Materials Today Physics 21 (2021) 100481

Contents lists available at ScienceDirect

Materials Today Physics

journal homepage: https://www.journals.elsevier.com/materials-today-physics

Low-pressure plasma-induced physical vapor deposition of advanced thermal barrier coatings: Microstructures, modelling and mechanisms

S.-H. Liu [a], J.P. Trelles [c], A.B. Murphy [d], W.-T. He [a], J. Shi [a], S. Li [a], C.-J. Li [b], C.-X. Li [b], H.-B. Guo [a, *]

[a] School of Materials Science and Engineering, Key Laboratory of Aerospace Materials and Performance (Ministry of Education), Beihang University, Beijing, 100191, China
[b] School of Materials Science and Engineering, State Key Laboratory for Mechanical Behavior of Materials, Xi'an Jiaotong University, Xi'an, Shaanxi, 710049, China
[c] Department of Mechanical Engineering, University of Massachusetts Lowell, Massachusetts, 01854, USA
[d] CSIRO Manufacturing, Lindfield, NSW, 2070, Australia

ARTICLE INFO

Article history:
Received 28 April 2021
Received in revised form
25 June 2021
Accepted 8 July 2021
Available online 21 July 2021

Keywords:
Thermal barrier coatings
Plasma spraying
Particles velocity
Vapor deposition
Numerical simulation

ABSTRACT

Thermal barrier coatings used to protect the blades of aircraft and gas turbine engines are primarily ceramic coatings with unique microstructures result of the deposition method used., for example, plasma spraying. Over the last decade, low-pressure (50–200 Pa) plasma spray - physical vapor deposition (PS - PVD) has been recognized as a promising method for obtaining advanced high-temperature performance thermal barrier coatings on gas turbines or aircraft engines. However, challenges still exist in experimental measurements and numerical modeling inside very large supersonic fluid fields (at the meter scale) with multiple phases (at micron- or nano-scale) at temperatures over 12000 K and velocities of over 6000 m/s. The plasma spray flow and heat and mass transfer in a closed chamber are not fully understood owing to the complicated interaction of the supersonic flow, swirling flow, phase transition and shock waves. This paper reviews the current state of technology in thermal barrier ceramic coatings obtained using PS-PVD. The multiphase flow characteristics during low-pressure plasma spraying using ceramic nano-agglomerated powders at different chamber pressures are studied via computational fluid dynamics modelling and experiment. The self-shadowing effect of impinging particles and the intensification of heat and mass transfer from the low-pressure plasma plume to the substrate are demonstrated. The flash vaporization and atomization of the ceramic droplets induced by the plasma jet shock waves are clarified. The formation, effects and control of quasi-columnar ceramic coatings in the additive manufacturing process of low-pressure plasma spraying are studied. Finally, this paper concludes with the future outlook and outstanding problems in this topic.

1. Introduction

1.1. Research status of the PS-PVD method

An important goal is the development of a coat-effective process to deposit an optimized columnar-like ceramic coating with low thermal conductivity and improved strain tolerance, allowing acceptable performance in high-thermal shock test [1–3]. Over the last decade, with the development of industrial requirements, the low-pressure plasma spray-physical vapor deposition (PS-PVD) method has been successfully used to obtain quasi-columnar ceramic coatings [5,10–12]. The PS-PVD method is a relatively new process that can deposit a coating of thickness between conventional PVD technologies (e.g., 1–20 μm) and conventional thermal spray processes [13–15]. The properties of quasi-columnar coatings are recognized as being superior to current thermal spray coatings, and they have a lower cost and higher deposition rate than EB-PVD coatings [5,10,15].

Typically, PS-PVD operates in a closed chamber at a low-pressure of 50–200 Pa through the use of a direct current non-transferred arc plasma torch to obtain a super-long plasma plume

* Corresponding author. School of Materials Science and Engineering, Beihang University, Key Laboratory of Aerospace Materials and Performance (Ministry of Education), Beihang University, No. 37 Xueyuan Road, Beijing, 100191, China.
E-mail address: guo.hongbo@buaa.edu.cn (H.-B. Guo).

https://doi.org/10.1016/j.mtphys.2021.100481
2542-5293/

Notation

C_D	drag coefficient
C_{ps}	specific heat of solid YSZ materials (J/kg K^{-1})
C_{pl}	specific heat of liquid YSZ materials (J/kg K^{-1})
D_p	particle diameter (μm)
$\boldsymbol{F_d}$	*drag force (N)*
$\boldsymbol{F_t}$	*thermophoretic forces (N)*
h	convective heat transfer coefficient (W m^{-2} K^{-1})
I	current (A)
σ_s	*Stefan Boltzmann constant* ($5.67 \times 10^{-8} W/m^2 K^{-4}$)
k_g	plasma gas thermal conductivity
L_m	melting latent heat of YSZ materials (J kg^{-1})
L_v	vaporization latent heat of YSZ materials (J kg^{-1})
P	pressure (Pa)
Q	*gas flow rate (kg/s)*
q_r	radiative heat loss from the particle surface
r_p	particle radius (μm)
Re_p	Reynolds number of particles
R_g	gas constant
T	*plasma gas temperature (K)*
T_m	particles melting temperature (K)
$\boldsymbol{V_p}$	*particle velocity (m/s)*
v_r	plasma velocity in the r direction
v_θ	plasma velocity in the θ direction
v_z	plasma velocity in the z direction
W	power (W)

Greek symbols

κ	thermal conductivity (W/m/K)
μ	dynamic viscosity (kg/m/s)
ρ	density (kg/m^3)

Subscript

b	boiling point
tr	crystallize transform
p	particle
m	melting point

Abbreviations

APS	Atmospheric Plasma Spraying
ALPS	Atmospheric Laminar Plasma Spray
BUAA	Beihang University
EBSD	Electron Back - Scattered Diffraction
GZO	gadolinium zirconate
IPF	Inverse Pole Figure
LCO	$La_2Ce_2O_7$
LTE	Local Thermodynamic Equilibrium
LZO	$La_2Zr_2O_7$
MHD	Magneto Hydrodynamic
OES	optical emission spectroscopy
Oh	Ohnesorge Number
PS - PVD	Plasma Spray - Physical Vapor Deposition
Pr	Prandtl Number
SD	Spraying Distance
Sh	Sherwood Number
SLPM	Standard Liter Per Minute
SPS	Suspension Plasma Spraying
Ta	Taylor Number
NCE	non-chemically equilibrium
NEC	Net Emission Coefficient
Nu	Nusselt Number
We	Weber Number
XJTU	Xi'an Jiaotong University
YSZ	yttria-stabilized zirconia

with a length of 1–2 m. The detailed operating parameters of current low-pressure plasma spray - physical vapor deposition technologies are listed in Table 1. The maximum length of the low-pressure plasma jet is approximately 2–2.2 m, as obtained by Refke [5] and Harder et al. [12]. Based on the low chamber pressure, the total gas flow rate of the plasma spray torch exceeded 60 SLPM when using argon, helium or hydrogen gases under a maximum input current of 2600 A, which is much larger than conventional plasma spray torches [23,35,59,73]. However, the powder feed rate is in the range of 0.5–20 g/min using nano-sized ceramic powders, which is significantly smaller than the conventional APS methods [24,25]. Since 2010, this method has been the subject of intensive research as the requirements for advanced ceramic coatings increase.

A key driver for expanding low-pressure plasma spray-physical vapor deposition technology is the desire to replace EB-PVD coatings at a low cost and high deposition rate [26–29]. Researchers have endeavored to develop a detailed understanding of this new method. However, many significant challenges and problems remain [30–34]. These include the mechanisms of heat and mass transfer between the supersonic plasma jet and nano-sized particles at temperatures above 10 000 K in less than a second when the powders are injected in the plasma torch; the formation mechanism and variation of the quasi-columnar ceramic coatings in the additive manufacturing of low-pressure plasma spray, and control of the vaporization phenomena of ceramic powders during the process. Further, the low-pressure plasma flow and associated heat and mass transfer in the closed chamber are not well understood because of the complicated interactions of the supersonic flow, swirling flow, phase transition and shock waves. Accordingly, the primary aims of this review are to understand the coating formation mechanism by presenting a broad range of research. This includes the plasma and in-flight particle diagnostics, fluid dynamic modeling taking into account multiple phases, and transient heat and mass transfer of phenomena during the entire coating process.

We present the unique microstructure variations in the coatings obtained using the low-pressure plasma spray physical vapor deposition method, together with their mechanical properties and high-temperature performance in Section 2. Besides, we compare these properties with those obtained using other plasma spray technologies. In Section 3, we focus on the time-dependent multiphase flows characteristics during the low-pressure plasma spraying of ceramic coatings at different chamber pressures. We use a numerical simulation in a large three-dimensional domain and compare the result with in-situ experimental measurements. In Section 4, the formation mechanism related to the self-shadowing effect of impinging particles, droplet breakup, and atomization during the sudden decrease in pressure from the plasma torch to the plasma jet are studied. In Section 5, the kinetics of surface diffusion and ceramic phase transformation on the substrate in this process are discussed. Finally, Section 6 and Section 7 present the future outlook and summary of this review on this topic, respectively.

1.2. Research background and thermal barrier coating manufacturing

Ceramic coatings are extensively used in different industrial

Table 1
Depositing parameters of low-pressure plasma spray - physical vapor deposited quasi-columnar coatings.

Institutes	Authors	Gas Flow Rates (SLPM)	Current (A)	Powder Feed Rate (g/min)	Operating Pressure	Spraying Distance (m)	Ref.
LERMPS, Université de Technologie de Belfort-Montbéliard (UTBM), France	Zahir. S, Christian. Coddet. et al.	Ar 40 SLPM +4 SLPM H_2	400/700 A	12–24 (Cu)	50–500 Pa	0.04–0.125	[4]
Sulzer Metco AG, Switzerland.	K. von Niessen, M. Gindrat, and A. Refke	200	2000–3000 A	2–10 (YSZ)	50–200 Pa	0.50–2	[5]
Department of Materials Engineering, The University of Tokyo ,Japan	Kazuyuki. Iizuka, M. Kambara, T. Yoshida et al.	Ar 52 SLPM +5 SLPM O_2 /Ar 170 SLPM +30 SLPM H_2	108 kW, RF Hybrid Plasma torch	0.36–0.05 (SnO_2) 0.8–3.2 (YSZ)	27 kPa	0.025–0.05	[6,7]
Dalian Maritime University, Center of Thermal Spray, Dalian, China	Yang Gao. D.M. Yang. et al.	Ar 30 SLPM +5 SLPM H_2	500/600 A	20 (YSZ)	50–100 Pa	0.4	[8,9]
Forschungszentrum Julich GmbH, Ju lich, Germany	G. Mauer, R. Vaßen. et al.	Ar 35 SLPM + He 60 SLPM	2600 A	1–20 (YSZ)	50–200 Pa	0.3–1.4	[10,30]
Sandia National Laboratories, USA	Mark F. Smith. et al.	–	2000 A 50 V	–	100 –500 Pa	–	[11]
NASA Glenn Research Center, Cleveland, USA	Bryan. J. Harder. et al.	80–120 SLPM Ar:He = 1:2	1700 A	2–11 (YSZ)	106.6 –150 Pa	1.7–2.2	[12]
Rzeszow University of Technology, Powstancow, Poland	Marek Goral. et al.	Ar 35 SLPM + He 60 SLPM	1600–2400 A	10–20 (YSZ)	140 –200 Pa	1.2	[13]
School of Material Science and Engineering, Beihang University, China	H. B. Guo. et al.	Ar 35 SLPM + He 60 SLPM	2000 A	5 (YSZ)	50–200 Pa	0.45–1.9	[14]
School of Material Science and Engineering, Xi'an Jiaotong University, China	C. J. Li. et al.	Ar 40 SLPM +8 SLPM H_2	620 A	0.5–2 (YSZ)	100 Pa	0.05–0.5	[15,16]
Guangzhou Research Institute of Non-ferrous Metals, China	K.S. Zhou, C. M. Deng, M Liu. et al.	Ar 35 SLPM + He 60 SLPM	2600 A	9–18 (YSZ)	150 Pa	0.95–2.2	[17,333],
Shanghai Institute of Ceramics, China	Fang. Shao, S. Y. Tao. et al.	Ar 35 SLPM + He 60 SLPM	2600 A	5 (YSZ)	150 Pa	0.5–1.0	[18,19]
Beijing General Research Institute of Mining and Metallurgy, China	D. M. Zhang, L.H.Gao. et al.	Ar 35 SLPM + He 60 SLPM	2000–2200 A	10–30 (YSZ)	100 –150 Pa	0.8–1.0	[20,21]
University of Toronto, Toronto, Canada	Pengyun. Xu, Javad. M. et al.	Ar 50 SLPM + H_2 10 SLPM	700 A	26–28 ($Yb(NO_3)_3$)	$1e^4$ ~ $3e^4$ Pa	0.08–0.1	[22]

fields. The stringent requirements of the aerospace industry are significant technology drivers for advanced ceramic coatings [35–37]. Thermal barrier coatings (TBCs) are critical components in modern gas turbines and aircraft engines as they can enable engines to operate stably with increasing gas temperature [38–40]. TBCs with multifunctional materials that protect the metal parts in the engine must have both very low thermal conductivities in the top ceramic coating and be able to withstand large thermal stress variations within the bonding coating under thermal shock (Fig. 1). The excellent thermal insulation and thermal cycling performances required of TBCs depend on the deposition method, particularly for the top ceramic layer when using 7–8 mol % yttria-stabilized zirconia (YSZ) [, # [41,42], gadolinium zirconate (GZO) [43–45], $La_2Ce_2O_7$ (LCO) or $La_2Zr_2O_7$ (LZO) [46–48].

Currently, the top ceramic coating is deposited using either electron-beam physical vapor deposition (EB-PVD) method or the plasma spraying methods (Fig. 2) [36,38,49,50]. In EB-PVD, a focused high-energy electron beam is used to melt the materials in a vacuum chamber [51,52]. The evaporating material condenses on the surface of the substrates or components [53]. While EB-PVD coatings with columnar-like microstructures have high thermal cycling lifetimes, they also have high thermal conductivities (typically 1.5–1.9 $Wm^{-1}K^{-1}$ by using YSZ) compared to those deposited by other methods [54–57]. Further, the process has high investment costs and a low deposition rate.

The atmospheric plasma spraying (APS) and atmospheric suspension plasma spraying (SPS) processes are operated under atmospheric conditions [58–60]. Typically, atmospheric plasma-sprayed YSZ coatings with lamellar structures, which have been used in thermal barrier systems for a long time, exhibit low adhesive strengths and low thermal conductivities (typically 0.8–1.8 W m^{-1} K^{-1}) [38,46,61]. The lamellar microstructure obtained from the stacking of successive splats is highly porous [62–64]. However, the coating is sensitive to thermal expansion mismatches and is not adaptable to the hot-section components of engines for high thermal cycling resistance.

Researchers have focused on developing a low-cost SPS method [65–68] that can deposit quasi-columnar ceramic coatings with lower thermal conductivity by using nano-sized feed powders that are dissolved in ethanol [60,77] or vertical segmentation coatings with very fine porosities and high densities of vertical segmentation cracks that exhibit high strain tolerance and low Young's modulus [69,70].

2. Unique microstructure evolution and properties of the coatings using the PS-PVD method

Since many conventional plasma spray methods deposited the ceramic coating of thermal barrier coatings with the lamellar structure and had a widely application on intricate components. The interconnection between lamellar structure and coating properties were understood. In the section, the unique microstructure of the PS-PVD coatings are discussed in detail and compared with conventional plasma spray methods. Process-structure-property relationships are discussed for the PS-PVD coatings. In addition, the influential factors for the formation of coating in the experiment are also discussed.

2.1. Microstructures of YSZ, GZO, LCO coatings using the PS-PVD method

TBCs are widely applied to protect the metal substrate of the hot section components of gas turbine. TBCs system is usually composed of a ceramic top coating as thermal insulation layer with low thermal conductivity and a metallic bond coating. Currently, yttria-stabilized zirconia (YSZ), gadolinium zirconia (GZO),

Fig. 1. Applications of thermal barrier coatings in (a), (b), (c), (d); the used plasma torch under the reduced pressure condition (e); the low-pressure plasma spray (LPPS) system at BUAA (f); the low-pressure plasma spray system in XJTU (g) (Copyright © Pixabay Licence).

$La_2Zr_2O_7$ (LZO) and $La_2Ce_2O_7$ (LCO) were used as ceramic material of ceramic top coating of TBCs [80–83], which exhibits low thermal conductivity and excellent mechanical properties by using conventional plasma spray methods or EB-PVD method [84,85]. And the coatings were shown different microstructures and consequently different properties by choosing different deposition methods and adjusting the deposition parameters.

Fig. 3 depicts the microstructures of coatings using PS-PVD method at a chamber pressure of 200 Pa and spraying distance of 1200 mm for yttria-stabilized zirconia (YSZ) and gadolinium zirconia (GZO) and 1000 mm for $La_2Ce_2O_7$ (LCO), using 30 SLPM argon, 60 SLPM helium, and plasma spray torch current of 2000 A. Fig. 3-d, 3-h and 3-l show the cross-section of the nano-agglomerated 7–8 mol % YSZ (d_{50} = 10 μm, Metco 6700, Oerlikon Metco, Westbury, USA) [86], GZO (d_{50} = 27 μm, Gd: Zr in a 1:1 M ratio) [88] and LCO (d_{50} = 20 μm, La and Ce in a 1.25 atomic ratio) powders [89], respectively.

Quasi-columnar microstructures are observed on the fracture surfaces in Fig. 3, which correspond multi-island protrusions with intervening spaces on the top surface. At higher magnification, the elements of the columnar-like structures on the top surface of the coatings are observed to be nanoclusters (Fig. 3-c, 3-g and 3-k).

2.2. Microstructural evolution of ceramic coatings with different spraying parameters

Fig. 4 shows the microstructural evolution of YSZ coatings under different spraying conditions. The dense lamellar structures, similar to those obtained with APS shows in Fig. 4-a and 4-b, closely packed columnar structure in Fig. 4-c, quasi-columnar structures in Fig. 4-d, and EB-PVD-like columnar structures in Fig. 4-e and 4-f were obtained as the spraying distances increased from 400 mm to 1900 mm. Moreover, the inter-space between the quasi-columnar structures at the top surface of the coating increased as the carrier gas flow rates increased using the same powders from Fig. 4- g to 4- L.

A conventional atmospheric plasma sprayed ceramic coating frequently exhibits a lamellar structure with a certain number of pores, including globular pores, inter-lamellar unbonded interfaces, and vertical cracks in individual splats [90–92]. The existence of

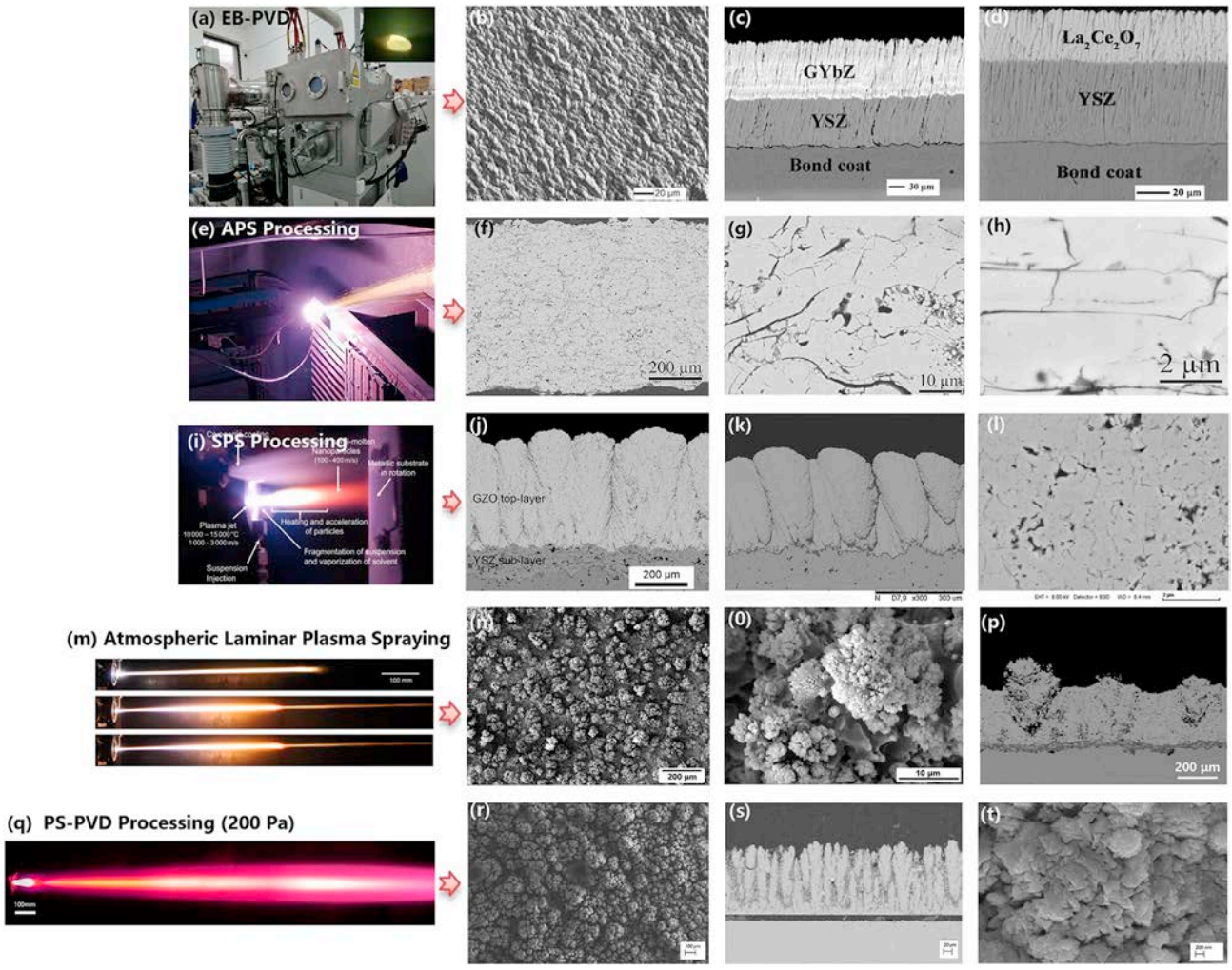

Fig. 2. Current deposition methods and columnar or quasi-columnar microstructures for thermal barrier coatings: EB-PVD system (a) and microstructures of ceramic coatings [71,72] (b), (c), (d); conventional atmospheric plasma spray method (e) and typical microstructures of coatings (f), (g), (h) [73,74]; atmospheric suspension plasma spray process (SPS) [75] (i) and typical microstructures of coatings (j), (k), (l) [76,77]; (c) atmospheric laminar plasma spray process (ALPS) in (m) and typical microstructures of YSZ coatings (n), (o), (p) [78,79]; low-pressure plasma spray-physical vapor deposition (PS-PVD) process (q), and typical microstructures of coatings (r), (s) and (t) (Reproduced with permission © Springer Nature, IOP Publishing Ltd., & Elsevier B.V.).

limited lamellar interface bonding as inter-lamellar pore in the ceramic coating was revealed in literature [[73,90]]. Intra-splat cracks are also usually observed within individual ceramic splats [93], which are generated by the intrinsic quenching stress. The pores in the form of unbonded inter-splat interfaces and intra-splat cracks are usually interconnected through the whole coating. A limited lamellar interface bonding sets up a low ceiling for properties [94], this coating is also very sensitive to a thermal expansion mismatch between the ceramic and metallic part of the TBCs, leading to a relatively low lifetime on the high pressure components of the turbine engine [95], although it is shown a low thermal conductivity that is expected for thermal barrier coating [90].

Generally, coatings with dense microstructures exhibit good performance for material protection against corrosion and wear [91,92]; coatings with full vertical cracks and microporous microstructures have a low thermal conductivity owing to enhanced phonon scattering and reduction in the phonon mean free path [38,42,111]. Moreover, coatings with columnar-like microstructures can offer high thermal compliance and thermal stress accommodation in thermal cycling tests [96–98]. Thus, the PS-PVD process allows a wide range of options for depositing coatings with different microstructures. The coating quality, i.e., density, hardness, elastic modulus, fracture toughness, and thermal conductivity is controlled by the spraying parameters.

2.3. Mechanical properties and high-temperature performances of coatings using PS-PVD

We investigated the corresponding elastic modulus (Fig. 5-a), cross-section hardness (Fig. 5-b), cross-section porosity (Fig. 5-c), thermal diffusivity at 1273 K (Fig. 5-d), thermal conductivity (Fig. 5-e) and thermal cycling lifetime (Fig. 5- f) of the YSZ, GZO, and LCO coatings deposited using the PS-PVD method as part of this work, and compared them with the results of the APS, SPS, and EB-PVD methods and a novel atmospheric long laminar plasma spray method (ALPS). The depositing parameters are shown in Table 2.

The elastic modulus of thermal spray coatings usually differ from the corresponding bulk material. Indentation tests have been used widely for thermal spray coatings to quantitatively measure their resistance to deformation under an applied load. The coating elastic modulus can be viewed as an indication of internal cohesion, porosity or the void and crack network, chemical phases and their

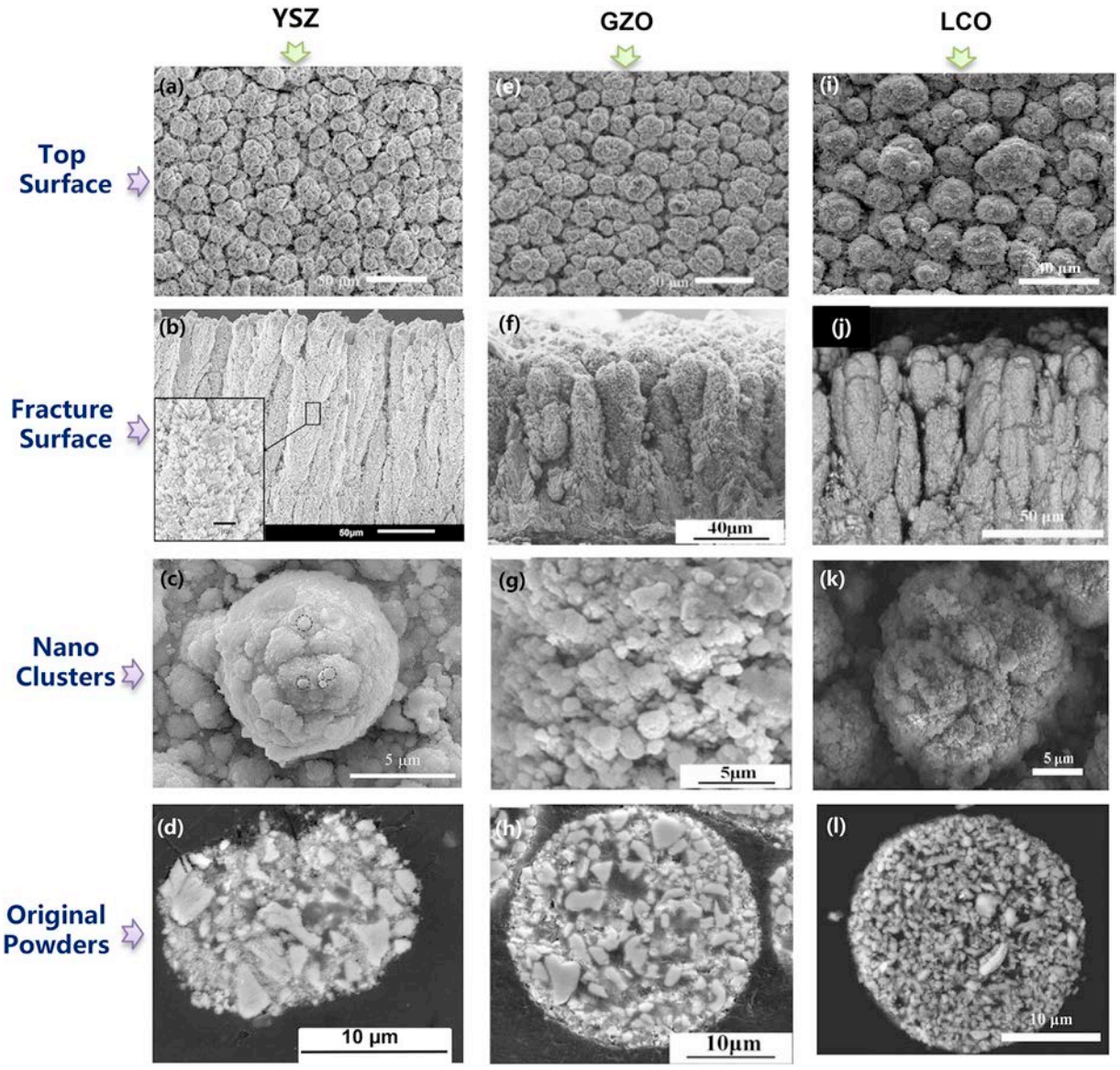

Fig. 3. Microstructures of low-pressure PS-PVD ceramics coatings: YSZ coatings at the top surface (a), fracture surface (b), nanoclusters on the top surface (c), original powder (d) [86,87]; GZO coatings at the top surface (e), fracture surface (f), nanocluster on the top surface (g), original powder (h) [88]; LCO coatings at the top surface (i), fracture surface (j), nanoclusters on the top surface (k), original powder (l) [89] (Reproduced with permission © Elsevier B.V.).

proportions within a coating, and the residual stress state [112]. Fig. 5-a shows the maximum elastic modulus of the EB-PVD GZO coating is 265 ± 11 GPa [71]. It is obviously affected by the columnar structure of EB-PVD coatings with strong anisotropic properties.

The elastic modulus of the coatings in this study were in the range of 70–125 GPa, including YSZ, GZO, and LCO coatings [89,99,109,110], which were used for nano-indentation tests on the polished cross-section of the coating. The maximum elastic modulus of the PS-PVD YSZ coatings from the studies of Deng. et al., Shan. et al., and Li et al. were approximately 167 GPa, 130 GPa, and 189 GPa [101,104,105], respectively. The elastic energy of the coating is determined by the thermal expansion mismatch between substrate and topcoat, the temperature difference, the elastic modulus of the coating, and the thickness [113]. This can be explained by the existence of the pores and defects in PS-PVD coatings and usually the elastic modulus decreases significantly with an increase in porosity, which has been widely reported in the literature [114,115].

APS ceramic coatings present a low elastic modulus in Fig. 5-a. The elastic modulus of an anisotropic, non-homogeneous, porous material is highly affected by microstructural features. Anisotropic pores and splat boundaries in thermal sprayed coatings can reduce the elastic modulus of coatings, and introduce anisotropy in the modulus relative to the spray direction [116].

Vickers indentations were used to measure the hardness on the cross-sections of the coating, which is widely used for thermal spray coatings to quantitatively measure their resistance to deformation under an applied load. The cross-section hardness of the GZO coating is higher than that of the YSZ and LCO coatings deposited using the PS-PVD method (Fig. 5-b), as well as the hardness of GZO bulk materials is higher than the YSZ and LCO [117]. Deng et al. reported a maximum hardness of 11.7 GPa for a YSZ coating by PS-PVD [102]. The hardness of LCO and LZO coatings deposited through the APS method is in the range of 2.9–3.5 GPa [109,110], and that of the EB-PVD manufactured GZO coating is 8.8 ± 0.4 GPa [71]. The maximum hardness of the atmospheric

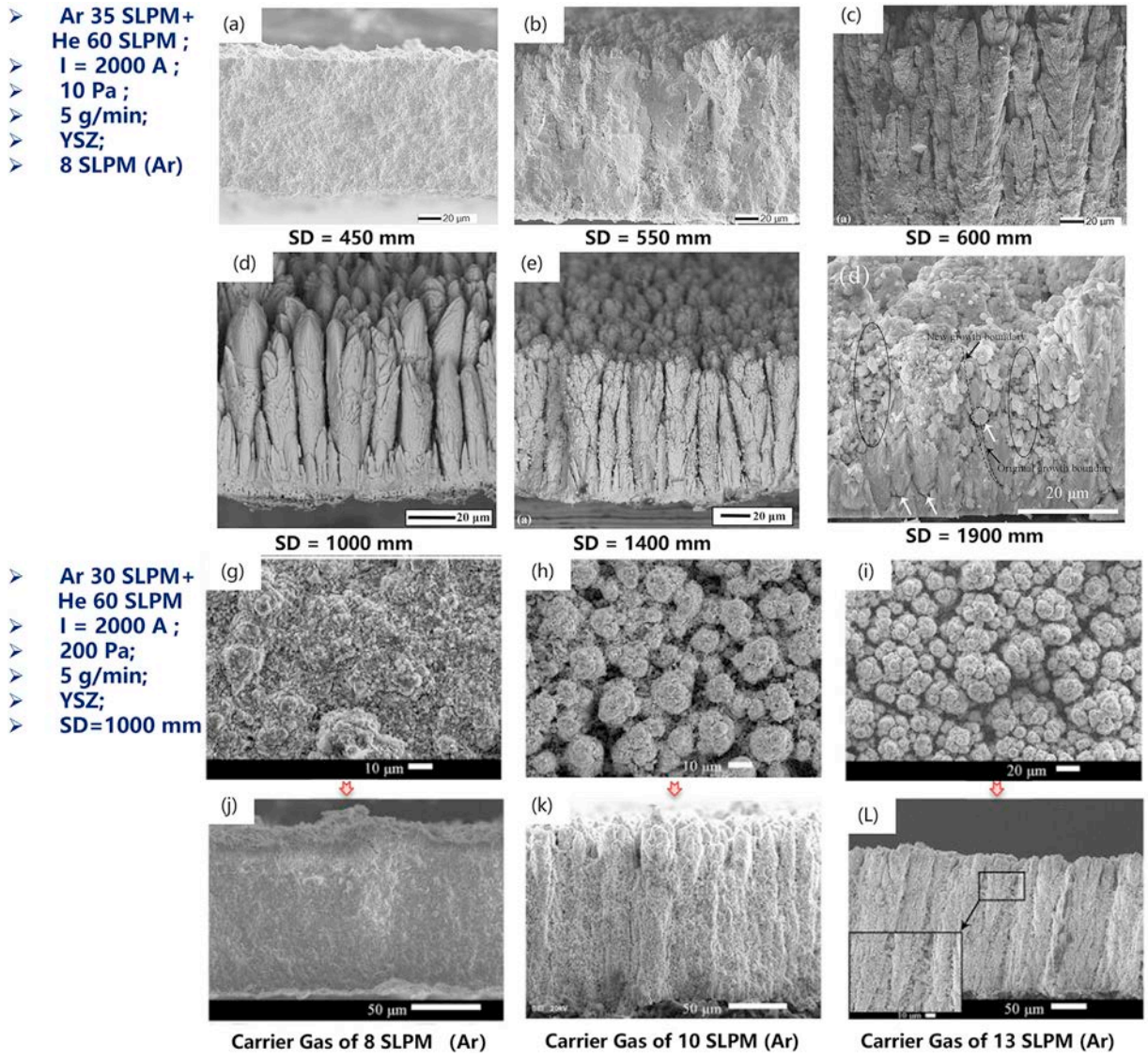

Fig. 4. Microstructures of PS-PVD manufactured YSZ coatings at different spraying distances in (a), (b), (c), (d), (e), (f) [14] and at different carry gas flow rates in (g), (h), (i), (j), (k), (l) [86] (Reproduced with permission © Elsevier B.V & Springer Nature).

laminar plasma sprayed YSZ coating is 8.9 GPa [111]. The average hardness of the YSZ coating prepared using the SPS method by Jordan et al. is 5.15 ± 1.1 GPa [118].

The porosity values at the cross-section of the coatings are shown in Fig. 5-c. The atmospheric suspension plasma-sprayed YSZ coating exhibited a maximum porosity of 37 ± 2 % with the use of very fine YSZ powders (d_{50} = 85 nm) that were dissolved in ethanol [119]. The cross-sectional porosity of the quasi-columnar coatings using PS-PVD in this study was in the range of 12–18 %, which is similar to the results obtained by other authors using the PS-PVD method. However, the atmospheric plasma-sprayed LZO, LCO, and YSZ coatings had a wide range of the porosities under different deposition conditions, which depended on specific requirements.

The results of thermal diffusivity of the ceramic coatings shown in Fig. 5-d was measured using a laser-flash apparatus (i.e., Netzsch. Inc., LFA-427, Germany). The thermal diffusivity of the YSZ coating at 1273 K deposited using the SPS method was approximately 0.7 mm^2/s, which was higher than other results. In this study, the PS-PVD manufactured GZO and YSZ coatings had thermal diffusivities of 0.3 mm^2/s and 0.5 mm^2/s at 1273 K, respectively. Gao et al. reported a thermal diffusivity of 0.39 mm^2/s for a PS-PVD manufactured YSZ coating [21]. The thermal diffusivity of a GZO coating using the EB-PVD method was 0.24 ± 0.02 mm^2/s.

The thermal conductivities of the coatings in Fig. 5-e were calculated by multiplying the thermal diffusivity, specific hear capacity, and density. Thermal conductivity is a critical criterion for evaluating the thermal insulation of the TBCs. Currently, SPS manufactured YSZ coatings offer the lowest thermal conductivities (Fig. 5-e). In PS-PVD coatings, the thermal conductivity of the GZO coating produced by PS-PVD method was lower than that of the YSZ coating. The YSZ porous columnar structures led to a significant decrease in thermal conductivity in the range of 0.5–1 W $m^{-1}K^{-1}$ compared to values of YSZ EB-PVD coatings (1.3–1.5 W $m^{-1}K^{-1}$) [120].

The LCO and LZO coatings using the APS method have thermal conductivities at 1273 K of 0.59 and 0.74 W m^{-1} K^{-1} at 1273 K, respectively [109,110], which are lower than those of YSZ coatings deposited using the APS or ALPS methods. The thermal conductivity of YSZ coating using SPS method are found to be lower than 1 W $m^{-1}K^{-1}$ from room temperature up to 1100 °C [108], while the

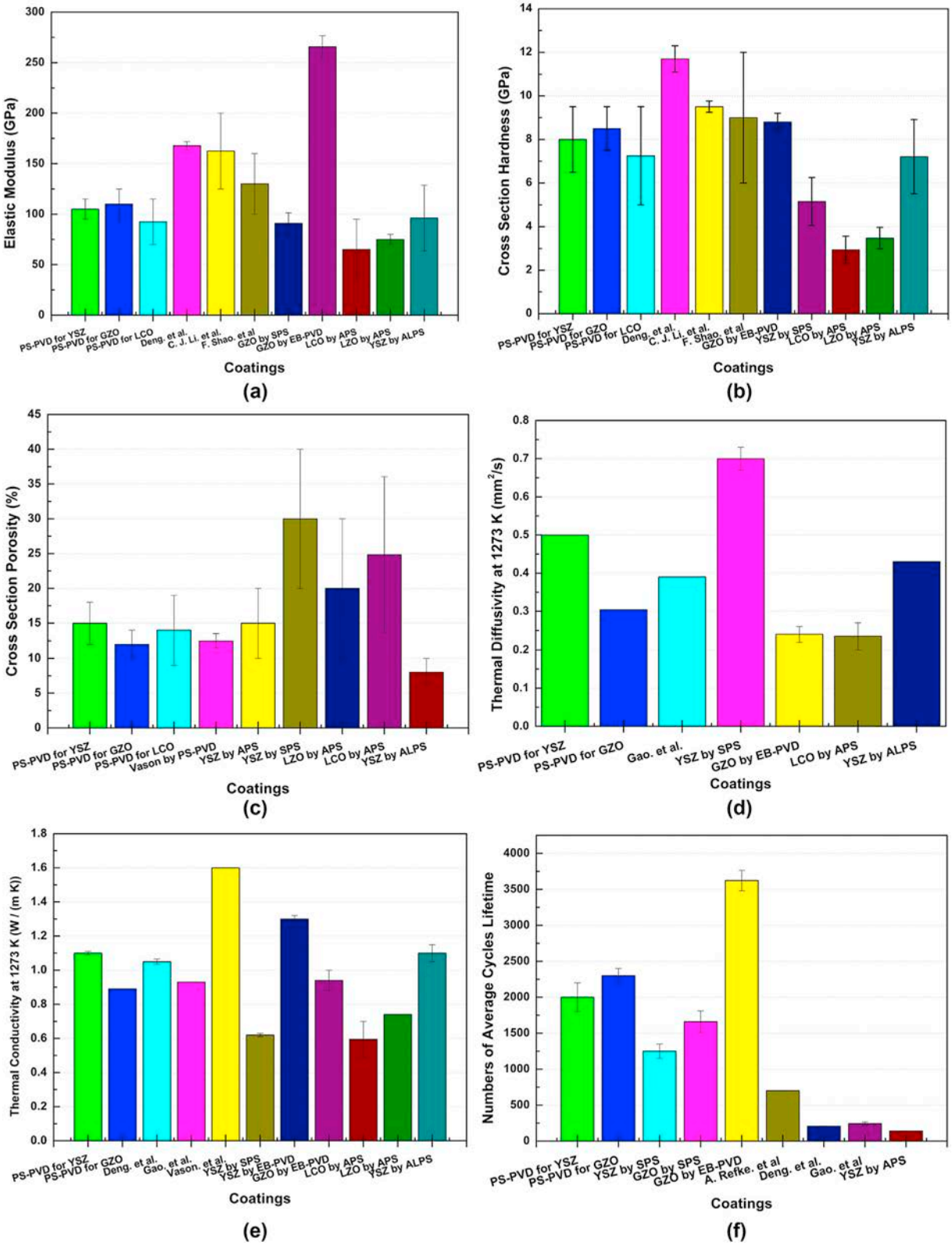

Fig. 5. Mechanical properties and high-temperature performances of PS-PVD ceramic coatings in this study and compared with those of coatings deposited using APS, ALPS, SPS and EB-PVD methods that were listed in Table 2.

EB-PVD coating is recorded at 1.2–1.3 W $m^{-1}K^{-1}$ at 1100 °C [107].

TBCs were used to reduce the surface temperature of hot components or to permit higher gas inlet temperatures and improve the service lifetime of the engines and the overall efficiency. Higher thermal insulation and longer cyclic lifetime are the crucial requirements of advanced TBCs for gas turbines. The thickening of thermal growth oxide (TGO) in the TBCs results in a large growth of strain and stress, which is one of the most important failure mechanisms of TBCs. Typically, with increase of the cycling time of APS coatings, the TGO layer grows thicker and reduces the local thermal contraction of the bond coating. Cracks are able to continuously propagate at valley areas of the interface, and there will converge with adjacent cracks and lead to a final failure of TBCs. The thermal cycling lifetimes of GZO and YSZ coatings produced using the SPS method were all higher than those of coatings produced using the APS method (Fig. 5-f). Furthermore, EB-PVD manufactured GZO coatings can offer up to 3700 cycles when the coating is heated at 1050 °C for 5 min and then air cooling for 40 s [71].

The quasi-columnar structure led to a redistribution of the radial thermal stresses at the vicinity of top coating and bonding coating interface [121]. The cracks are able to extend at the inter-space of columns, further connect with adjacent cracks to release residual stress after thermal shocks. Fig. 5-f shows the average thermal cycling lifetimes of the YSZ and GZO coatings by PS-PVD were all greater than 2000 cycles when the coatings were heated at 1100 °C for 5 min and then air-cooled for 5 min. The coatings present a good sintering resistance after thermal cycling, the column structure retains their original appearance and column interspace are still exist. Deng et al. and Gao et al. used the water-cooling method after heating the PS-PVD coatings in a thermal cycling test; thermal cycling lifetime was in the range of 203–267 cycles (1100 °C for 5 min and then water cooling). Vaßen et al. reported the PS-PVD YSZ coating after 5000 thermal cycles by using a burner rig facility (natural gas/oxygen heating for 5 min and then air cooling for 2 min) [32]. A. Refke et al. present the PS-PVD columnar structure YSZ coating showed superior results with more than 700 cycles achieved without any failure of the coating (1135 °C for 50 min and then air cooling in 4 min) [5].

3. Multiphase flow characteristics in the PS-PVD processing

The multiphase flow characteristics during the low-pressure plasma spraying were significantly affect the coating formation. The heat and mass transfer processing associate with the supersonic flow, swirling flow and shock waves from the narrow region inside the plasma torch to the low pressure chamber, where the original powders will rapidly transfer from solid to liquid or vapor phase within 2 s. In this section, this complicate processing inside the closed chamber were reviewed according to experiment and numerical investigations, as well as the particle heating and motion were simulated in a three-dimensional domain. Furthermore, the evolution of particle phase transformation in various conditions was briefly described.

3.1. Experimental investigations during the PS-PVD processing

The particle diameter, velocity, and flow rate of the powder injection, and the flow velocity and temperature of the plasma gas at the torch nozzle all affected the coating quality. The strong interaction between the flow field characteristics and the particle flow parameters complicates the particle behavior during spraying. Plasma diagnostics have become a broad field of research, encompassing measurements of plasma gas characteristics [122–124], plasma gas heat transfer [125–127], magnetohydrodynamic instabilities [23,128–131], in-flight behavior of individual particles [132–136,158], and interactions of the particles and plasma with the substrate [137–139]. Together, the measurements can provide a visualization of interactions between particles and plasma gas.

Spectroscopic and optical methods (e.g., Oseir Ltd., Spray Watch camera, Finland; Technar Ltd., DVP-2000, Canada; laser Doppler anemometry), and probe methods (e.g., Pitot tubes and electric, enthalpy, and thermal probes) are widely used in in-situ measurements of thermal spraying [140–142], particularly for the plasma jet area after particle injection in the experiment [143,144]. Spectroscopic diagnostics methods are based on measuring the intensity of spectral lines of emission and absorption, or the half-widths and shifts of spectral lines (e.g., emission coefficient, the radiation intensity, the absorption coefficient, and transmittance coefficient) [145]. The optical actinometry method is based on the determination of the intensities of the emission lines by comparison with a known spectrum, excitation, and deactivation of an emitting gas [146]. Probe methods provide local values of the plasma characteristics through the use of different probe devices (see Table 3).

Measurements inside the arc plasma spray torch present significant challenges, partly because of the very small area (at the centimeter scale) and extreme conditions (velocity > 1000 m/s and temperature >10000 K) and partly because of the lack of access, particularly for the PS-PVD process that operates in a closed chamber. Nevertheless, a wide range of devices inside and outside the operation chamber can be used to understand the low-pressure plasma spray process (Fig. 6-a).

Generally, the fluctuation characteristics in the jet flow near the torch exit are generally similar to that of an arc voltage [152,153,171]. The fluctuation of the arc voltage induces the variations of input energy to plasma generation. It causes different heating effects in plasma spraying and brings the fluctuation of the parameters in the jet flow [23,186]. Therefore, the fluctuation behavior of the plasma jet and the internal arc instabilities significantly affect both torch performance and coating quality [154,155]. An oscilloscope is commonly used to detect the time-resolved arc voltage fluctuation on microsecond or millisecond time scales. Typical results are shown in Fig. 6-b. The arc voltage fluctuation of a conventional atmospheric plasma spray torch (i.e., Sulzer F4 Torch) is frequently ± 20 V to ± 50 V when using 30 SLPM argon and 12 SLPM hydrogen at a current of 600 A [156]. A triplex plasma spray torch has a low amplitude of arc voltage fluctuation ($\Delta U = 7–8$ V) when it operates at an average arc voltage of 94.47 V. Moreover, the atmospheric laminar plasma spray torch is frequently operated at an average arc voltage of 167 V with an amplitude of ±0.5 V to ±2 V [157]. Finally, although the input current of the PS-PVD torch was 2000 A in this study, the average arc voltage was only 32 ± 2 V in the experiment using 30 SLPM argon and 60 SLPM helium at a chamber pressure of 200 Pa. It is predicted that the drag force of the flow inside the torch is too weak for driving the arc root movement intensively at reduced pressure. The higher gas flow rates lead to more arc column constriction and the arc column in the anode become constricted at higher pressure region.

Fig. 6-c shows the in-flight particle velocity distributions in cross-sections perpendicular to the spraying direction measured using a commercial particle diagnostic system (Technar Ltd., DVP-2000, Canada). The YSZ particle velocity in the low-pressure plasma spray process (100 mbar, I = 2600 A, 50 SLPM argon + 110 SLPM helium) at the spray distance ranging from 200 mm to 550 mm [158] was higher than those of other APS methods, including ALPS method (9.8 SLPM nitrogen and 4.2 SLPM argon, output power of 25.4 kW) [78], an atmospheric Praxair SG-100 Gun spray system (48 SLPM argon and 12 SLPM helium, output

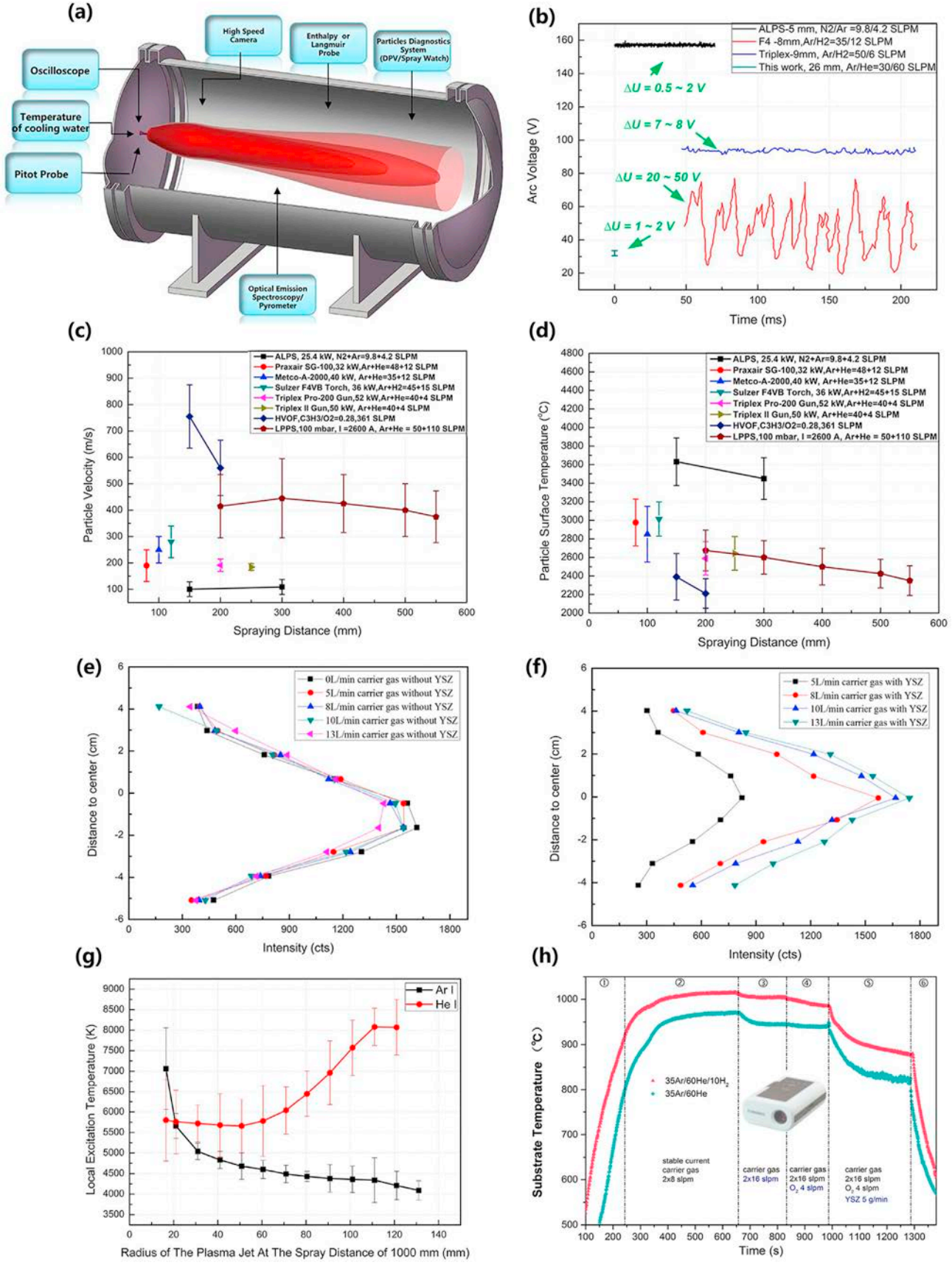

Fig. 6. Diagnostics in and around the low-pressure chamber (a); time-resolved arc voltage vibration in three atmospheric plasma spray torches and PS-PVD torch used in this work (b); YSZ particle velocity (c) and surface temperature (d) at different spraying distances; optical emission spectra intensity with different carrier gas flow without YSZ injection in (e) and with YSZ injection in (f) [86]; local excitation temperature along the radial direction of the plasma jet at the spraying distance of 1000 mm (Ar 35 SLPM + He 60 SLPM, I = 2750 A, 100 Pa) in (g) [170] and measured substrate temperature when the plasma jet impinges from 100 s to 1300 s at the same operating conditions [170] (Reproduced with permission © Springer Nature & Elsevier B.V).

Table 2
Depositing parameters of the coatings in Fig. 5

Coatings	Power/Feed rate	Materials	Thermal Cycling Test	References
PS-PVD for YSZ	1850 A; 100 Pa; 5 g/min; SD = 1000 mm	NiCoCrAlY bond coating. With pre-oxidation α-alumina (0.4 μm)	1200 ± 30 °C for 5 min and then cooled by compressed air for 90 s	[99,100]
PS-PVD for GZO	2000 A; 200 Pa; 5 g/min SD = 1000 mm	Gd_2O_3 +ZrO_2, Gd:Zr = 1:1 in molar ratio; NiCoCrAlY bond layer by multi arc ion plating	1100 °C for 5 min and then air cooling 5min	[88]
PS-PVD for LCO	2000 A; 100 Pa; 6 g/min SD = 1000 mm	La_2O_3, CeO_2; La/Ce = 1.25 in atomic ratio	/	[89]
C. M. Deng.& M. Liu. et al. by PS-PVD	128 kW; 150 Pa; 18 g/min; SD = 950 mm	100 μm NiCoCrAlY bond coating; 120 μm Metco 6700. 7–8 wt.% YSZ	1050 °C for 5 min and then water cooling	[17,101,102]
L. H. Gao & D.M. Zhang. et al. by PS-PVD	2200 A; 150 Pa; 10 g/min SD = 1000 mm	Metco 6700. 7–8 wt.% YSZ	1100 °C for 5 min and then water cooling	[20,21]
A. Refke. et al. by PS-PVD	50–200 Pa;	Metco 6700. 7–8 wt.% YSZ; PtAl bond coating	1135 °C for 50 min and then air cooling for 4min	[5,103]
Vaßen.et al. by PS-PVD	2200 A; 100 Pa; 10 g/min SD = 1000 mm;	Metco 6700. 7–8 wt.% YSZ	5 min heating by natural gas/oxygen; 2 min air cooling	[31]
F.Shao & S.Y. Tao. et al. by PS-PVD	2600 A; 150 Pa; 5 g/min SD = 1000 mm	Metco 6700. 7–8 wt.% YSZ	/	[104]
C.J. Li. et al. by PS-PVD	600 A; 100 Pa; 0.5 g/min SD = 350 mm	100 μm NiCoCrAlY bond coating; 120 μm Metco 6700. 7–8 wt.% YSZ	/	[15,105]
GZO by EB-PVD	1×10^{-3} Pa	$(Gd_{1-x}Yb_x)_2Zr_2O_7$; (x = 0,0.1,0.3,0.5,0.7)	1050 °C for 5 min and then air cooling 40 s.	[117]
YSZ by EB-PVD	1×10^{-3} Pa	a NiCoCrAlY bond coat and a YSZ topcoat	/	[106,107]
YSZ by APS	630 A; 42 kW; 3 g/min; SD = 110 mm	NiCoCrAlYTa bonding layer; 7 YSZ	1050 °C for 5 min and then water cooling	[102]
YSZ by SPS	32.2 kW; 25 g/min; SD = 50 mm	7 wt% YSZ; aluminized NiAl bond coat	1100 °C for 15 min and then air cooling 15 min	[108]
GZO by SPS	750 A; 105.5 kW; 30 g/min; SD = 100 mm	$Gd_2Zr_2O_7$; CoNiCrAlY bond coating	1050 °C for 5 min and then air cooling 2 min	[76,77]
LCO by APS	42 kW; 20 g/min; SD = 100 mm	0–60 mol% YSZ doped La_2O_3/CeO_2; NiCrAlY bonding layer	1000 °C for 55 min and then air cooling 5min	[109]
LZO by APS	650 A; 39 kW; 25 g/min; SD = 80 mm	$La_2Zr_2O_7$	/	[110]
YSZ by ALPS	160 A; 26 kW; 8 g/min	NiCoCrAlY bond coating; Metco 204NB 7–8 wt.% YSZ	/	[111]

Table 3
Experimental parameters of plasma spray systems in Fig. 6-c and 6-d.

Business Name	Output Power (kW)	Gas Flow Rate (SLPM)	Spraying Distance (mm)	Powders	Ref.
ALPS Torch	26	N_2 (9.8 SLPM) + Ar (4.2 SLPM)	150/300	YSZ	[78]
Praxair SG-100 Torch	32	Ar (48 SLPM) + He (12 SLPM)	80	YSZ	[147]
Metco-A-200	40	Ar (35 SLPM) + He (12 SLPM)	100	YSZ	[148]
Sulzer F4VB Torch	36	Ar (45 SLPM) + H_2 (15 SLPM)	120	YSZ	[149]
Triples Pro-200 Torch	52	Ar (40 SLPM) + He (4 SLPM)	200	YSZ	[150]
Triples II Torch	50	Ar (40 SLPM) + He (4 SLPM)	250	YSZ	[151]
HVOF Torch	/	361 SLPM C_3H_3/O_2 = 0.28	150/200	Alumina	[164]
LPPS Torch	125	Ar (50 SLPM) + He (110 SLPM)	300	YSZ	[158]

power of 32 kW) [159], an atmospheric Metco- A-200 system (30 SLPM argon and 12 SLPM helium, output power of 40 kW) [160], an atmospheric Sulzer F4VB Torch spray system(45 SLPM argon and 15 SLPM hydrogen, output power of 36 kW) [161], atmospheric Triplex Pro-200 Torch spray system(40 SLPM argon and 4 SLPM helium, output power of 52 kW) [162] and atmospheric Triplex II Gun spray

system (40 SLPM argon and 4 SLPM helium, output power of 50 kW) [163]. However, the particle velocity for the high-velocity oxygen fuel (HVOF) method in an atmospheric environment using a total gas flow rate of 361 SLPM was higher than that of LPPS at spray distances of 150 and 200 mm [164].

The distributions of the in-flight particle surface temperature are shown in Fig. 6- d. The average surface temperature of YSZ particles in the LPPS method remains above 2200 °C at a spraying distance of 550 mm, which means that the powders flight through a very long distance after they are injected into the low-pressure plasma jet and a mass of droplets of YSZ materials exist at a spraying distance of 550 mm. The particle surface temperatures obtained using the Triplex Pro-200 Gun and Triplex II Gun spray systems are similar to those obtained using the LPPS method at spraying distances of 200 mm and 250 mm. The surface temperature of YSZ particles with other APS methods is approximately

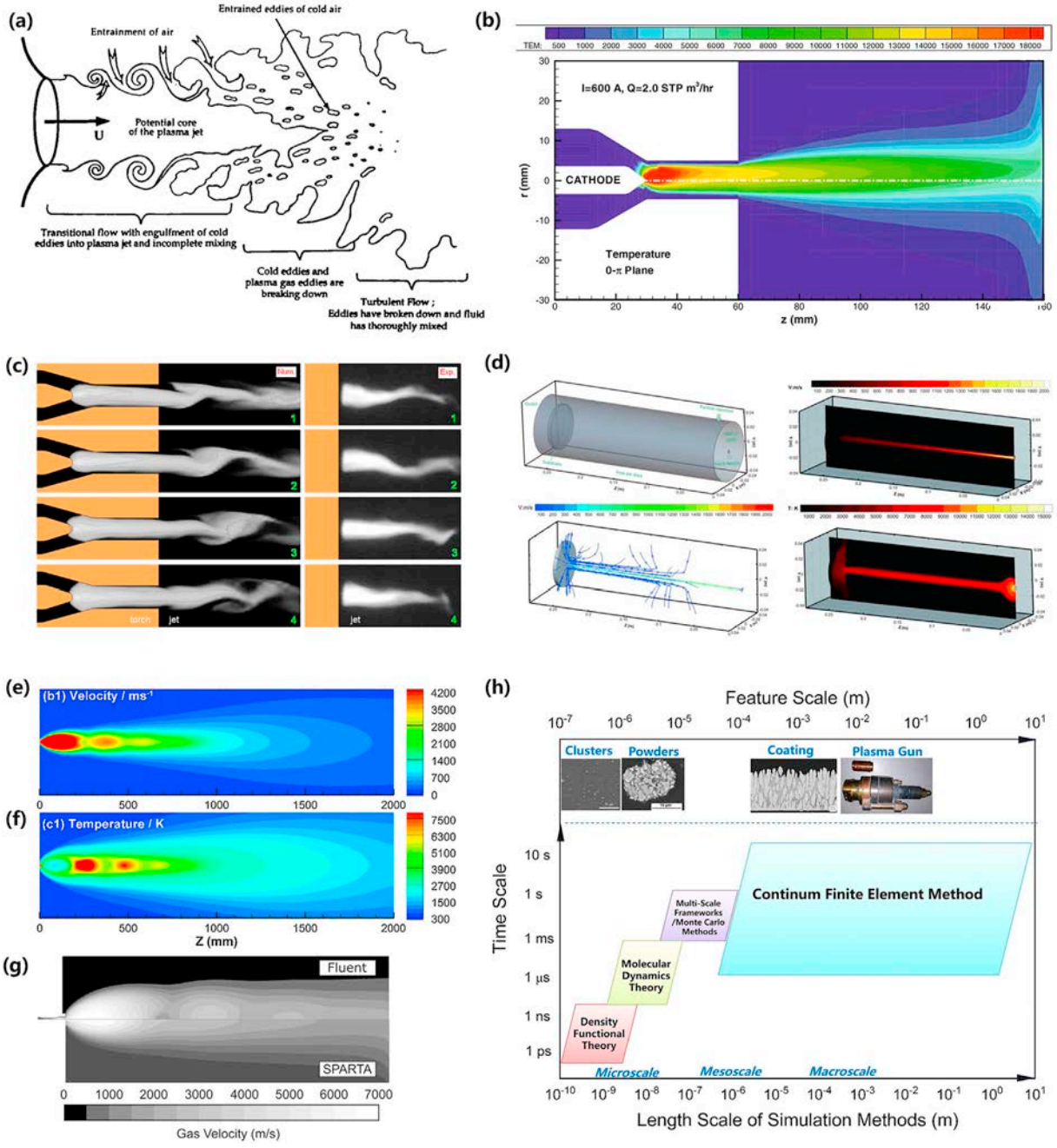

Fig. 7. (a) Regions of entrainment of cold gas into an atmospheric thermal plasma jet by E. Pfender et al. (1991) [174,175]; (b) temperature distributions in a plasma torch and plasma jet area under pure argon of 2.0 STP m^3/h and current of 600 A conditions from H. P. Li et al. (2007) [176]; (c) distributions of instantaneous heavy-particle temperature distribution obtained from the numerical simulation and experimental observations by J. P. Trelles (2008) [177]; (d) three-dimensional simulation of the atmospheric laminar plasma spray process by S. H. Liu et al. (2020) [79]; velocity (e) and temperature (f) distributions of low-pressure plasma jet at a chamber pressure of 100 Pa by using 100 SLPM argon and 10 SLPM hydrogen in a two-dimensional axisymmetric domain by M. J. Liu (2019) [254]; (g) Dmitrii Ivchenko et al. (2018) predicted contours of velocity magnitude using Ansys Fluent and SPARTA [252]; (h) length and temporal scales in simulations of the low-pressure plasma spray process.

2600–3200 °C at a spraying distance of 80–120 mm. As Fig. 6-d shows, the YSZ surface temperature with the ALPS method is clearly higher than other results; this is because of the very low particle velocity.

The intensities of the optical emission spectra of the low-pressure plasma jet for various carrier gas flow rates at a spraying distance of 600 mm (P = 200 Pa, 30 SLPM Ar + 60 SLPM He, I = 2000 A) with and without YSZ particles are shown in Fig. 6-e and 6-f [86], respectively. The optical emission spectrometer (OES) was operated at a wavelength of 402.62 nm to record Ar II and a wavelength of 378.05 nm to record neutral zirconium (Zr I). The intensity of the Ar II emission spectrum in the low-pressure plasma plume decreased slightly as the carrier gas flow rate increased from 0 SLPM to 13 SLPM at a spraying distance of 600 mm because the density of the cold argon carrier gas is larger than the thermal plasma gases inside the plasma torch [165,166]. The increase in the cold carrier gas flow rate can affect the fluid characteristic of the low-pressure plasma jet and result in an asymmetric distribution of the Ar spectrum intensity (Fig. 6-e). Moreover, under the same conditions, the intensity of the neutral zirconium emission intensifies after the YSZ particle injection (Fig. 6-f), although it decreases when using a 5 SLPM carrier gas with YSZ powders since the heating histories of in-flight particles were short. This means that the flow rate of the carrier gas in the PS-PVD process significantly affects the heating and motion of YSZ powders inside the plasma torch in the experiment due to the huge differences between cold gas density and plasma gas density [167,168]. Basically, the laterally injection of carrier gases caused appreciable three-dimensional flowing in the plasma spraying and the jet will be deviated from its original geometrical axis, leading to non-axisymmetry distributions of temperature, mass fraction and velocity [169]. Therefore, an appropriate carrier gas flow rate will help the particles penetrate further to the plasma plume at the beginning and finally benefit to obtain a long heating history. It usually shows a high emission intensity at a given spraying distance as the similar results by Liu. et al. [255] and He et al. [170].

An abel inversion was used to calculate the excitation temperatures of Ar I and He I at a spraying distance of 1000 mm of the low-pressure plasma jet (P = 200 Pa, 35SLPM Ar + 60 SLPM He, I = 2750 A) (Fig. 6-g) [170]. The maximum excitation temperature of Ar I was approximately 7000 K, and the temperature decreased from the center to the periphery of the plasma jet. The maximum excitation temperature of He I in Fig. 6-g was approximately 8000 K at the periphery of the plasma jet. A strong deviation from the local thermal equilibrium was exhibited at the periphery of the low-pressure plasma plume.

Under the same conditions, the substrate temperature variation was recorded using a pyrometer at a wavelength of 1.6 μm as the low-pressure plasma jet impinged on a planar substrate (Inconel 718 alloys) [170]. The substrate surface temperature rapidly increase to a maximum value of 1000 °C, when the low-pressure plasma jet impinged on the substrate at a speed of 1000 m/s, and the temperature is slightly decreased as the carrier gas flow rate increased. Furthermore, when using the mixture gases of argon (35 SLPM), helium (60 SLPM), and hydrogen (10 SLPM), the substrate temperature was higher than the result obtained using the mixture gases of argon (35 SLPM) and helium (60 SLPM) owing to the increased thermal conductivity due to the presence of hydrogen.

The dynamic arc attachment inside the PS-PVD torch, the fluid characteristics of the low-pressure plasma jet, the carrier gas flow rates, and powder feed rates, and the substrate temperature are all likely to affect the formation of ceramic coatings. However, the chamber pressure, plasma plume flow streamlines, powder heating history, and particle flight trajectory are still unknown. The distribution of vapor concentration of ceramic materials is not able to be detected using spectral or probe methods. We expected that the turbulent flow is a crucial factor limiting the controllability of the plasma spray [171–173]. A three-dimensional numerical simulation of the low-pressure plasma spray process was employed to comprehensively aid in understanding the multiphase flows inside a low-pressure chamber. This is described in the following.

3.2. Modeling of arc plasma spraying

In the plasma spray torch, an electric arc is formed between the cathode and the anode [178]. The input gases abruptly expand owing to the rapid heating of the arc to very high temperatures (from 15 000 to 25 000 K) [179,180], dissociating and ionizing the gas [181,182]. The plasma is initiated by a high-voltage pulse that causes localized ionization and a conductive path for an electric arc to form between the cathode and anode [183,184]. The thermal plasma formed in the torch has a high energy density (10^6–10^7 J/m^3), high heat flux density (10^7–10^9 W/m^2), high quenching rate (10^6–10^8 K/s), and high processing rates [185].

Plasma jet instabilities are primarily caused by the large density and velocity gradients at the interface between the jet and the surrounding gas, and by the pulsating force due to the movement of the arc inside the torch [186,187]. These instabilities cause eddy roll-ups at the interface between the plasma and the surrounding gas and finally result in large-scale turbulence [24,188]. Because of the strong radiation from the arc and its confinement inside the torch, the direct observation of the dynamics of the arc inside the torch is extremely difficult.

Currently, computational fluid dynamic modeling of thermal plasma aided by the rapidly increasing computational. It bases on the coupled magneto-hydrodymanics (MHD) model equations have been widely used in the numerical simulation of atmospheric plasma spray processes and provide agreement with the experimental results [23,157,176,177,185,204] and has expanded over the last three decades from two-dimensional to three-dimensional models of steady or transient processes [185,189,190,210]. E. Pfender et al. (1991) showed that a rapid decrease in the axial jet velocity of the atmospheric plasma jet is caused by the entrainment of the cold gas surrounding the plasma jet, which is more of an engulfment type process than simple diffusion (Fig. 7-a) [174]. Li et al. (2007) modeled the three-dimensional temperature and flow fields inside and outside a direct current arc plasma spray torch. The results indicated that the anode arc root inside the torch moved downstream as the gas flow rate increased at a constant input current (Fig. 7-b) [176]. Trelles et al. (2008) simulated the instantaneous heavy-particle temperature distributions and compared them with the high-speed images from an experiment at intervals of 100 μs (Fig. 7-c) [177]. These results revealed the role of thermal non-equilibrium and entrainment at the interface between the plasma jet and the surrounding gas. Liu et al. (2020) modeled the atmospheric long laminar plasma spray process with consideration of the substrate (Fig. 7-d) [79]. The results showed an expansion area near the nozzle exit of the plasma torch, followed by the formation of a uniform jet as observed in experiments. Intensive entrainment of the surrounding gases occurred in the downstream area, particularly when the laminar plasma jet impinged on the surface of the substrate.

- Thermal Plasma Flows

However, few researchers focused on the modelling of low-pressure PS-PVD process. Vautherin and Bolot et al. (2014) calculated a low-pressure plasma spray system at a chamber pressure of 150 Pa, presenting an expansion area at the torch nozzle and a typical supersonic flow [249]. Yan and Liu et al. (2015) modeled a

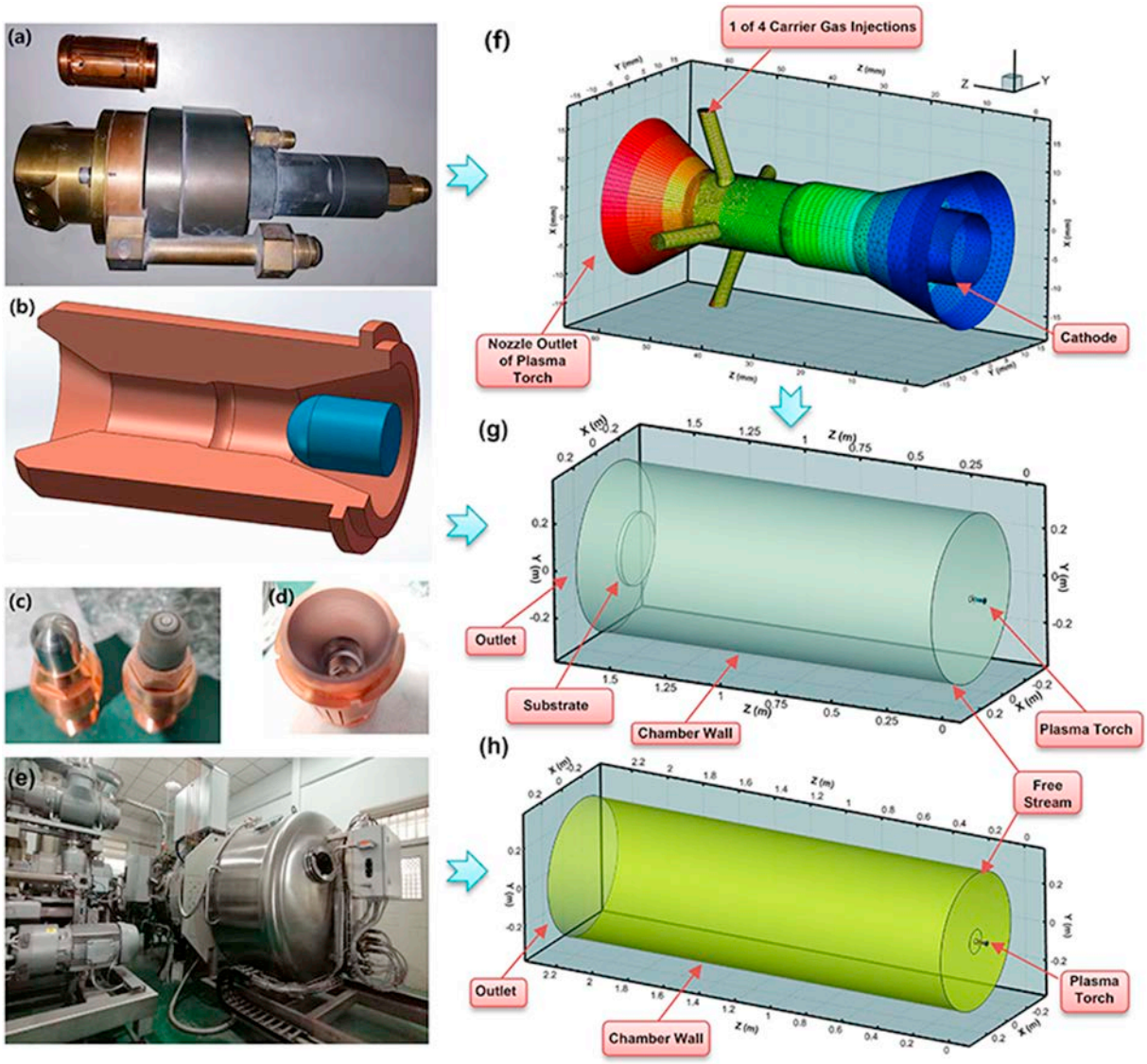

Fig. 8. (a) internal channel structure of the plasma torch (b); the new and eroded cathode bar (c) and anode (d) in the experiment; overview of the PS-PVD system in this work (e); calculation domain of the PS-PVD torch with four carrier gas injection locations (f); computational domain of the PS-PVD plasma torch with the plasma jet (g), and of the torch with a free plasma jet (h).

low-pressure plasma spray process at a chamber pressure of 10 kPa and obtained a maximum plasma velocity of 6100 m/s using 65 SLPM argon at an input power of 39 kW [250]. Ivchenko and Vardelle et al. (2018) used FLUENT and SPARTA software to study the fluid characteristics in the PS-PVD method using 40 SLPM argon and 8 SLPM hydrogen at a chamber pressure of 100 Pa (Fig. 7-g) [251]. Liu et al. (2019) calculated the velocity and temperature distributions of a low-pressure plasma jet by using 100 SLPM argon and 10 SLPM hydrogen at a chamber pressure of 100 Pa [255]. The maximum velocity and temperature at the torch nozzle are exceeded 4200 m/s and 7500 K (Fig. 7-e and 7-f, respectively). Despite the merits of attained results, all these models run relied on two-dimensional axisymmetric domains and therefore are not suitable to properly investigate particle heating and motion in realistic three-dimensional configures, such as closed spraying chambers.

In this work, the following assumptions are adopted, in accordance with our previous studies [157]: 1) the plasma jet is considered to be a fluid with corresponding thermodynamic, and the transport properties are functions of temperature and the conservation equations assume the fluid to be a continuum medium; 2) the working gas at the gas inlet is injected in the axial direction without any swirling velocity component at the initial.

Although many non-LCE and non-LTE models have been developed for argon plasma [191–196], the plasma flow is assumed to be in a local thermodynamic equilibrium (LTE) state in this approach, because of the lack sufficient data for the electrons and heavy particles of argon and helium mixture plasma gases. The equilibrium compositions of argon and helium systems including Ar, Ar^{+}, Ar^{2+}, Ar^{3+}, He, He^{+}, and electrons at different pressures were computed by minimizing the Gibbs free energy of the system using the computed compositions [197,198], the thermodynamics properties such as mass density (ρ), specific enthalpy (h), and specific heat (C_P) were calculated. The transport properties such as electrical conductivity (σ), thermal conductivity (κ), and viscosity (η) were obtained using the third-order approximation of the

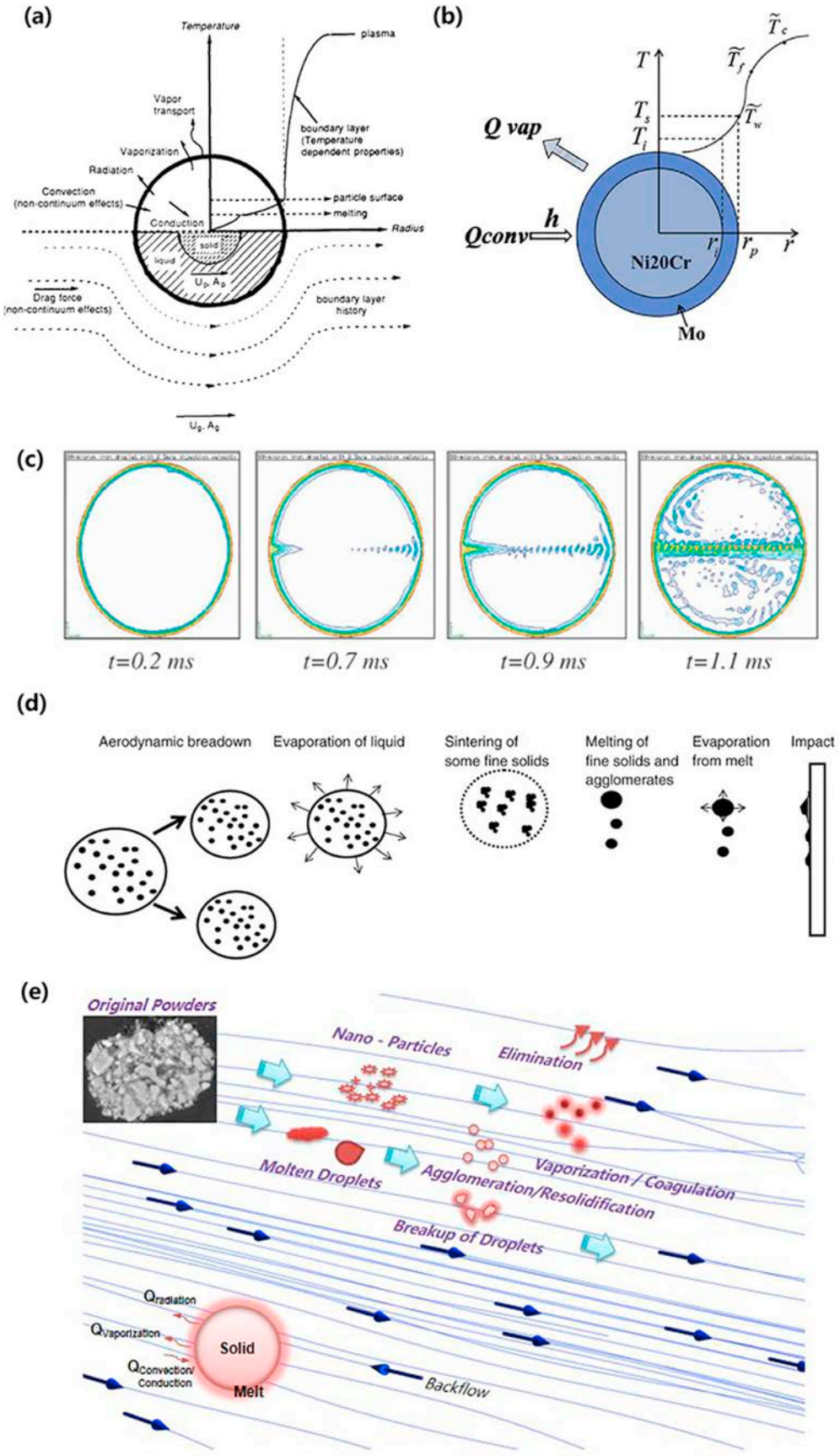

Fig. 9. Numerical analysis of powder heating and motion in the plasma spray: (a) Szekely et al. (1992) illustrated the particle heat, mass, and momentum transfer phenomena [217]; (b) Li et al. (2018) simulated the heating of core-shell structure powders [218]; (c) Vardelle et al. (2001) modeled the convective motion of a Hill vortex within an iron particle 60 μm in diameter in the core of an Ar–H_2 plasma jet [219,220]; (d) Pawlowski (2009) investigated the phenomena affecting in-flight suspension droplets in the high-temperature plasma [221]; (e) we predicted the heating and motion histories of the original nano-agglomerated YSZ powders in the low-pressure plasma jet in this work.

Chapman–Enskog method using the collision integrals between the plasma species [199–202].

- Turbulence model transport equations

In Reynolds-averaging approaches (e.g., the Spalart-Allmaras model, the K - ε models, and the K - ω models), the solution variables in the instantaneous Navier-Stokes equations are decomposed into the mean (ensemble-averaged or time-averaged) and fluctuating components [203,205,325]. The advantage of these approaches, such as the renormalization group or realizable K - ε turbulent model, is a relatively low computational cost associated with the computation of the turbulent viscosity (μ_t) and thermal conductivity (k_t). In many cases [23,157,185,204], these methods have been successfully used to model the turbulent transport inside or outside the plasma spray torch. They generally require two other equations that are coupled with the above Magneto-Hydrodymanics Model equations. The turbulent fluctuations are characterized by the local turbulence energy K and dissipation rate ε [205]. The particle trajectories are computed by tracking them as they interact with a sequence of turbulent eddies [325].

An alternative approach to RANS is the Reynolds Stress Method (RSM), which includes five additional equations describing the evolution of the terms in the Reynolds stress tensor [206,207]. Although the RSM model requires significantly more additional memory and calculation time than the K- ε or the K - ω two-equation models, it has been reported to be suitable for the description of highly swirling flows [208,209,250]. Therefore, we used both Realizable and RSM turbulence transport models that coupled with the above MHD model to investigate the low-pressure plasma jet at chamber pressures of 50 Pa, 100 Pa, 200 Pa, and 1000 Pa, and compared the predictions with experiment results.

Fig. 8 shows the computational domains, chosen to represent the experiments. The boundaries comprise the surfaces of the torch nozzle exit, wall of the torch, free jet area, chamber wall, substrate, and outlet. The PS-PVD torch (Fig. 8-a and 8-b) contains four particle injection paths with the carrier gas in the radial direction of the torch channel (Fig. 8-f). The size of the cathode and anode were all according to the experiment (Fig. 8-c and 8-d). We modeled the coupled regions of the plasma torch, plasma jet, and substrate (Inconel 718 alloys, d = 300 mm, δ = 5 mm) as operated in the experiment. The diameter of the low-pressure plasma jet domain was 700 mm (Fig. 8-g and 8-h). The maximum length of the PS-PVD domain with substrate shown in Fig. 8- g was 1700 mm, and the substrate was at a spraying distance of 1500 mm from the torch nozzle. The maximum length of the PS-PVD domain of the plasma torch and plasma free jet was 2200 mm (Fig. 8-h). The number of nodes in the computational mesh of Fig. 8-f, 8-g and 8-h were approximately 493456, 6484791, and 6843500, respectively.

- Boundary conditions of the low-pressure plasma torch and jet domains

The external torch wall and the chamber wall were cooled using water. The third boundary condition of heat transfer is shown in Eq. (11). The heat transfer coefficient was 1.0×10^5 W/m^2/K, and T_w is the reference cooling water temperature of 500 K [157,204].

$$-k\left(\frac{\partial T}{\partial r}\right)_w = h_w(T_W - T_\infty) \tag{11}$$

The boundary conditions on the cathode surface were the current density and temperature distribution [157,185,210], which can be defined over the cathode rod tip by using the following equations:

$$j(r) = J_{\max}\exp\left(-(r/R_c)^{n_c}\right) \tag{12}$$

$$T(r) = T_w + T_c\exp\left(-\left(\frac{r}{2R_c}\right)^{n_c}\right) \tag{13}$$

where r is the radius of the hottest region of the cathode tip, and n_c specifies the shape of the current density profile, which is set to 4 in this work [157,204]. Typically, the maximum value of the current density J_{max} is set to 2.5×10^8 A/m^2 for an input current of 600 A for a commercial plasma spray torch [204]. Hence, J_{max} is set to 8.4×10^8 A/m^2 for an input current of 2000 A. The value of $j(r)$ has been reported to have no significant effect on the temperature and velocity distributions at the nozzle exit. The long process of heat and momentum transfer from the upstream to the downstream of the plasma torch channel eliminates any influence [211,212].

- Particle heating and motion

Modelling of the heating and motion of particles during plasma spraying is now widely used. Westhoff and J. Szekely et al. (1992) first proposed a single particle model for the calculation of particle velocity, trajectories, and heating histories based on the consideration of non-continuum effects, particle vaporization and the temperature gradient within the particles (Fig. 9-a). The results indicated that the radial component of the plasma gas velocity is important in determining the trajectory of small particles [217]. Then, Li et al. used the same model to study the particles with Mo shell and Ni20Cr core in atmospheric plasma spray (Fig. 9-b) [218]. They clarified the effect of the particle temperature gradient on a novel shell-core structured powders, and the formation of a dense NiCrMo coating. Zhang and Vardelle et al. investigated the convective motion of a Hill vortex within an in-flight particle in an Ar–H_2 plasma jet (Fig. 9-c), which was caused by the high ratio of the kinematic viscosities between the plasma gas and the particle [219]. Pawlowski described the evolution of a suspension droplet in a high-temperature plasma plume (Fig. 9-d) [221], which included aerodynamics breakup, vaporization of the liquid, sintering of fine solids, and impact with the substrate.

Therefore, as Fig. 9-e shows, we consider that the original nano-agglomerated powders initially penetrate the plasma plume and then separate into nano-particles. Nanoparticles are heated to molten droplets or continuously vaporize on the surface, causing a decrease in particle size. As the surface temperature approaches the boiling point of zirconia, the vaporization of the particles becomes increasingly rapid. The in-flight particles may suffer melting, break up, agglomeration, re-solidification (self-cooling), vaporization, coagulation, and elimination. The particles may impact the substrate under any condition depending on the local plasma gas conditions, which have a significant effect on the coating quality.

The governing equations for the particle heating and motion are based on as following,

$$m_p\frac{d\overrightarrow{V_p}}{dt} = \overrightarrow{F_d} + \overrightarrow{\mathrm{F_p}} + \overrightarrow{\mathrm{F_t}} + \overrightarrow{\mathrm{F_b}} \tag{14}$$

$\overrightarrow{V_p}$, $\overrightarrow{F_d}$, $\overrightarrow{\mathrm{F_p}}$, $\overrightarrow{\mathrm{F_t}}$, and $\overrightarrow{\mathrm{F_b}}$ are the particle velocity (m/s), drag force (N), pressure gradient force (N), thermophoretic force (N), and body force (N), respectively; $\overrightarrow{\mathrm{F_p}}$ is the force on the particle caused by the pressure gradient; $\overrightarrow{\mathrm{F_b}}$ is the gravitational force that caused by the gravitational force. In atmospheric plasma spraying, the forces due to gravity and pressure gradients are usually very small [213,214]. However, the pressure gradient force of in-flight particles in the PS-

PVD process must be considered when the particles flow from a high-pressure region of the plasma torch (10^3–10^4 Pa) to a low-pressure region of the chamber (50–200 Pa). The thermophoretic force expression was obtained from the studies of Pfender and Chen et al. [215,216].

A representation of the particle size distribution (i.e. Metco 6700, YSZ, d = 1–30 μm, d_{50} = 1–10 μm, Oerlikon Metco. Inc, Westbury, USA) was calculated using as the Rosin-Rammler equation, which is an exponential relationship between the diameter and the mass fraction of particles that is based on the natural logarithm of the particle diameter [205].

- Drag coefficient for non-continuum effects of the in-flight particles

Eq. (15) is a widely-used equation in the simulation of particle motion in an atmospheric plasma jet from Refs. [222,233].

$$C_d = \begin{cases} \frac{24}{Re_p} & Re_p < 0.2 \\ \frac{24}{Re_p}\left(1+\frac{3}{16}Re_p\right) & 0.2 \le Re_p < 2 \\ \frac{24}{Re_p}\left(1+0.11Re_p^{0.81}\right) & 2 \le Re_p < 21 \\ \frac{24}{Re_p}\left(1+0.11Re_p^{0.632}\right) & 21 \le Re_p < 500 \\ \frac{10.56}{Re_p} & Re_p > 500 \end{cases} \quad (15)$$

where Re_p is the particle Reynolds number, which is calculated using:

$$Re_p = \rho_g |U - Up|\ d_p/\mu_g \quad (16)$$

where U_p is the relative velocity between the plasma gas and particle.

However, we adopted and equation used by Wan et al. (1999) to correct for non-continuum effects in plasma spray (Eq. (17)) [223], which tend to reduce the drag coefficient owing to velocity slip on the surface of particles [241]:

$$C_d = \left(\frac{24}{Re_p} + \frac{6}{1+Re_p} + 0.4\right) f_{prop}^{-0.45} f_{Kn}^{0.45} \quad (17)$$

$$f_{prop} = \frac{\rho_p \mu_p}{\rho_g \mu_g} \quad (18)$$

$$f_{Kn} = \left[1 + \left(\frac{2-a}{a}\right)\left(\frac{\gamma_g}{1+\gamma_g}\right)\frac{4}{Pr_g}Kn\right]^{-1} \quad (19)$$

f_{prop} represents the effects of the variable plasma properties; f_{Kn} is used to describe non-continuum effects in the thermal plasma flows for Knudsen numbers in the range of $10^{-2} < Kn < 1$, which was proposed by Chen and Pfender (1983) [224]; Kn is the Knudsen number; a is the thermal accommodation coefficient; γ_g is the specific heat ratio, and Pr_g is the Prandtl number of the plasma gas [225].

We also considered the effect of deviations from a spherical shape of the in-flight particles caused by phase changes and deformations in the liquid phase by using a dynamic drag force C_{dd} in Eq. (20),

$$C_{dd} = C_d(1 + 2.632y) \quad (20)$$

which represent the effects of droplet distortion in a high swirling flow of a large Weber number [226]; y ranges from 0 for a spherical droplet to 1 for a disk-shaped droplet. Obviously, the drag coefficient of a disk droplet is higher than that of a sphere droplet.

To accurately model droplet breakup while flowing in a high-speed plasma plume, the wave model is used, allowing prediction of the size distributions during the deposition. The wave model considers the breakup of the droplets to be induced by the velocity gradient between the plasma gas and the in-flight particles. It is reported to be suitable for application in a high-speed swirling flow by considering the Kelvin-Helmholtz instability that is induced by the plasma jet under low-pressure conditions [227]. In this model, the change in the droplet radius is calculated using the following equations [227]:

$$r = B_o \Lambda \quad (21)$$

$$\frac{\Lambda}{a} = 9.02\frac{\left(1+0.45Oh^{0.5}\right)(1+0.4Ta^{0.7})}{\left(1+0.87We_g^{1.67}\right)^{0.6}} \quad (22)$$

$$\frac{da}{dt} = -\frac{(a-r)}{\tau},\ r \le a \quad (23)$$

This model is based on the relationship between the parent and the parcel in the droplet breakup. The breakup of droplet parcels is calculated by assuming that the radius of the newly formed droplets is proportional to the wavelength of the fastest-growing unstable surface wave on the parent droplet [227]. B_0 is a model constant, and τ is the breakup time. The relationships between the Ohnesorge number, Taylor number, and Weber numbers are expressed as [228–230],

$$Oh = \sqrt{We_l}\Big/Re_p \quad (24)$$

$$Ta = Oh\sqrt{We_g} \quad (25)$$

where the We_l and We_g are the liquid and gas Weber numbers, respectively.

- Particle heat transfer

The heat transfer from the plasma gas to the particles is estimated according to the following equation [222]:

$$m_p\frac{d(C_{ps}T_p)}{d_t} = -A_p\lambda_p(T_p - T_g) + H_f\frac{dm_p}{dt} \quad (26)$$

where m_p is the mass, C_{ps} is the specific heat of the particle, H_f is the latent heat of phase change, T_p is the temperature of the particle, and λ_p is the heat transfer coefficient obtained using:

$$\lambda_p = \frac{k_g Nu}{d_p} \quad (27)$$

where k_g is the thermal conductivity of the plasma gas, and Pr is the Prandtl number from Eq. (28):

$$Pr = C_{pg}\mu_g\Big/k_g \quad (28)$$

The empirical Nusselt number of the particles is usually

calculated based on the Reynolds and Prandtl numbers of the particles. However, researchers have used different expressions to calculate the Nusselt number, listed in the following equations [231–233]:

$$\mathrm{Nu} = 2.0 + 0.515\mathrm{Re}_p^{0.5} \tag{29}$$

$$\mathrm{Nu} = 2.0 + 0.6\mathrm{Re}_p^{0.5}\,\mathrm{Pr}_p^{0.33}\ ,\ (0 \le \mathrm{Re}_p \le 776.06,\ 0 \le \mathrm{Pr}_p \le 250) \tag{30}$$

$$\mathrm{Nu} = 2.0 + 0.27\mathrm{Re}_p^{0.62}\,\mathrm{Pr}_p^{0.33}\ ,\ (776.06 \le \mathrm{Re}_p,\ 0 \le \mathrm{Pr}_p \le 250) \tag{31}$$

$$\mathrm{Nu} = \left(2.0 + 0.27\mathrm{Re}_p^{0.5}\,\mathrm{Pr}_p^{0.33}\right)\left(\mathrm{f}_{\mathrm{prop}}\right)^{0.6} f_{kn} f_v \tag{32}$$

Xiong and S. Sampath used Eq. (32) to obtain the Nusselt number. This model predicts strong vaporization of the zirconia at high temperatures, in agreement with the experimental results [234].

In Eq. (32), f_v is used to account for the effect of mass transfer owing to vaporization, using an expression proposed by Faeth (1983) [235]:

$$f_v = \frac{m_v C_p \big/ 2\pi r_p k_f}{\exp\left[m_v C_p \big/ 2\pi r_p k_f\right] - 1} \tag{33}$$

The boundary layer at the particle surface is determined as follows:

$$\left.\frac{\partial T_p}{\partial r}\right|_{r=0} = 0 \tag{34}$$

$$4\pi r_p^2 \left(k_p \frac{\partial T_p}{\partial r}\right)\Big|_{r=r_p} = \mathrm{Q}_{\mathrm{conv}} - \mathrm{Q}_{\mathrm{vap}} - \mathrm{Q}_{\mathrm{rad}} \tag{35}$$

The convection ($\mathrm{Q}_{\mathrm{conv}}$), radiation ($\mathrm{Q}_{\mathrm{rad}}$), and vaporization ($\mathrm{Q}_{\mathrm{vap}}$) latent heat fluxes on the surface of the particle are determined as follows:

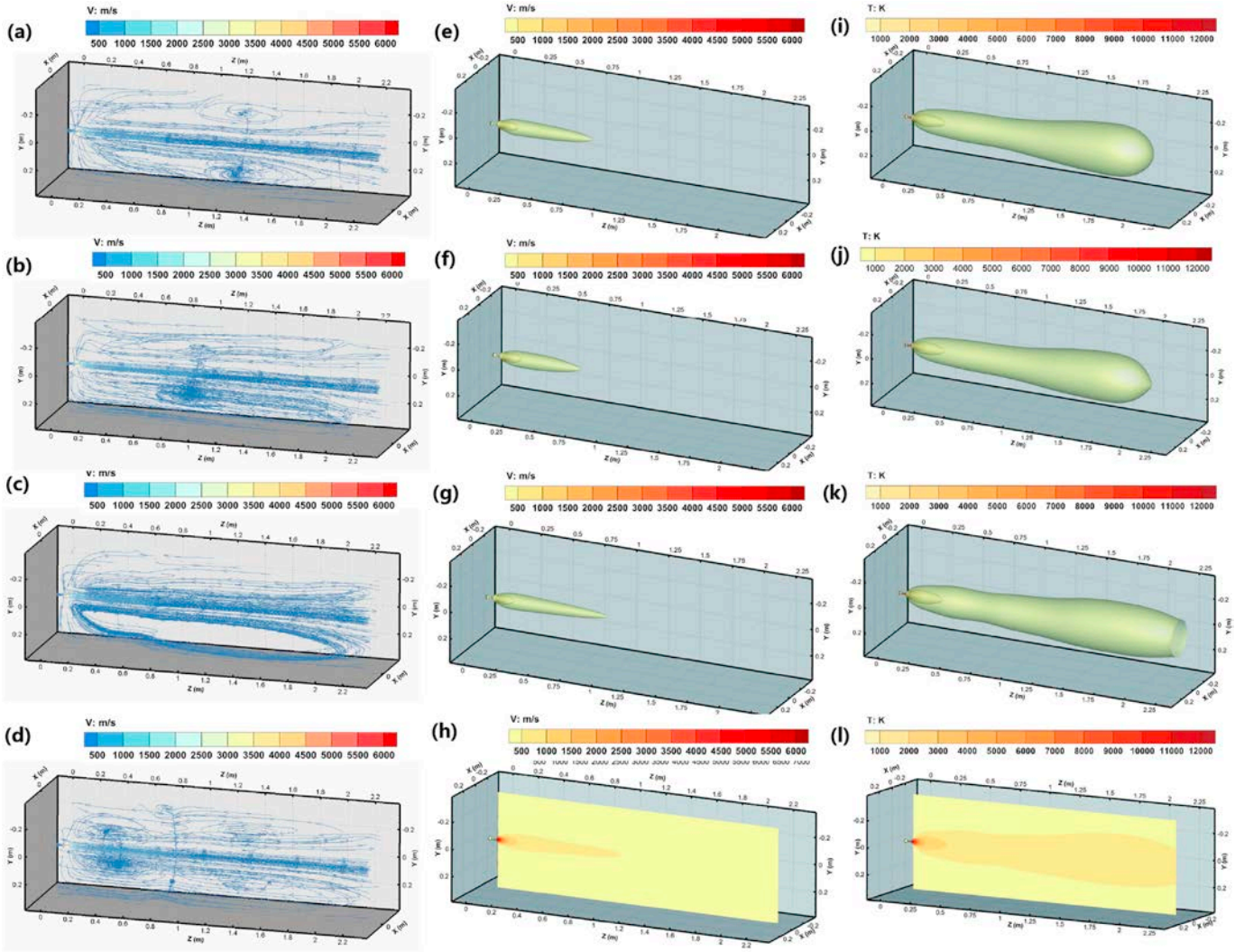

Fig. 10. Transient fluid characteristics at intervals of 10^{-5} s of the low-pressure plasma jet at a chamber pressure of 200 Pa and an input current of 2000 A using 30 SLPM Ar and 60 SLPM He: Realizable K-ε modelling fluid streamlines in (a), (b), (c); three-dimensional velocity distributions in (e), (f), (g) and cross-sectional distribution in (h); three-dimensional temperature distributions in (i), (j), (k) and cross-sectional distribution in (l).

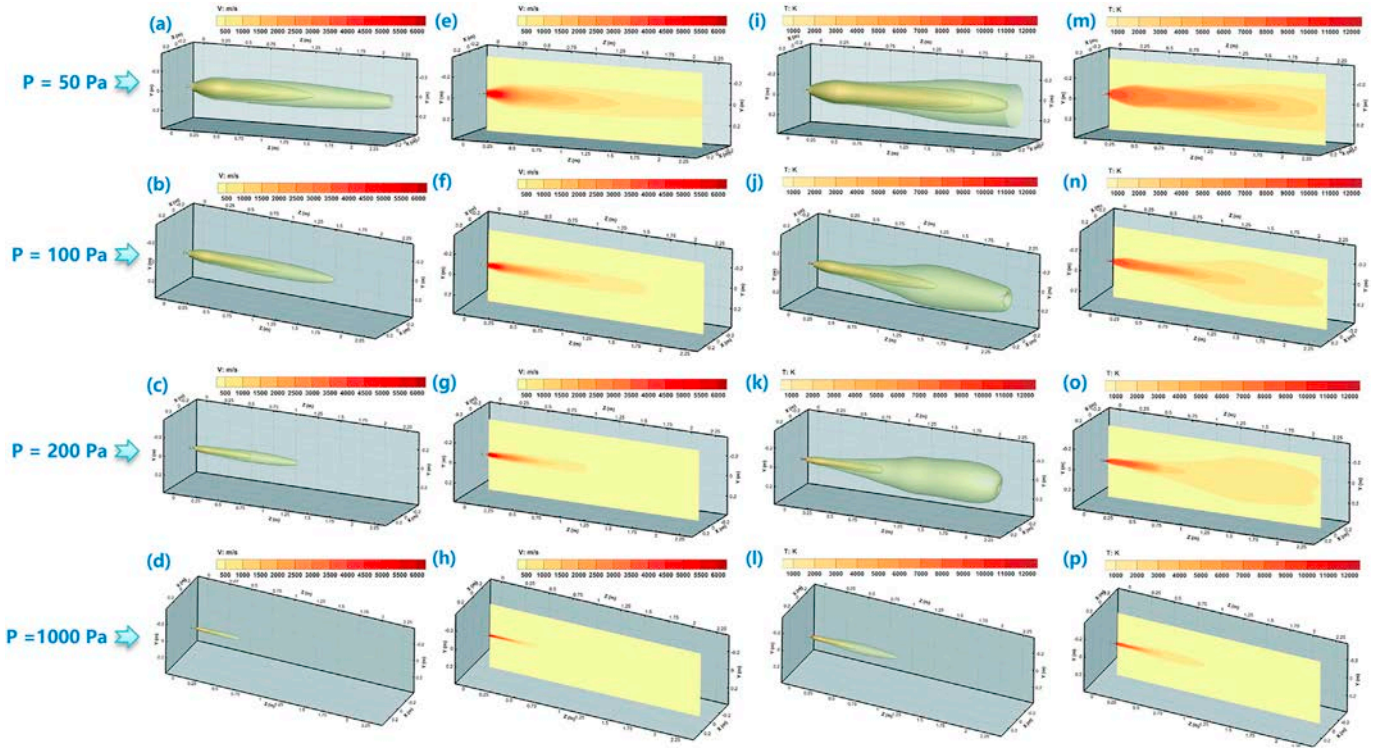

Fig. 11. Velocity and temperature distributions of RSM models in a three-dimensional domain at different chamber pressures (I = 2000 A, 30 SLPM Ar + 60 SLPM He). Chamber pressure of 50 Pa: velocity iso-surface (a), velocity cross-section (e), temperature iso-surface (i), temperature cross-section (m). Chamber pressure of 100 Pa: velocity iso-surface (b), velocity cross-section (f), temperature iso-surface (j), temperature cross-section (n). Chamber pressure of 200 Pa: velocity iso-surface (c), velocity cross-section (g), temperature iso-surface (k), temperature cross-section (o). Chamber pressure of 1000 Pa: velocity iso-surface (d), velocity cross-section (h), temperature iso-surface (l), temperature cross-section(p).

$$Q_{conv} = 4\pi r_p^2 h_f (T_g - T_p) \tag{36}$$

$$Q_{vap} = m_v \left[L_v + \left(H_f - H_P \right) + (H_l - H_s) \right] \tag{37}$$

$$Q_{rad} = 4\pi r_p^2 \varepsilon_p \sigma_p \left(T_p^4 - T_\infty^4 \right) \tag{38}$$

where h is the heat-transfer coefficient, σ is the Stefan-Boltzman constant, ε is the emissivity, T_p is the particle surface temperature, T_g is the surrounding plasma temperature, L_v is the latent heat of vaporization, and m_v is the vaporization mass rate, which is controlled either by vapor diffusion or heat transfer through the boundary layer around the particle. Generally, the particles enter the plasma jet at a low temperature in the beginning, and convective heat transfer dominates the heating stage. Subsequently, radiative heat transfer becomes significant after the particle approaches its maximum temperature. Thereafter, the mass transfer on the particle surface that caused by vaporization significantly reduces the convective heat transfer on the particle surface and constrains the vaporization rate.

- Physical vaporization without chemical reactions on the surface of powders

The physical vaporization of ceramic powders in the PS-PVD process generally occurs when the surface temperature approaches the boiling point of this material. The material changes from the solid (s) or liquid (l) into the vapor (g) phase.

The effect of vaporization on heat and momentum transfer is expected to reduce the drag force owing to the thickening of the boundary layer. Other effects may include change in the position of flow separation, a steep variation in the mixture properties, and an unbalanced momentum flux over the surface of the particle owing to vaporization [236].

A primary consequence of the vaporization of the ceramic powders is the effect of mass transport on convective heat transfer and modification of the transport properties surrounding the particles. Vapor can modify the heat transfer between the plasma and the particles and act as a thermal buffer. Vaporization will decrease the heat transfer to the particle surface because part of the enthalpy from the surface of the particle is used to provide the latent heat of vaporization and to heat the vapor [237].

Moreover, vaporization can, in some cases, contribute to the increase in the plasma temperature. Liu et al. (2017) showed that an energy balance existed between the molten ZrO_2 and the low-pressure plasma jet over a long spraying distance [238]. The result indicated that the molten ZrO_2 at 3247 K with a diameter of 0.28 μm can be completely evaporated at the spraying distance of 450 mm. When the surface temperatures is lower than the boiling point, vaporization is controlled by the intrinsic vapor pressure of the particle and is limited by the diffusion of vapor through the boundary layer surrounding the particle surface. These are determined by the vaporization processes at the surface of the particle (Langmuir vaporization) and mass transfer of species across the boundary layer [239]. Vardelle et al. (1997) recommended that the Langmuir expression is suitable for the vacuum environment and that the mass diffusion must be considered for plasma spraying [240].

Faeth (1983) proposed a vaporization rate controlled by vapor diffusion through the boundary layer around the particle as follows [235]:

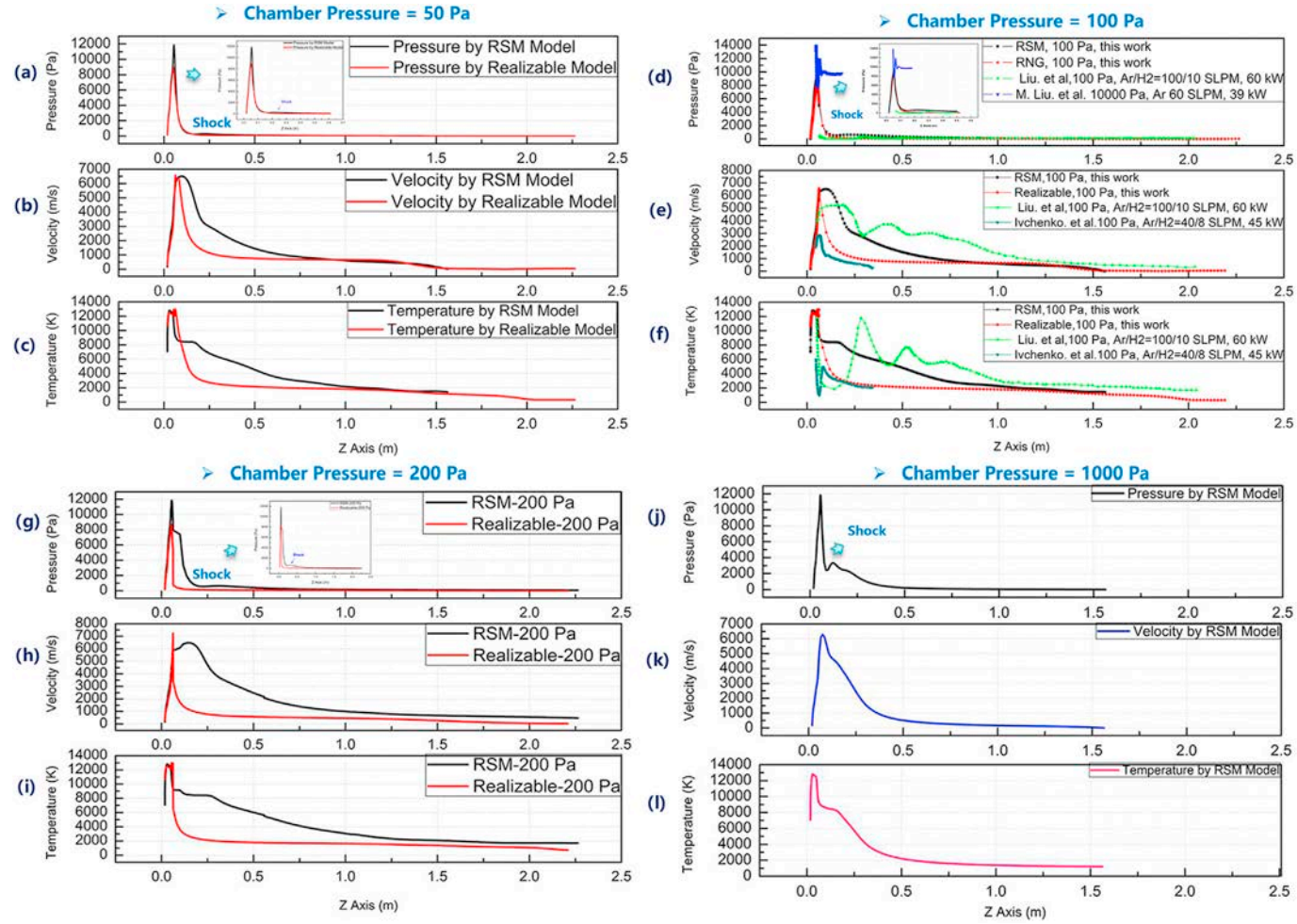

Fig. 12. Axial dependence of properties on-axis for the PS-PVD torch obtained using RSM and Realizable turbulent models. Chamber pressure of 50 Pa: (a) pressure, (b) velocity, (c) temperature. Chamber pressure of 100 Pa: (d) pressure, (e) velocity, (f) temperature and comparison with the results from M. J. Liu et al. (100 SLPM Ar+ 10 SLPM H_2, 60 kW, 100 Pa) [254], Ivchenko et al. (40 SLPM Ar+ 8 SLPM H_2, 45 kW, 100 Pa) and M. Liu et al. (60 SLPM Ar, 39 kW, 10000 Pa) [252]. Chamber pressure of 200 Pa: (g) pressure, (f) velocity, (i) temperature. Chamber pressure of 1000 Pa: (j) pressure, (k) velocity, (l) temperature.

$$m_v = 2(\rho D_p)\pi r_p \ln(1+B)Sh \tag{39}$$

Wan et al. (2002) provided a simple expression of the rate of vaporization using the following equation [241]:

$$m_v = Q_{net}/L_v \tag{40}$$

Q_{net} (W) is the net heat transfer to the particle surface. This means that the vaporization rate (m_v) increases rapidly as the particle surface temperature approaches the boiling point. Subsequently, the vaporization rate is limited by the heat transfer rate to the surface of the particles.

The above governing equations were solved in the ANSYS Fluent16.0 commercial software using the SIMPLE algorithm [242]. Fluent has the basic capabilities to solve the conservation equations of continuity, momentum and energy. The equations and relationships to determine the electric potential, magnetic vector potential, electric field, magnetic induction vector, and electric current density vector were solved via Fluent's user-defined memory, user-defined scalar, and user-defined functions [242].

3.3. Fluid characteristics of the plasma jet in different reduced pressure conditions

The predicted time-dependent flow streamlines, and velocity and temperature distributions of the low-pressure plasma jet at an input current of 2000 A and a chamber pressure of 200 Pa using 30 SLPM argon and 60 SLPM helium in a three-dimensional domain are shown in Fig. 10 at an interval of 10^{-5} s. A high-speed swirling flow is predicted to propagate in the closed chamber, generating back flows or vortex flows between the chamber wall and the plasma jet (Fig. 10-a to 10-d). The maximum velocity of the low-pressure plasma jet was greater than 6000 m/s under this condition. The velocity iso-surfaces and cross-section distributions were determined using the realizable K-ε turbulent transport model (Fig. 10-e to 10-h). An expanding flow was obtained outside the torch nozzle and featured a long plasma jet with a maximum distance of 1200 mm. The time-dependent temperature iso-surface distributions are shown in Fig. 10-i to 10-k. The low-pressure plasma plume was continuously expanded when it was sprayed from the torch nozzle, particularly in the wake of the plasma jet (distance from 1750 mm to 2000 mm). The low-pressure plasma jet finally developed to form an expansive flow at the cross-section (Fig. 10-l), which is frequently observed in experiments.

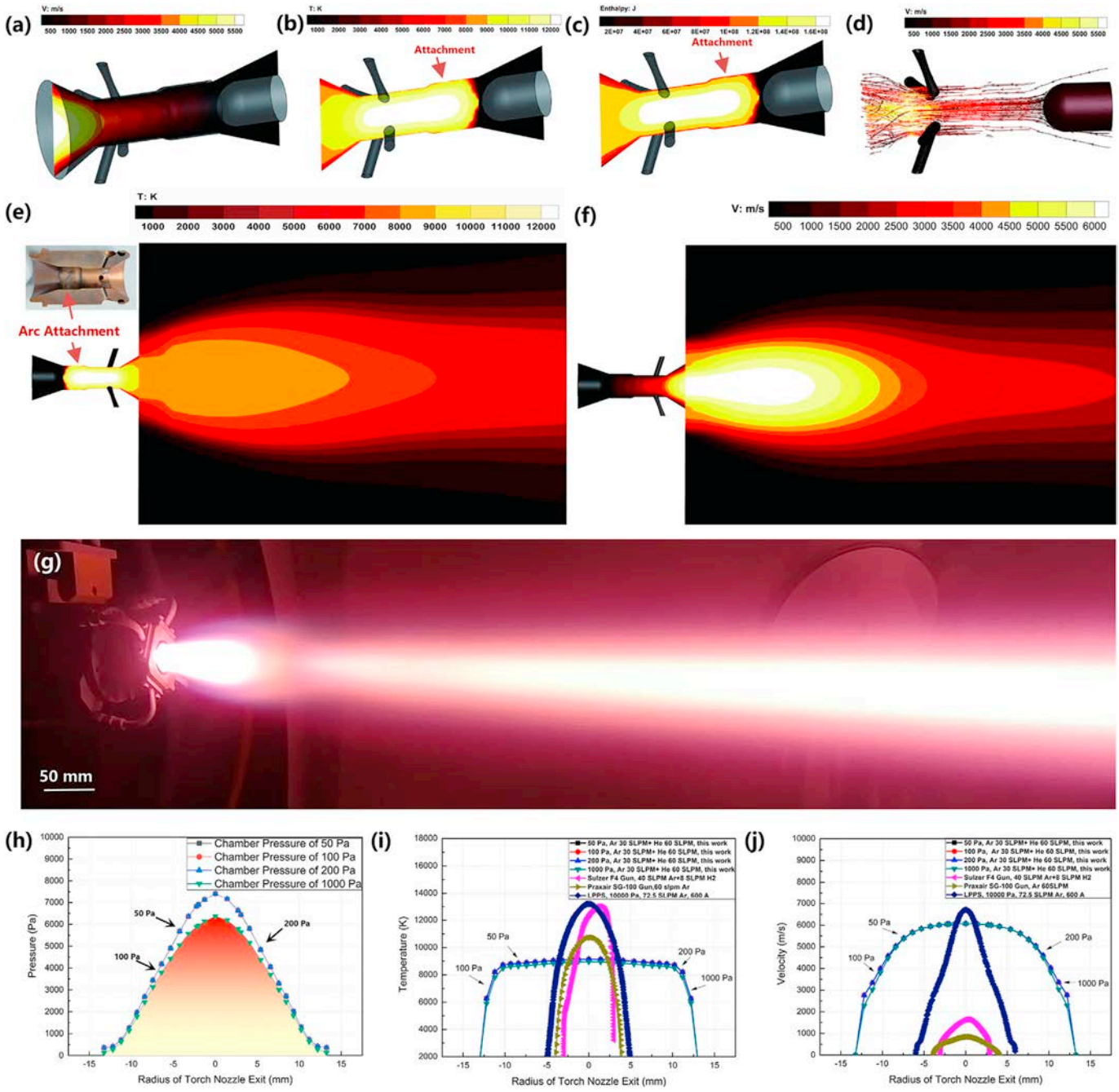

Fig. 13. Velocity (a), temperature (b), enthalpy (c) and flow streamlines (d) distribution inside the plasma spray torch (I = 2000 A, P = 100 Pa, Ar/He = 30/60 SLPM); temperature (e) and velocity (f) distributions with the plasma jet area at the torch nozzle exit (d = 27 mm, I = 2000 A, 100 Pa, Ar/He = 30/60 SLPM); photograph of the low-pressure plasma jet (g); pressure (h), temperature (i) and velocity (j) distributions at the cross-section of the torch nozzle at the chamber pressure of 50 Pa, 100 Pa, 200 Pa, 1000 Pa, including comparisons with the modelling results from Praxair SG-100 Plasma Torch (d = 8 mm, I = 800 A, Ar = 60 SLPM), the Sulzer-Metco F4 Plasma Gun (d = 6 mm, I = 400 A, Ar/H_2 = 40/8 SLPM) and a LPPS system (d = 12 mm, I = 600 A, Ar = 72.5 SLPM, P = 10000 Pa).

Moreover, we ran the simulation using the RSM turbulent transport equations, which is reported to be suitable for the highly swirling flows [208,209]. Fig. 11 shows the velocity and temperature distributions at the chamber pressure of 50 Pa, 100 Pa, 200 Pa and 1000 Pa in the three-dimensional domain by using 30 SLPM argon and 60 SLPM helium and the RSM turbulent model. They show different fluid characteristics compared with the results obtained using the realizable K-ε turbulent transport model (Fig. 10). A more concentrated area of high velocity and high temperature at the cross-section was obtained under the same initial conditions. The maximum velocity decreased as the chamber pressures increased from 50 Pa to 1000 Pa, while the velocity iso-surface distributions indicate that the plasma jet rapidly expanded axially and radially (Fig. 11-a to 11-d). The corresponding velocity distributions in the cross-sections are depicted from Fig. 11-e to 11-h.

Similarly, the temperature iso-surface distributions decreased both axially and radially as chamber pressure increased (Fig. 11-i–11-l), although the plasma gas temperature was still over 1000 K at a distance of 1000 mm under a chamber pressure of 1000 Pa. An strongly expanding region was generated at the wake of the plasma

Table 4
Predicted maximum velocity, maximum temperature and other properties in low-pressure plasma spray systems.

Authors	Operating Parameters	Plasma Gases and Flow Rate (SLPM)	Mach Number	Maximum Enthalpy (J/mol)	Maximum Velocity (m/s)	Maximum Temperature (K)	Maximum Heat Flux (W/m^2)	YSZ Flight Velocity (m/s)	YSZ Flight Temperature (K)	YSZ Flight time (s)	Reference
Peng Han and Xi Chen (2001)	P = 10000 Pa I = 600 A U = 40 V	72.5 SLPM Ar	2.8	/	6900	13200	/	/	/	/	[246,247]
Mauer G & Vaßen R et al. (2014)	P = 200 Pa; I = 2600 A;	35 Ar + 60 He	2.1	/	~6000	15500	/	/	/	/	[248]
Vautherin. et al. (2014)	P = 150 Pa; I = 650 A; U = 73 V	45 Ar +10H_2	/	/	3350	5500	/	/	/	/	[249]
Ming Liu &W. Kui et al. (2015)	P = 10000 Pa 65 kW	65 Ar	/	/	5400	14700	/	/	/	/	[250]
Anwaar, A. et al. (2017)	P = 100 Pa; I = 2300 A; U = 30.4 V	35 Ar + 60 He	/	838965 J/mol	6000–8000	12000 –16951	2×10^8 ~ 5.5×10^8	/	/	36–40 us	[251]
A. Vardelle & D. Ivchenko et al. (2018)	P = 100 Pa; I = 600 A; U = 75 V	40 Ar + 8H_2	/	/	~7000	14200	/	/	/	/	[252,253]
M. J. Liu & G. J.Yang et al. (2019)	P = 100 Pa; 60 kW	100 Ar + 10H_2	/	/	~4200	7800	/	/	/	/	[254,255]
	P = 100 Pa	35 Ar + 60 He	/	/	~4000	10100	/	/	/	/	[256]
Zhang Tao & C. J. Li. (2021)	P = 100 Pa I = 2300 A	60 Ar + 30 He	4–5	/	6000–8000	18500	/	/	/	/	[257]
	P = 100 Pa I = 750 A	40 Ar+ 8H2	5–7	/	7000–7900	16550	/	/	/	/	[257]
This Work	P = 50 Pa; I = 2000 A;	30 Ar + 60 He	3.53	1.663×10^8 J/kg	6519.4	12850.7	539693	0.47–6432	300–4548	0–0.4	/
	P = 100 Pa; I = 2000 A;	30 Ar + 60 He	3.48	1.663×10^8 J/kg	6508.6	12849.3	539114	0.47–6432	300–4548	0–0.4	/
	P = 200 Pa; I = 2000 A;	30 Ar + 60 He	3.44	1.657×10^8 J/kg	6474.8	12823.7	539611	0.47–6300	300–4548	0–0.4	/
	P = 1000 Pa; I = 2000 A;	30 Ar + 60 He	3.42	1.656×10^8 J/kg	6294.2	12826.5	538912	0.47–6000	300–4548	0–0.4	/

plume, and the plasma jet was expanded to over 200 mm in the radial direction at chamber pressures of 50 Pa, 100 Pa, and 200 Pa.

The center axis attenuation of the plasma gas pressure, velocity and temperature on axis from the cathode tip of the plasma torch to the plasma jet area at four different chamber pressures is shown in Fig. 12. An apparent pressure gradient was observed at the chamber pressures of 50 Pa, 100 Pa, 200 Pa and 1000 Pa, corresponding to a shock region outside the torch nozzle, and the velocity of the plasma gas increased abruptly after exiting the torch nozzle. The temperature from the realizable turbulent model rapidly decreased to 3000 K at a distance of 250 mm from the plasma jet area. However, a gradual attenuation of the temperature using the RSM turbulent model was observed at the four different chamber pressures.

For the chamber pressure of 100 Pa (Fig. 12-d to 12-f), the predicted on-axis attenuation were compared with the results at the same chamber pressure obtained by Liu et al. (2015) using 60 SLPM argon at an input power of 39 kW and a chamber pressure of 10000 Pa [250], Ivchenko & Vardelle et al. (2018) using 60 SLPM argon and 8 SLPM hydrogen at an input power of 45 kW and a chamber pressure of 100 Pa [252], and Liu et al. (2018) using 100 SLPM argon and 10 SLPM hydrogen at an input power of 60 kW and a chamber pressure of 100 Pa [254]. Intense fluctuations in the pressure in the vicinity of the torch nozzle were observed from these results, and a shock area existed in the low-pressure plasma flow. Thereafter, the pressure of the plasma jet was stabilized to the chamber pressure. Moreover, the velocity and temperature attenuation were significantly different when using different turbulent transport models for the low-pressure plasma flow. The turbulent transport of the plasma plume and chamber pressure all affected the velocity and temperature fluctuations in the plasma jet when it flowed from the high-pressure the plasma torch region to the low-pressure chamber region.

3.4. Fluid characteristics at the nozzle exit of the PS-PVD torch

The predicted flow characteristics inside the PS-PVD torch are shown in Fig. 13-a–13-d. The maximum velocity of the plasma gas inside the plasma torch was less than 6000 m/s, but the maximum plasma velocity outside the torch nozzle shown in Fig. 13-f was approximately 6508 m/s. This indicates that the plasma gas was accelerated after it was ejected from the torch nozzle because of the large pressure gradient between the region inside the plasma torch, and the plasma jet.

An apparent arc column was observed from the cathode tip to the torch nozzle in Fig. 13-b and Fig. 13-e with a part of plasma jet area. The arc attachment position is indicated and corresponded to the location of erosion of the anode in experiments (Fig. 13-e). The erosion was found to affect strongly the state of the jet flow downstream [157,181]. The plasma temperatures near the torch nozzle are shown in Fig. 13-e, and these distribution corresponds to the observed emission from the jet shown in Fig. 13-g. The plasma gas temperature abruptly decreased nearby the torch nozzle and expanded in the radial direction, particularly in the shock area (Fig. 13-f). Thereafter, it changed to a uniform jet flow, similar to that observed experimentally.

The distributions of the plasma gas pressure, temperature and velocity at the cross-section of the torch nozzle are shown in Fig. 13-h, 13-i and 13-j, respectively. These results were compared with those calculated for the Praxair SG-100 Plasma Torch (d = 8 mm, I = 800 A, Ar = 60 SLPM) [243], Sulzer-Metco F4 Plasma Gun (d = 6 mm, I = 400 A, Ar/H_2 = 40/8 SLPM) [212] in an atmospheric environment and an LPPS system (d = 12 mm, I = 600 A, Ar = 72.5 SLPM, P = 10000 Pa) [244]. The plasma gas pressure at the

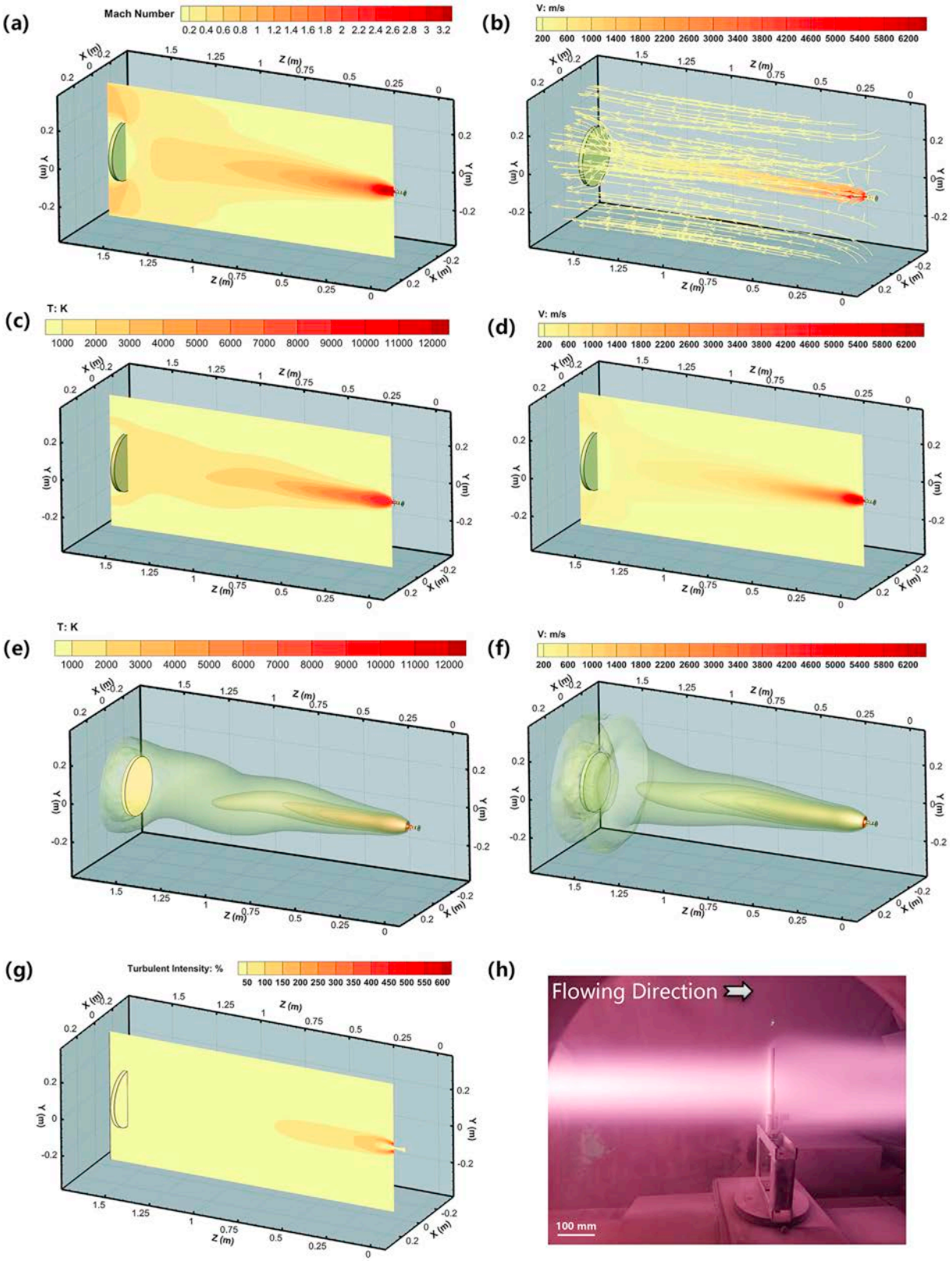

Fig. 14. Numerical simulation the low-pressure plasma spray process (P = 100 Pa, I = 200 A, 30 SLPM Ar + 60 SLPM He, spraying distance of 1500 mm): Mach number (*Ma*) (a); plasma jet flow streamlines distributed in a three-dimensional area (b); temperature (c) and velocity (d) distributions in a sliced cross-section plane; temperature (e) and velocity (f) iso-surface distributions in the three-dimensional domain; turbulent intensity (%) (g); photograph of the low-pressure plasma jet impinging on a substrate (h).

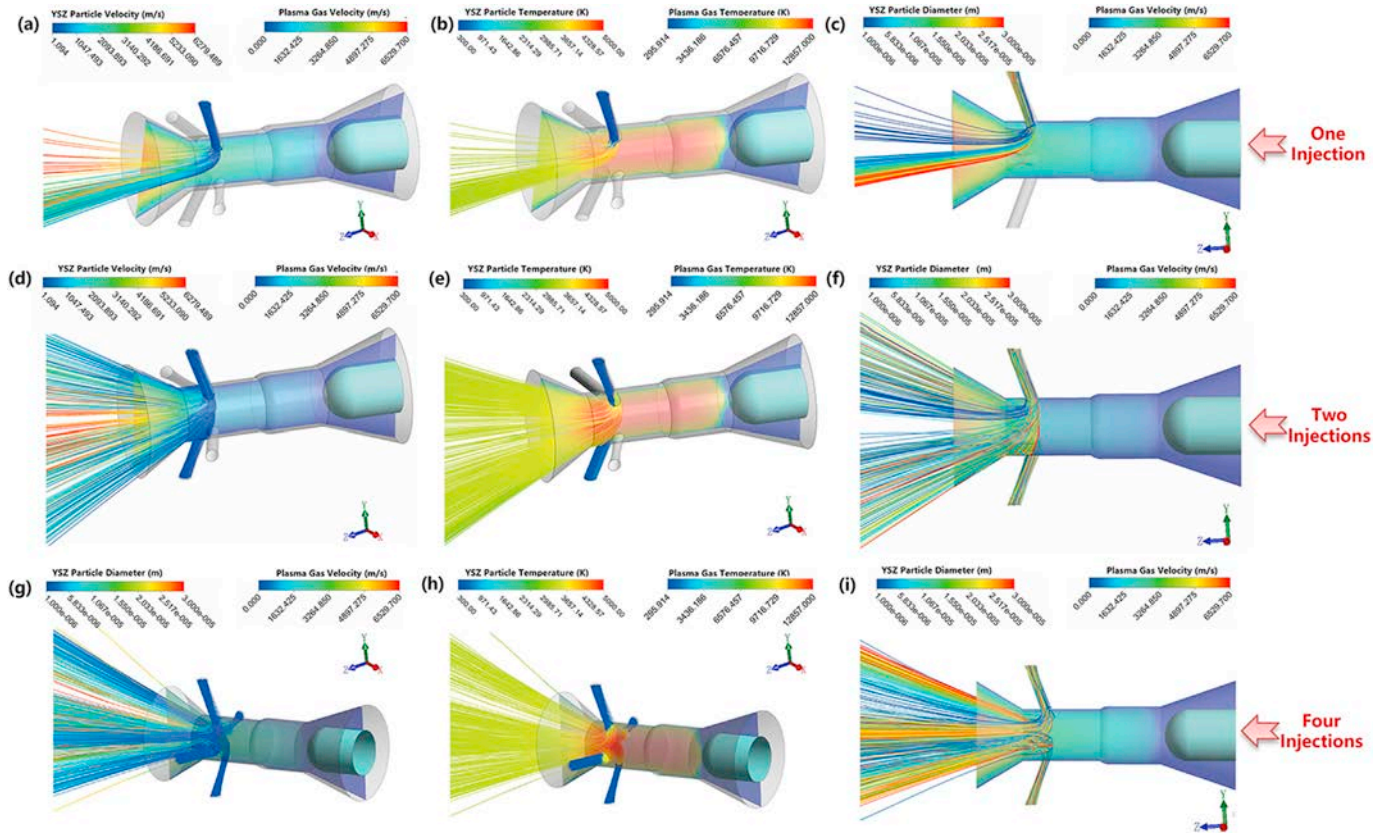

Fig. 15. YSZ particle (d = 1–30 μm) flight characteristics inside the PS-PVD torch (P = 200 Pa, I = 2000 A, 30 SLPM Ar + 60 SLPM He): one-way injection of particles by carrier gases (10 SLPM Ar, 4 g/min): (a) plasma gas velocity distribution that combined with particle velocity; (b) plasma gas temperature and particle temperature; (c) plasma gas velocity and particle diameters along the cross-section of the torch; two-way injections of particles by carrier gases (2 × 10 SLPM Ar, 2 × 4 g/min): (d) plasma gas velocity and particle velocity; (e) plasma gas temperature and particle temperature; (f) plasma gas velocity and particle diameters along the cross-section of the torch; four-ways injections of particles by carrier gases (4 × 10 SLPM Argon, 4 × 4 g/min): (d) plasma gas velocity and particle velocity; (e) plasma gas temperature and particle temperature; (f) plasma gas velocity and particle diameters along the cross-section of the torch.

torch nozzle was significantly higher than the chamber pressure because the high-temperature plasma gas was constricted in the small channel structure of the plasma torch. Nevertheless, the plasma gas pressure was slightly affected by the low chamber pressure. The profile of the plasma gas pressure (P_{out}) at the torch nozzle in this work followed the Gauss-Amp (amplitude version of the Gaussian peak function) distribution [245] as a function of the torch nozzle diameter (d). Using the chamber pressure of 200 Pa as an example,

$$P_{out} = -798.18 + 8140.80 \times e^{-\frac{(d-0.01)^2}{80.78}} \quad (41)$$

where P_{out} is in Pa and d is in mm.

The plasma gas temperature at the torch nozzle exit was not affected by the variation in the chamber pressure (Fig. 13-i). The maximum plasma gas temperatures at the torch nozzle exit under the chamber pressures of 50 Pa, 100 Pa, 200 Pa and 1000 Pa were 12851 K, 12849 K, 12824 K and 12827 K, respectively. The maximum temperatures at the torch nozzle exit for the Praxair SG-100 Plasma Torch using 60 SLPM argon at a current of 800 A and the Sulzer-Metco F4 Plasma Gun using 40 SLPM argon and 8 SLPM hydrogen at a current of 400 A were higher than those in this work. This is likely a consequence of the much larger diameter of the PS-PVD torch.

The plasma gas velocity at the torch nozzle exit increased slightly as the chamber pressure decreased. The maximum plasma gas velocities at the torch nozzle at chamber pressures of 50 Pa, 100 Pa, 200 Pa and 1000 Pa are 6084 m/s, 6072 m/s, 6069 m/s and 6007 m/s (Fig. 13-i), respectively. These values are much larger than for the atmospheric plasma spray torches, despite the lower temperature.

In simulations of the plasma spray process, accurate values of the velocity, temperature, and pressure at the torch nozzle exit are required to obtain reliable results. However, a simulation of low-pressure plasma spray has to consider the flow both inside and outside the plasma torch in the closed chamber owing to the high pressure gradient.

In Table 4, we list the numerical predicted maximum velocity, temperature, and other parameters for current LPPS methods under different operating conditions. In this work, the results were close to those of Mauer et al. (2014) [248] and Anwaar et al. (2017) [251] at similar operating conditions. Generally, the plasma gas temperature in other reported results were based on the input power and the gases used, while the plasma gas velocities were all very high. The predicted Mach number of the low-pressure plasma jet at four different chamber pressures ranged from 3.43 to 3.53.

3.5. Fluid characteristics in low-pressure plasma jet - substrate impingement

The low-pressure plasma spray process was modeled for the case of the plasma jet impinging on a circular substrate (d = 300 mm, δ = 5 mm, spraying distance 1500 mm). Results are shown in Fig. 14 and compared with experimental observations in

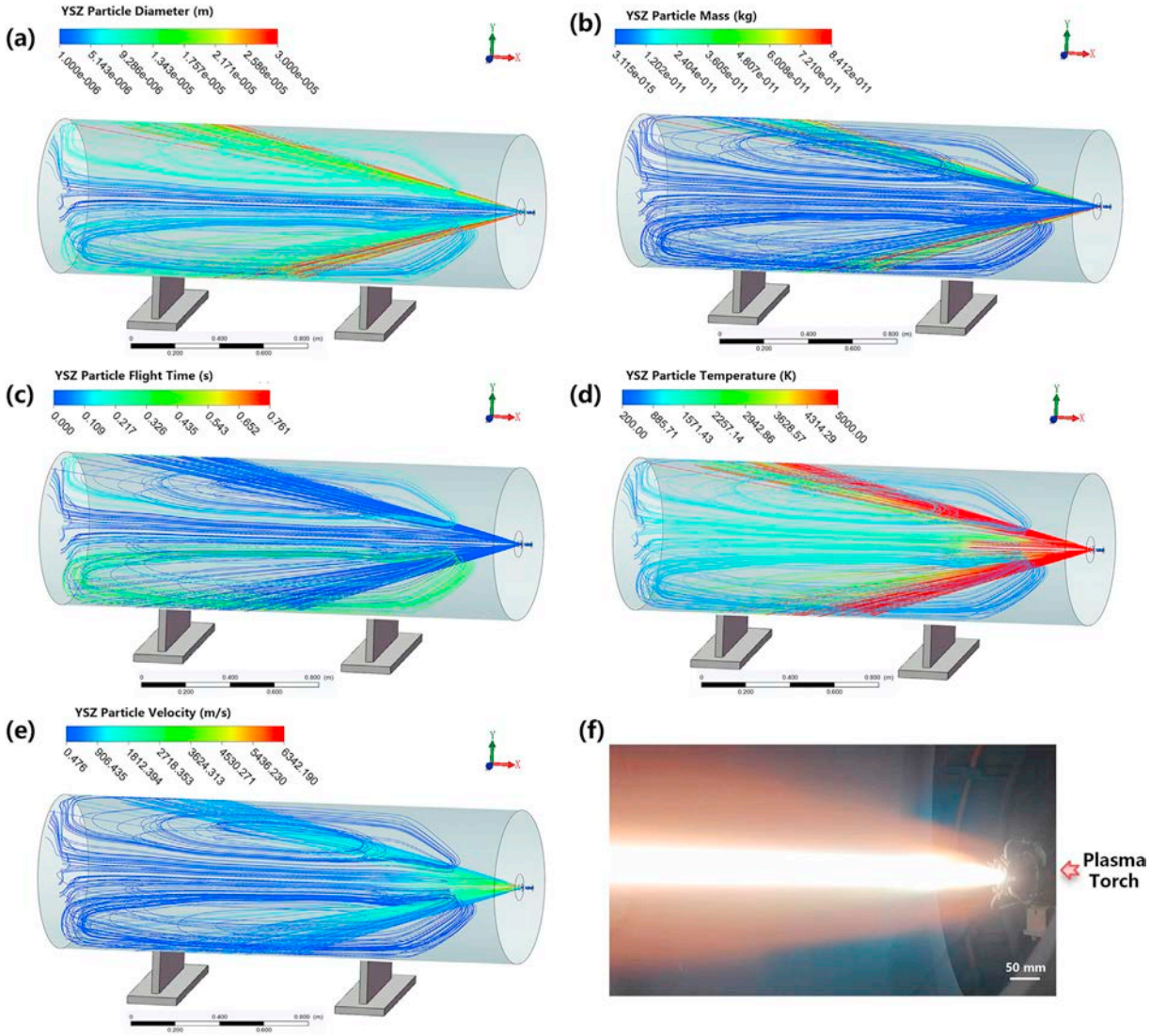

Fig. 16. Overall views of the flight trajectories of YSZ particles (4 g/min, d = 1–30 μm) in a three-dimensional domain extending the plasma torch area to plasma jet region (P = 200 Pa, I = 2000 A, 30 SLPM Ar + 60 SLPM He, SD = 2200 mm) using two-way injection with carrier gases (2 × 10 SLPM Argon, 2 × 4 g/min): particle diameter distribution (a); particle mass distribution (b); particle flight time (c); particle temperature (d); particle velocity (e); photograph of the region near the torch nozzle with the YSZ particles under the same conditions (f).

Fig. 14- h.

The calculated maximum Mach number (*Ma*) was 3.48 in this case, with larger values near the torch nozzle and the edge of the substrate. The flow streamlines of the low-pressure plasma jet in the three-dimensional domain are shown in Fig. 14-b; they indicate strong entrainment at the torch nozzle and around the substrate.

The temperature and velocity contour distributions in a cross-section are depicted in Fig. 14-c and 14-d, respectively. The iso-surface temperature and velocity in the three-dimensional domain are shown in Fig. 14-e and 14-f, respectively. The plasma temperature rapidly decreased to 1500 K near the surface of the substrate at a spraying distance of 1500 mm. The plasma gas was rapidly impinging on the substrate in vertical direction and flowing bypass the edge of the substrate. The low-pressure plasma plume expanded near the torch nozzle, similarly to the result of the free flow jet shown in Fig. 13. The plume is predicted to flow around the edge of the circular substrate in agreement with the experimental observation shown in Fig. 14-h.

The turbulence intensity is defined as the ratio of the root-mean-square of the velocity fluctuations to the mean flow velocity [205]. If the flow is fully developed, the turbulence intensity may be as high as a few percentages. The results of turbulent intensity using the RSM turbulent transport model show a maximum of over 600 % outside the torch nozzle (Fig. 14-g). The turbulent intensity gradually decayed to below 50 % at a spraying distance of 750 mm.

3.6. Particle heating and motion in low -pressure plasma spraying

The simulations of particle injection with the carrier gas through one, two or four injections points into the plasma torch are shown in Fig. 15. With the use of a one-way injection of YSZ particles (Metco 6700, YSZ, d = 1–30 μm, Oerlikon Metco. Inc., Westbury, USA) with the carrier gas (10 SLPM Argon), the particle velocity and temperature in the carrier gas pipe were all very low (Fig. 15-a and 15-b), although the smaller particles (diameter less than 5 μm) rapidly accelerated to over 6000 m/s after they were injected inside the plasma torch channel, and their tracked trajectories noticeably ascended along the cross-section (Fig. 15-c). The velocity of the

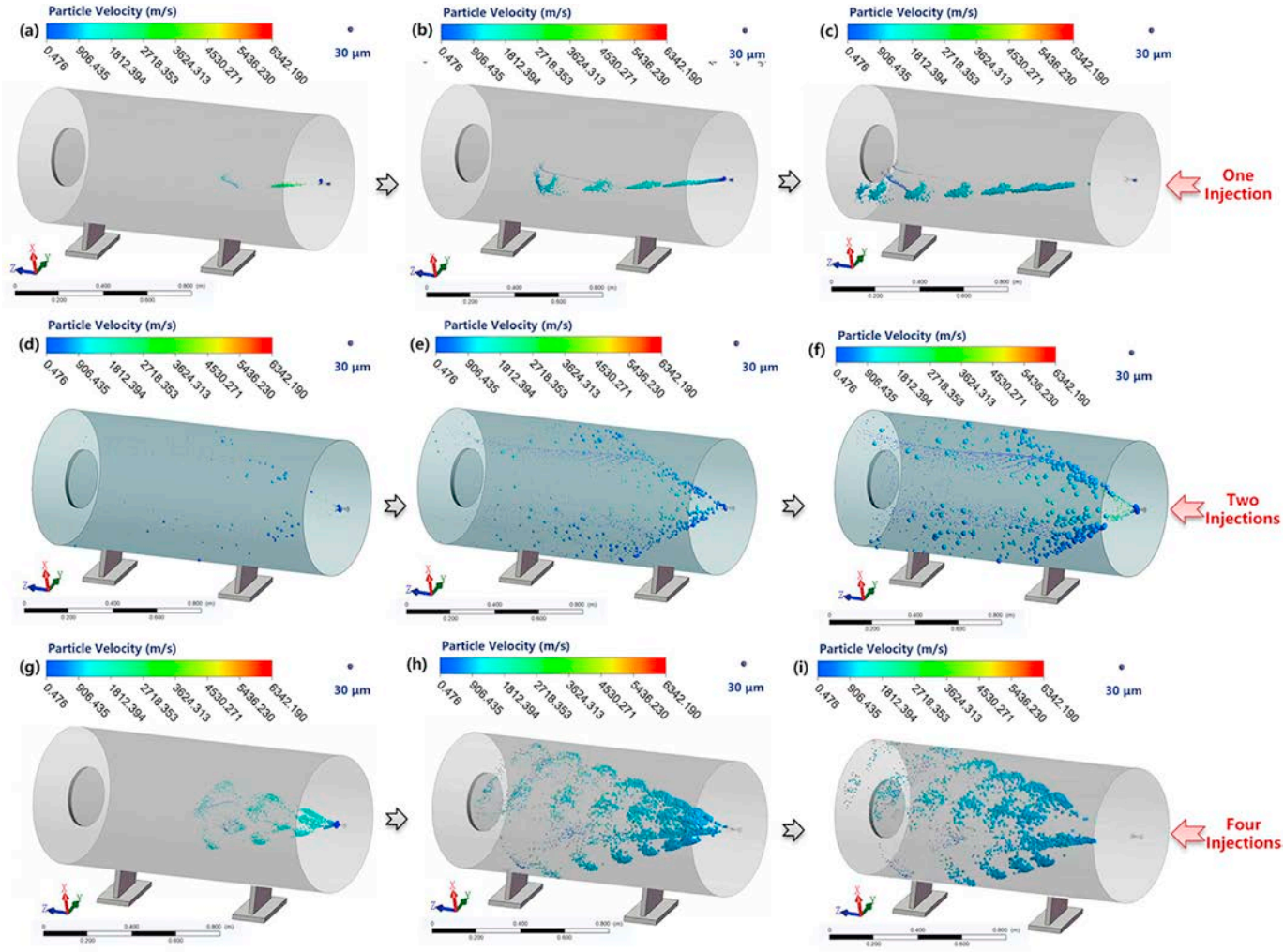

Fig. 17. Time-dependent YSZ particle (4 g/min, d = 1–30 μm) properties continuous flow (P = 100 Pa, I = 2000 A, spraying distance = 1500 mm, 30 SLPM Ar + 60 SLPM He) at 1 μs intervals for one-way injection of carrier gas (10 SLPM argon, 4 g/min) in (a), (b), (c); two-way injection of carrier gas (2 × 10 SLPM argon, 2 × 4 g/min) in (d), (e), (f); four-way injection of carrier gas (4 × 10 SLPM argon, 4 × 4 g/min) in (g), (h), (i).

larger particles (diameter larger than 10 μm) was smaller than of the smaller-diameter particles, and the tracked trajectories were closer to the axis.

The two-way injection of YSZ particles was conducted at a total feed rate of 8 g/min (Fig. 15-d–15-f), which is the most commonly used method for the manufacturing of TBCs. The particles were accelerated into the torch nozzle, where the smaller particles reached a higher velocity than the larger particles. The maximum particle velocity occurred outside the torch nozzle in the plasma jet shock region. The particles were immediately heated to over 4500 K (the boiling point of zirconia is 4548 K [257]), and the particle temperature then decreased along the flow trajectory. The particles with a diameter of 25–30 μm flowed trajectories close to the nozzle wall and were injected at a large incident angle to the plasma jet axis.

In the four-ways injection of YSZ particles at a total feed rate of 16 g/min, flow characteristics similar to the above results were observed, with the particle temperature immediately increasing to over 4500 K and then decreasing significantly outside the torch nozzle. The maximum particle temperature area was within the torch nozzle. The average particle temperatures near the torch nozzle, as shown in Fig. 15-b, 15-e and 15-h, were all higher than 3600 K.

Fig. 16 shows overall views of the YSZ particle trajectories in low-pressure plasma spray for the same conditions as Fig. 16, with a spraying distance of 2200 mm and two-way injection of particles. As Fig. 16-a shows, the trajectories of particles with diameter of 1–5 μm were along the flow streamlines of the plasma jet to a maximum distance of 2200 mm and close to the centerline. The trajectories of particles with diameter of 5–12 μm were at a larger incident angle to the centerline of the plasma jet. Some of the injected particles flowed through the entrainment flow streamlines of the plasma jet around the chamber wall. The trajectories of particles with diameter of 25–30 μm deviated substantially from the centerline, so that they passed close to the wall of the torch nozzle and were deposited on the chamber wall. Fig. 16-b shows the particle mass distribution along the trajectories where the larger particles exhibited a higher mass concentration, similar to the result in Fig. 16-a.

The flight time of the YSZ particle is shown in Fig. 16-c. The flight times of all particles were generally short, although the particles that flowed backwards had a longer flight time from 0.4 s to 0.7 s. The flight time of most particles was less than 0.1 s.

The temperature and velocity distributions of the YSZ particles as they follow the calculated trajectories are shown in Fig. 16-d and 16-e, respectively. An experimental observation near the torch

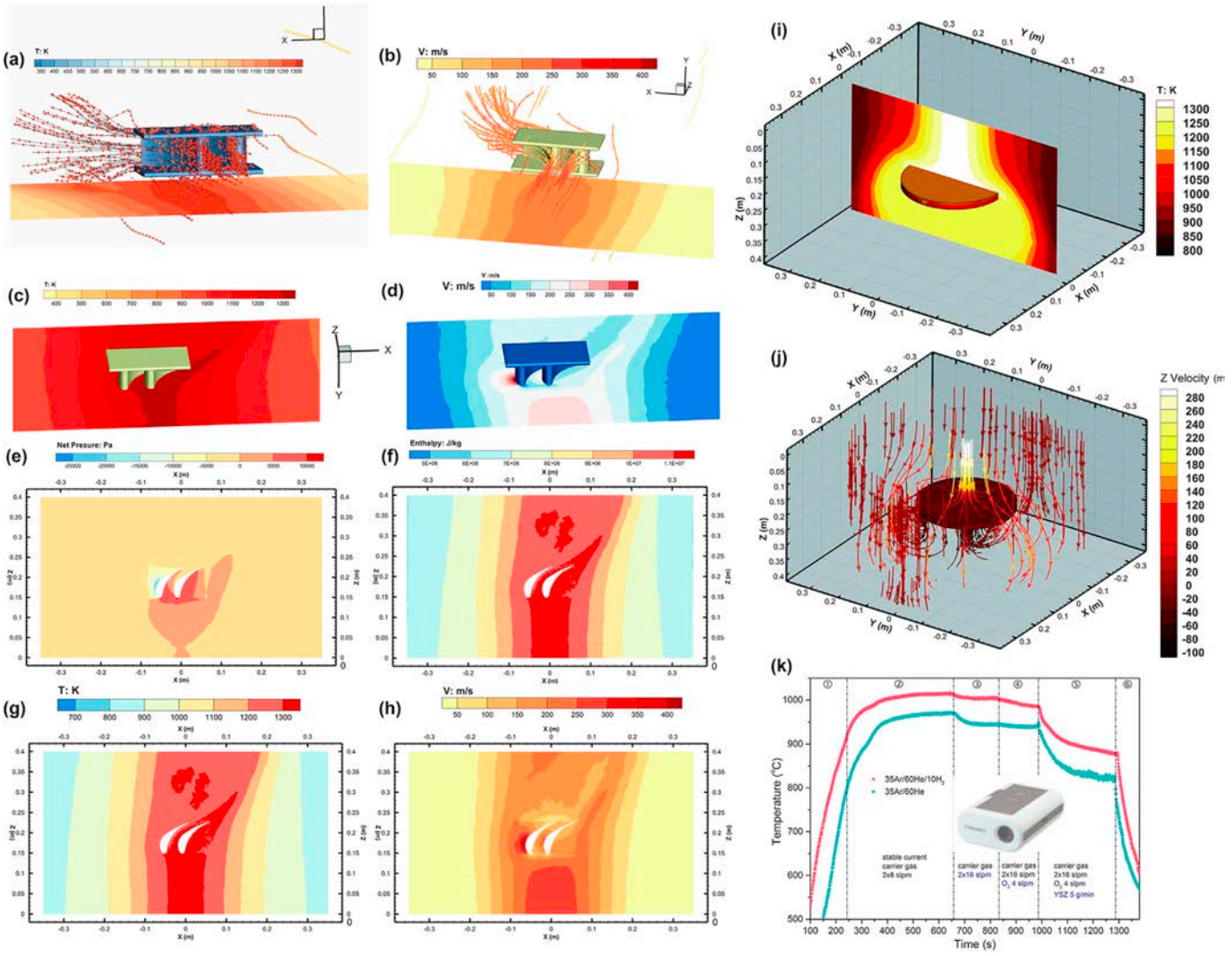

Fig. 18. Three-dimensional simulations of the low-pressure plasma jet impinging on the substrate (chamber pressure of 200 Pa, 2000 A, 30 SLPM Ar +60 SLPM He, SD = 1500 mm): heat flux streamlines (a), velocity streamlines (b); temperature and velocity distribution in a cross-section (c) and (d); impact net pressure (e); enthalpy distribution (f); cross-section temperature distribution (g) and velocity distribution (h) for the double-vane substrate (Inconel 738 alloy); temperature distribution (i) and flow streamlines in the Z-direction (j) for the circular substrate (Inconel 738 alloys); circular substrate temperatures at 200 Pa by using 30 SLPM Ar + 60 SLPM He plasma jet (green curve) and 30 SLPM Ar+ 60 SLPM He+10 SLPM H_2 plasma jet (red curve) measured using a CHINO IR-AP 3CG pyrometer (k) [170] (Reproduced with permission © Elsevier B.V.).

nozzle is shown in Fig. 16- f. All the particles were sprayed at a particular incident angle from the torch nozzle. The jet appeared brighter than a free plasma jet without particle injection. The temperatures of particles of all sizes were high close to the boiling point of zirconia, near the torch nozzle (Fig. 15-e and 16-d). The maximum particle velocity near the torch nozzle reached 6300 m/s in a very small zone and then rapidly decreased to approximately 1500 m/s at a distance of 1000 mm along the trajectories.

The transient characteristics of in-flight YSZ particles in a low-pressure plasma spray are shown in Fig. 17. The flight paths for one-way injection of YSZ particles at an interval of 1 μs are shown in Fig. 17-a–17-c. The results demonstrate that the deposition location on the substrate deviated substantially from the centerline. This is commonly observed in the experiments and has to be avoided in industrial operation.

In the two-way injection of YSZ particles, at a feed rate of 8 g/min, the larger particles with diameters of 25–30 μm as shown in Figs. 15 and 16, were deposited on the wall of the chamber at high velocity and high incident angle. The smaller particle with diameters of 1–5 μm were entrained in the low-pressure plasma plume and were transported downstream, which is widely observed in PS-PVD [16,20,87,255].

In the four-way injection of YSZ particles, larger particles were continuously ejected from the torch nozzle at a mass flow rate higher than for one- or two-way injection, and filled the three-dimensional domain of the chamber. The smaller in-flight particles flowed a long way downstream and trended to divert downward because of gravity.

The multiphase flow characteristics in the PS-PVD process have been described in the section. However, the deposition of the quasi-columnar ceramic coating occurs in the micro-scale boundary layer of the substrate. The formation mechanism of the coatings in the boundary layer is examined in the following section.

4. Formation mechanism of coatings in the PS-PVD process

It is evident that the coating microstructure and the formation of quasi-columnar structures are strongly determined by the development of the particle trajectories close to the substrate, when the particles flight through a super long distance and reach

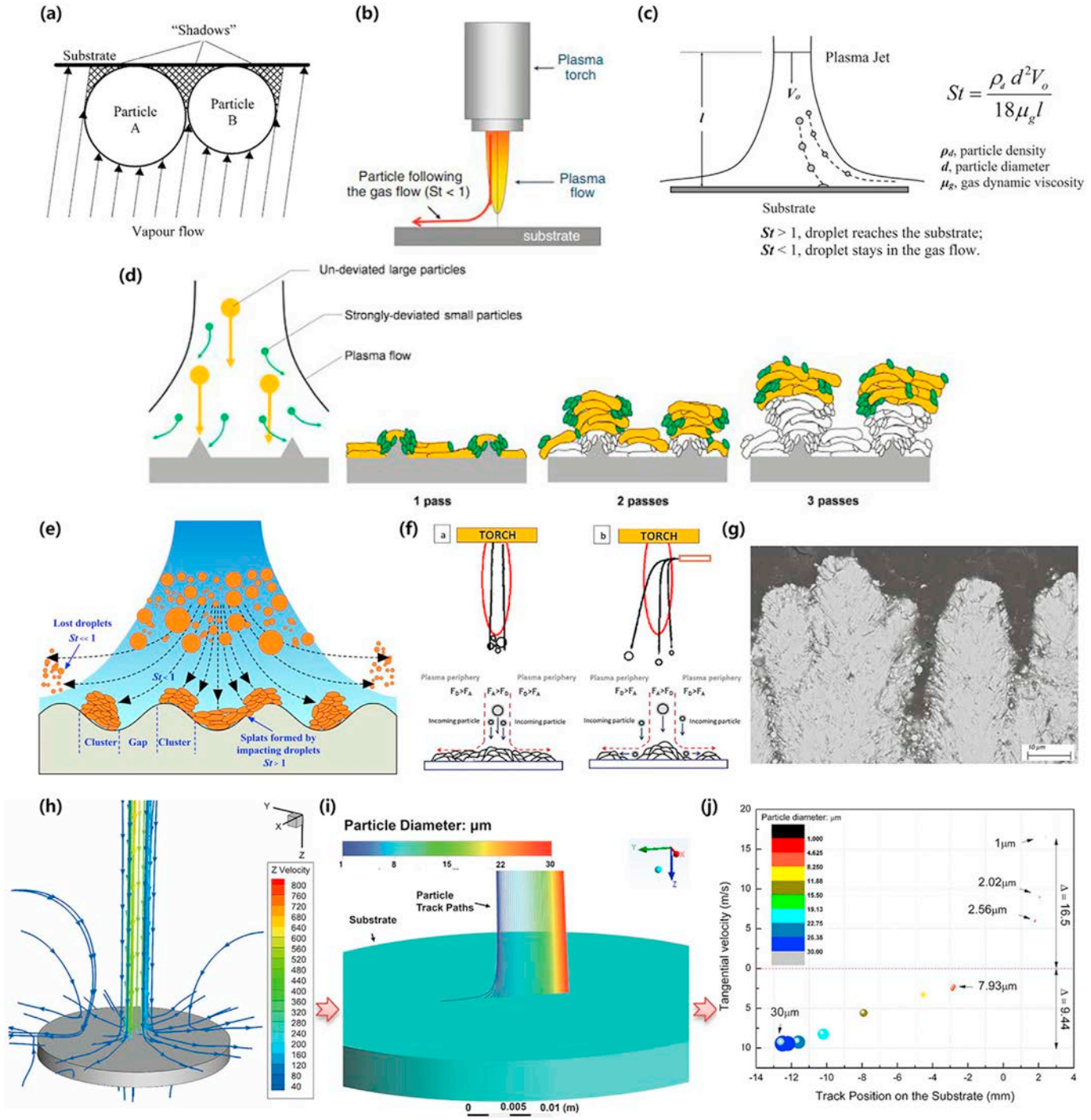

Fig. 19. Schematic diagrams of "shadowing effect or self-shadow effect" for the deposition of quasi-columnar coatings: (a) Movchan. (2006) illustrated the shadowing zones in the vicinity of two particles in the EB-PVD process [272]; (b) Fauchais et al. (2014) showed the particle trajectory along the surface of the substrate for St < 1 [277]; (c) Jordan et al. (2015) gave the Stokes number for in-flight particles and the effect on deposition in the SPPS process [278]; (d) Bernard et al. (2017) provided the steps of coating buildup of an SPS columnar structure [108]; (e) Xu et al. (2019) showed the droplets motion trajectories on the surface of a substrate [22]; (f) Sokołowski et al. (2017) presented the trajectories of impinging particles during the formation of SPS coatings [279]; (g) a typical quasi-columnar YSZ coating deposited using the PS-PVD method; (h) Liu et al. (2020) calculated atmospheric long laminar plasma spray (ALPS) jet streamlines near a substrate [79]; (i) particle trajectories before reaching the substrate in the ALPS [79]; (j) the tangential velocity of the particles as a function of the impact location inducing the shadowing effect on the surface of the substrate [79] (Reproduced with permission © Elsevier B.V. & IOP Publishing).

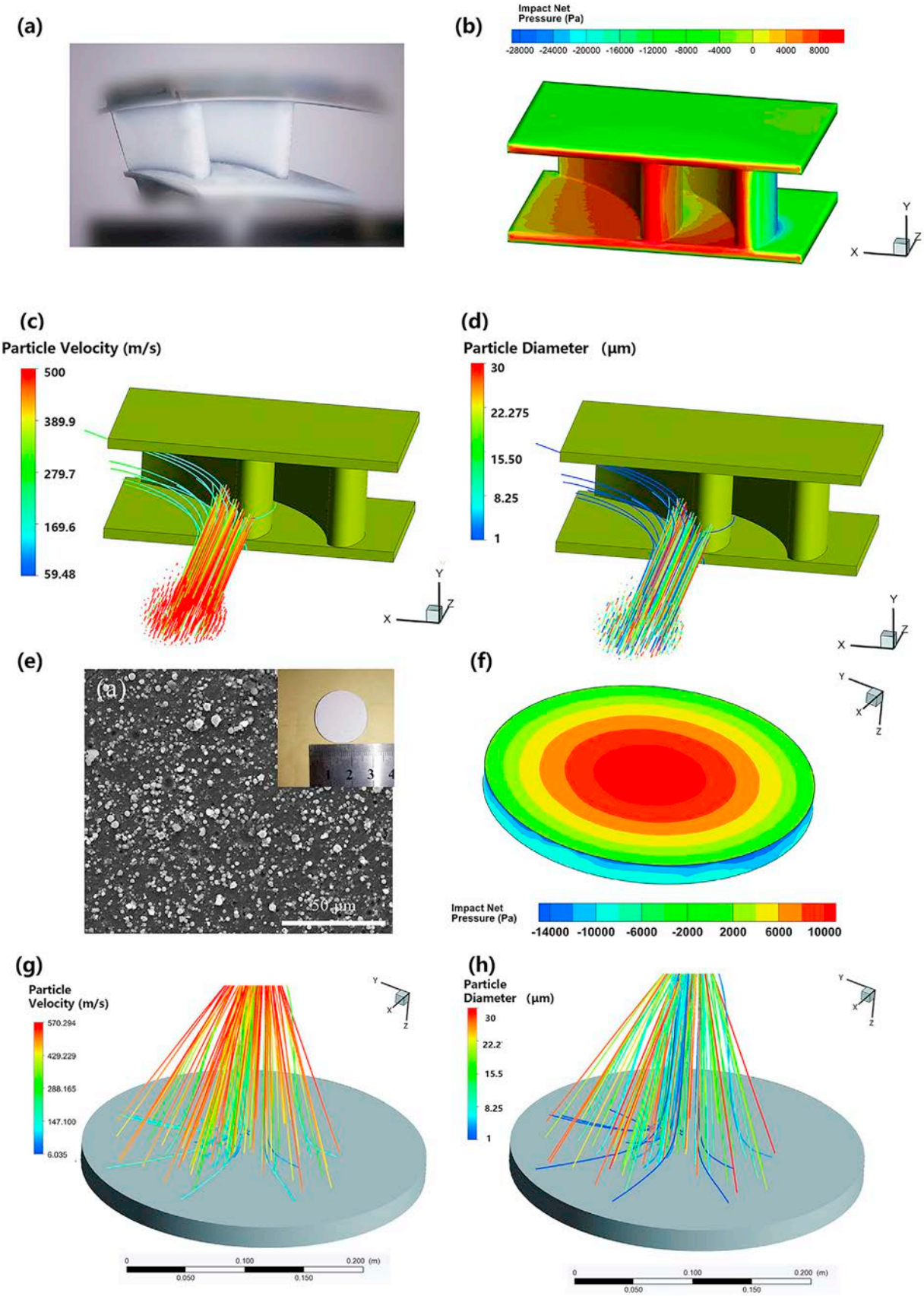

Fig. 20. Non-line of sight deposition of coatings at the spraying distance of 1500 mm induced by the self-shadowing effect of impinging particles (chamber pressure of 200 Pa, 2000 A, 30 SLPM Ar +60 SLPM He): (a) double vane substrate; (b) net impact pressure distributions on the double vane substrate; (c) impinging particle velocity along the tracked particle trajectories; (d) impinging particle diameters along the trajectories; (e) a circular substrate; (f) net impact pressure distributions on the circular substrate; (g) impinging particle velocity along the trajectories; (h) impinging particle diameters along the trajectories.

on the substrate in the PS-PVD processing. As a consequence, the substrate exerts a strong impact on the particle deposition in the velocity and temperature field of the plasma gas flow. The interaction and effects between the plasma gas jet and the particles should be considered including the substrate.

In this section, experiment and numerical studies were carried out to investigate the interaction between plasma gas and particles at the substrate boundary layer and the shockwave region. The heat transfer from the plasma jet to the substrate was studies. The formation mechanism related to the self-shadowing effect of impinging particles, droplet breakup, and atomization during the sudden decrease in pressure from the plasma torch to the plasma jet were clarified.

4.1. Intensification of heat transfer as the low-pressure plasma jet impinges on the substrate

The spraying distance of APS processes usually is in the range of 80–200 mm because the length of these plasma jets that generated by the conventional non-transferred arc plasma torches do not exceed 200 mm in atmospheric environment at a minimum gas flow rate of 30 SLPM [78,260]. Therefore, the atmospheric plasma jet with a huge temperature gradient cannot used to precisely control the substrate temperature during multi-scans of the plasma spraying. In industry, most of atmospheric plasma spraying TBCs do not operate on a very high temperature substrate (e.g., >1000 K), except for some special purposes with auxiliary heating device [[261,262]]. In addition, EB-PVD process usually deposits on the substrate of a high temperature (e.g., >1000 K) by using other auxiliary heating device [263,264], which is one of the essential conditions to obtain columnar structured YSZ coating. However, in spraying distance for deposition of TBCs in PS-PVD usually ranges from 1000 mm to 1500 mm, which is much longer than that of other current plasma spray methods. This section investigates the heat transfer from the plasma jet to the substrate at a chamber pressure of 200 Pa. A typical chamber pressure of 200 Pa and a spraying distance of 1500 mm are chosen according to the experiment.

The heat flux and velocity streamlines around the double vane are shown in Fig. 18-a and 18-b, respectively. The plasma plume impinges directly on the front surface of the substrate and flows through the interspace and edge of the substrate. Oblique views are shown in Fig. 18-c and 18-d, respectively. The maximum temperature and velocity of the plasma gas were above than 1300 K and 450 m/s, respectively, at a spraying distance of 1500 mm. The net impact pressure and enthalpy at the cross-sections of the double-vane substrate are shown in Fig. 18-e and 18-f, respectively. A negative impact pressure area was obtained on the convex surface of the substrate, although a high impact pressure occurred at the interspace of the double vane structure. The maximum enthalpy from the plasma gas to the substrate at a spraying distance of 1500 mm was larger than 1×10^7 J/kg.

The plasma gas temperature and velocity at the vicinity of the double vane substrate are shown in Fig. 18-g and 18-h, respectively. The double-vane structure significantly affects the local flow characteristics of the plasma jet. The plasma gas temperature decreased slightly along the flowing direction and rapidly decreased along the radial direction. The plasma gas velocity suddenly decreased below 200 m/s at the front surface of the substrate, although a high-velocity area was obtained on the convex surface of the two vanes.

The plasma gas temperature and velocity when the plasma plume was impinging on a plane substrate at a spraying distance of 1500 mm are shown in Fig. 18-i and 18-j, respectively. The Inconel 718 alloys substrate was predicted to be heated to 1000 K–1150 K under these conditions, which was in agreement with the measurement shown in Fig. 18-k. The plasma gas velocity rapidly decreased below 200 m/s when the plasma jet reached the top surface of the substrate and the plasma gas streamlines could flow bypass the edge of the plane. Strong entrainment occurred on the bottom surface of the substrate, and it exhibited a negative velocity in the Z-direction. Fig. 18-k shows the measured substrate temperature evolution from 100 s to 1300 s when the low-pressure plasma jet impinges on a substrate obtained by He et al. (2017) [170], which was in agreement with the results of this study.

4.2. Plasma plume induced self-shadowing effect of impinging particles at the boundary layer of the substrate

The EB-PVD method is widely used in the production of columnar-like ceramic coatings. The self-shadowing, or shadowing, of impinging particles is recognized as a vital effect in the repeated scans required to deposit such coatings [52,265–268,272]. The vapor flux at lower incident angles may be blocked by the edge of a columnar grain [269,270]. Inter-columnar gaps and columnar structures are produced by shadowing during the repeated sprays cycles [271,272].

Movchan (2006) indicated that the shadowing zones were in the vicinity of two particles in EB-PVD process (Fig. 19-a) [273], which was caused by micro-protrusions growing on the substrate. The shadowing effect may be enhanced when the incident angle of the vapor flux is below 90°.

Fauchais (2014) and Jordan et al. (2015) indicated that the impinging particles at the boundary layer of the substrate were distributed according to their Stokes number (St) distribution (Fig. 19-c). Impinging particles with a low Stokes number (St < 1) follow the streamlines of the plasma jet and can bypass the edge of the substrate (Fig. 18-b). Impinging particles with a high Stokes number (St > 1) are deposited on the substrate completely in the atmospheric plasma spray process [274,275].

Bernard et al. (2017) described the steps of coating buildup of SPS columnar structures (Fig. 19-d) [108] by considering the impingement angles of large particles, which do not deviate, and strongly-deviated small particles at the boundary layer of the substrate. Sokołowski et al. (2017) presented the trajectories of incoming particles during the formation of SPS coatings (Fig. 19-f) [276], which were dominated by the adhesion force and drag forces of particles within the plasma plume. Xu et al. (2019) analyzed the trajectories of Yb_2O_3 droplets near the substrate in high-velocity low-pressure plasma spray (Fig. 19-e) [22], showing that the deposition locations of impinging particles are affected by their Stokes number.

Liu et al. (2020) calculated the particle trajectories before impacting the substrate in the atmospheric long laminar plasma spray process (ALPS) [79]. They found that the tangential velocity of the particles was crucial in determining the deposition position. This factor induced the shadowing effect of impinging particles at the boundary layer of the substrate in repeated scans (Fig. 19-h–19-j).

We attempted to demonstrate the shadowing effect of impinging particles in the PS-PVD process operating at an input current of 2000 A and a chamber pressure of 200 Pa using 30 SLPM argon and 60 SLPM helium. The results are shown in Fig. 20 using a double vane substrate (Fig. 20-a) and a circular substrate (Fig. 20-e) from an aircraft engine.

The net impact pressure from the low-pressure plasma jet to the double vane substrate at a spraying distance of 1500 mm is shown in Fig. 20-b. The net impact pressure (dynamic pressure) is the difference between the total pressure (stagnation pressure) and static pressure. The maximum net impact pressure was larger than

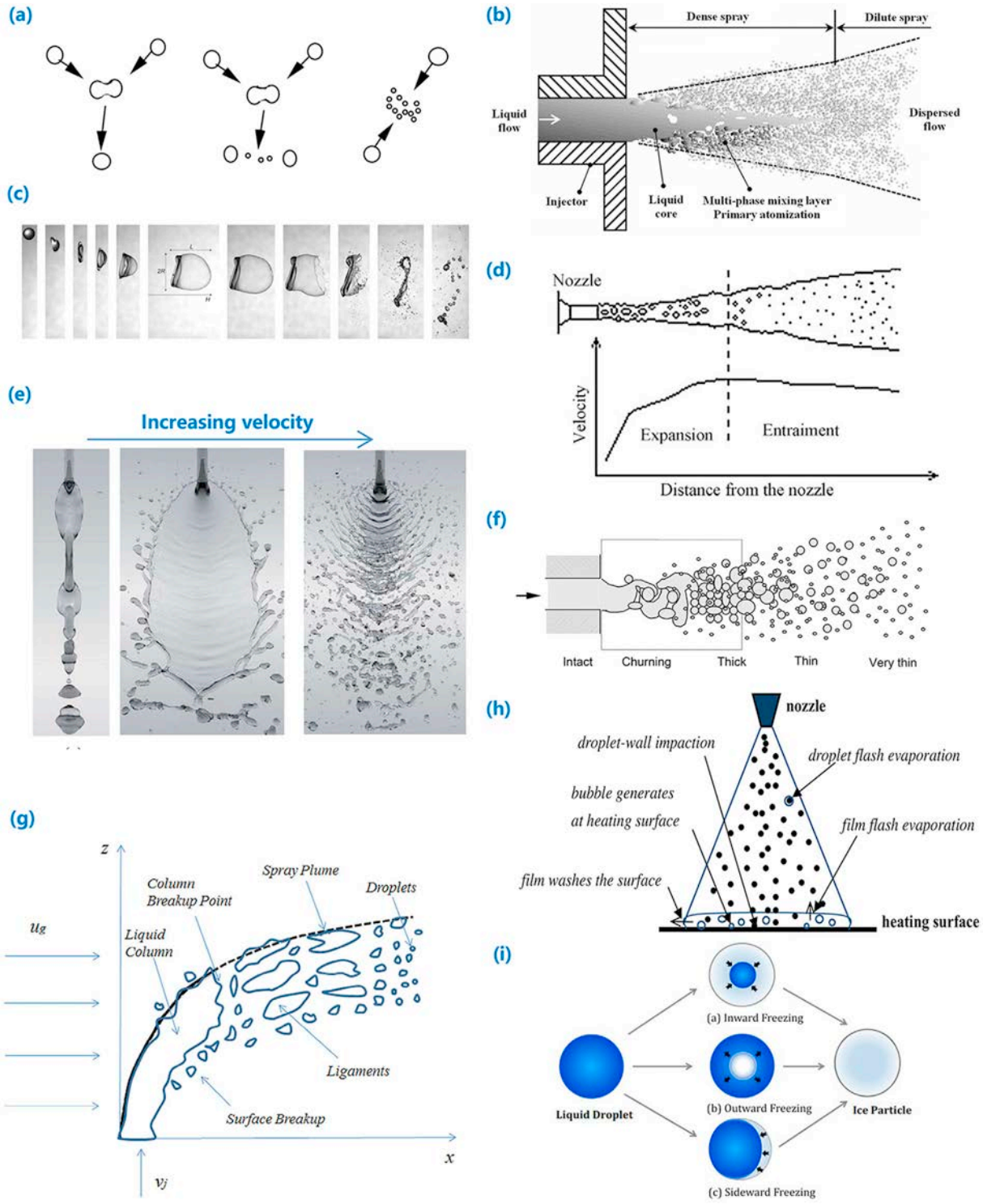

Fig. 21. (a) Schematic representation of outcomes of the coalescence, collision and shattering during droplet breakup as Weber number increases as presented by O'Rourke (1982) [312]; (b) Faeth et al. (1995) illustrated the spray structure in the atomization region [313]; (c) Opfer (2014) investigated the typical evolution of a single bag breakup of water in an airflow [314]; (d) Polanco et al. (2010) described the expansion and entrainment areas as the center velocity in a flashing jet varied [315]; (e) Chen et al. (2013) simulated the impinging jet flow patterns with the increasing of flow velocity [316]; (f) Reitz. (1996) presented a schematic representation of spray regimes for liquid injection from a single hole nozzle [317]; (g) Wang et al. (2016) investigated the liquid column and spray plume regions when a jet penetrates a cross-flow [318]; (h) Cheng et al. (2015) studied the heat transfer mechanism in vacuum flash evaporation cooling [311]; (i) Wang et al. (2017) indicated the possible patterns for droplet freezing (re-solidification) in a vacuum spray [319]. [][][].

8000 Pa on the front surface of the substrate, and a negative impact pressure was formed on the convex surface of the substrate. The impinging YSZ particle velocity and diameter distributions as the trajectories are shown in Fig. 20-c and 20-d, respectively. The small particles (diameter less than 5 μm) can bypass the concave surface of the blade, while the larger particles are deposited.

The net impact pressure on a circular substrate at the same spraying distance is shown in Fig. 20-f. The maximum impact net pressure was higher than the blade substrate shown in Fig. 20-d and also exhibited a negative area of impact net pressure at the edge of a circular substrate. The impinging particle velocity and diameter distributions are shown in Fig. 20-g and 20-h, respectively. The small particles flowed further at a lower velocity and are deposited at a lower incident angle than the larger particles. The previously deposited particles tend to block the subsequently impinging particles in repeated scans of the plasma spray, inducing a self-shadowing effect.

4.3. Shockwave-induced flash vaporization and atomization of YSZ materials in the PS-PVD process

The study of the evaporation and vaporization of droplets is mainly directed toward the better understanding of the PS-PVD method and design of the industrial devices. Therefore, the aim of this section is to improve the fundamental understanding of the droplet heating, boiling and vaporization.

Vaporization and boiling are two thermodynamic processes that govern liquid-to-gas phase change [280]. Vaporization is a phase change phenomenon in which some of the molecules have sufficient kinetic energy to escape from the liquid into the vapor phase when the vapor pressure is lower than the saturation pressure [281,282]. The boiling process is a volume-based phenomenon in which gas bubble formation occurs when the vapor pressure of a liquid is equal to the local pressure [283–285]. During the evaporation, explosive boiling phenomenon occurs inside superheated droplets on a heated surface [286,287]; the boiling temperature is used as a parameter to characterize this phenomenon [288,289].

Jiang et al. (2017) indicated that three typical cases of vaporization exist [290]:

(1) Heating vaporization ($Q_{conv} + Q_{rad} > Q_{vap}$): the droplet temperature increases until it is completely vaporized.
(2) Isothermal vaporization ($Q_{conv} + Q_{rad} = Q_{vap}$): droplet vaporization at a fixed temperature.
(3) Cooling vaporization ($Q_{conv} + Q_{rad} < Q_{vap}$): the droplet temperature decreases below the boiling point of the material, and evaporation occurs on the surface of the liquid [291]. Evaporation is a type of vaporization of a liquid that occurs only on the surface of a liquid [292].

However, before the vaporization of YSZ occurs, the YSZ particles melt into liquid columns or droplets after they are injected into the plasma torch (Figs. 15 and 16). The liquid is abruptly accelerated by the perpendicular plasma gas flow, and the large drops break up into smaller drops [293–295], which is a well-known phenomenon when a liquid jet flows through a nozzle into a low-pressure environment below its saturation pressure [296,301,305]. This process frequently forms an atomized spray owing to the unsteady turbulent flow of liquid droplets [297–299].

The generated droplets further collapse into smaller droplets through the aerodynamic force, called secondary breakup [300], particularly in the shock area of the low-pressure plasma jet. Subsequently, the generated droplets evaporated within 0.1–0.4 s, as described in Section 3.4. Flash vaporization is a vaporization phenomenon caused by a sudden pressure gradient below the saturation pressure [301–303]. Owing to this abrupt decrease in pressure, the liquid undergoes a rapid phase transition and the sensible heat of the liquid converts into latent heat of vaporization [304,305]. The heat transferred to the particle during this process is mostly used to overcome the latent heat of vaporization [306,307]. Flashing can induce a shock wave when the fluid is exposed to an abrupt pressure drop. This generated shockwave can transfer the energy of a high-pressure fluid directly to another low-pressure fluid [308,309]. Under this condition, when the heat is conducted through the liquid at a sufficiently high rate, surface vaporization occurs.

The mass vaporization rate can be calculated using [310],

$$\frac{dm}{dt} = D\left(\rho_l - \rho_s\right) \tag{42}$$

where D is the mass transfer coefficient (mm^2/s), ρ_l is the saturated vapor density of the liquid film, and ρ_s is the saturated vapor density of the environment. The driving force of mass transfer is the vapor density difference on both sides of the vapor–liquid interface [311]. The vapor density above the vapor–liquid interface is the saturated vapor density at the surrounding temperature. The vaporization rate in the jet area increases as the final pressure decreases and the initial temperature increases [303], which is a critical criterion of the PS-PVD process (50–200 Pa) and the LPPS process (1000–10000 Pa).

As Fig. 21 shows the models of the coalescence, collision and shattering during droplet breakup. Rourke (1982) investigated the binary collision of in-flight droplet that could overcome coalescence, collision, and shattering during the breakup process (Fig. 21-a) [312]; Faeth et al. (1995) illustrated the spray structure near the nozzle in the atomization breakup region (Fig. 21-b) [313], which contained the dense spray region, multiphase mixing region, dilute spray region, and dispersed flow regions. The primary breakup occurred owing to the formation of ligaments and other irregular liquid elements along the surface of the liquid core. The dense spray region is strongly dependent on the liquid flow characteristics, e.g., the turbulent intensity and vorticity properties at the jet nozzle. Similarly, Reitz (1996) presented a schematic representation of spray regimes for liquid injection from a single hole nozzle (Fig. 21-f) [317]. The in-flight droplets pass through the churning region, thick region, thin region and very thin region.

Recently, Opfer (2014) investigated the typical evolution of a single bag breakup of water in an airflow through continuous images in the experiment (Fig. 21-c) [314]. This prediction of film thickness based on film kinematics was validated for the initial stage through direct measurements of drop thickness. Polanco et al. (2010) described the expansion and entrainment areas as the centre velocity in a flashing jet varied (Fig. 21-d) [315]. The expansion region is characterized by the continuous breakup and evaporation of large droplets or liquid ligaments occurs, and the entrainment region by a decrease in the droplet velocity. Chen et al. (2013) simulated the impinging jet flow patterns with an increase in the flow velocity (Fig. 21-e) [316]. The flow patterns of the glycerin-water solution change from the liquid chain, closed rim, and unstable rim to an impact wave as the flow velocity increases.

Wang et al. (2016) evaluated the liquid column and spray plume regions when a jet penetrated a subsonic crossflow (Fig. 21-g) [318]. The spray trajectory was unsteady or oscillatory in a high-temperature subsonic crossflow [320]. Surface breakup dominated the liquid jet column and fragments evaluation owing to the hydrodynamic instabilities, which resulted in smaller droplets and spray formation. Cheng et al. (2015) studied the heat transfer mechanism of vacuum flash evaporation cooling (Fig. 21-h) [311], which included droplet wall impaction heat transfer, film flash evaporation heat transfer, film surface convective heat transfer, heat transfer induced by boiling bubbles and environment heat transfer. Wang et al. (2017) indicated that three possible patterns of droplet freezing (re-solidification) exist in a vacuum spray after droplet flash evaporation (Fig. 21-h) [319].

The study of droplet breakup is frequently described using three

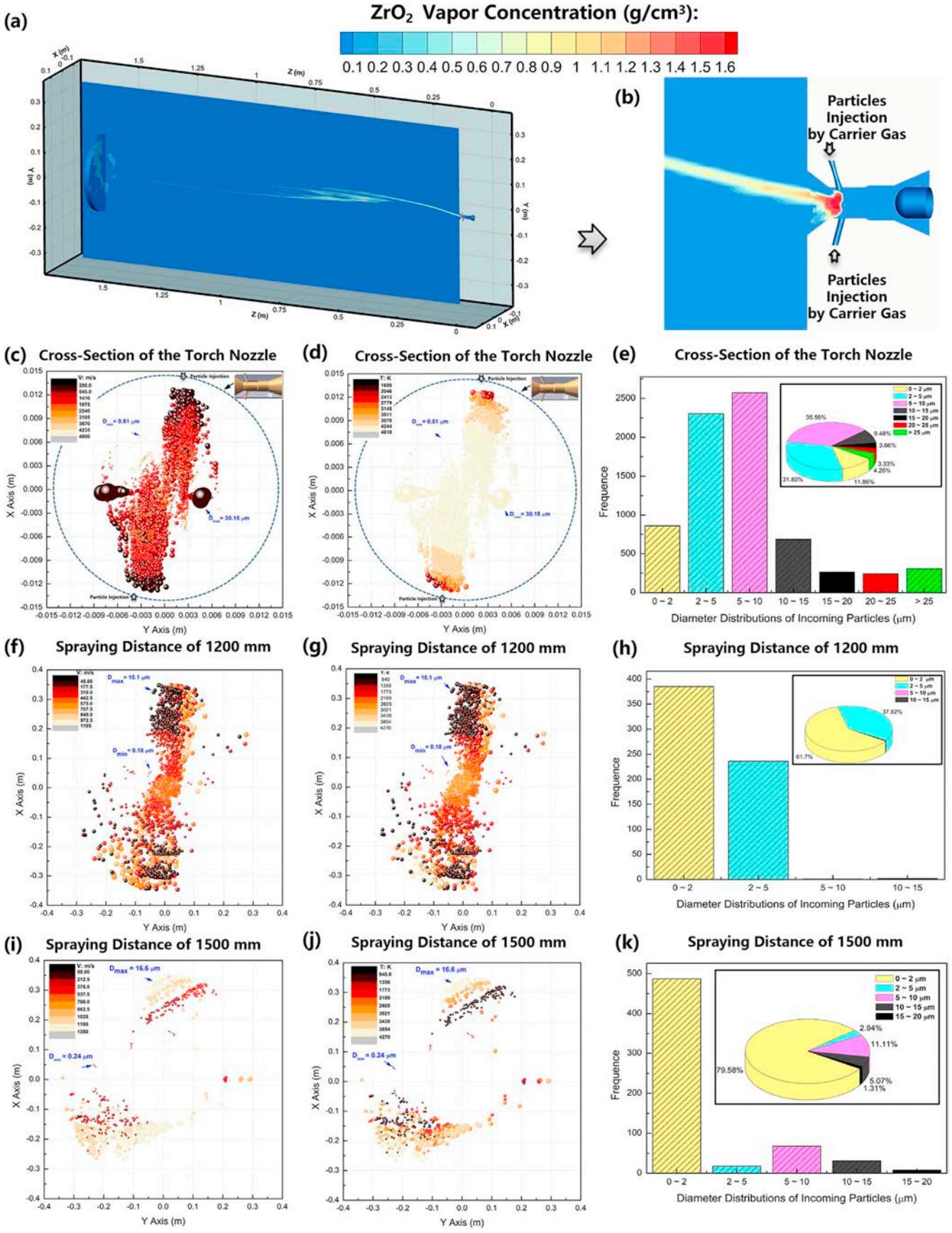

Fig. 22. Zirconia vapor concentration distribution in the three-dimensional domain with a substrate (chamber pressure of 100 Pa, 2000 A, 30 Ar +60 He, SD = 1500 mm, 2 × 4 g/min) in this work (a); magnification view of the zirconia vapor concentration nearby the torch nozzle (b); particles velocity (c) and temperature (d) as the tracked particle diameter

dimensionless parameters [321]. The aerodynamic Weber number affects the primary breakup behavior and the vortex development and morphology behind the liquid column, which results in a drastic change in the evaporation process [300].

$$We = \frac{\rho u^2 d}{\sigma} \tag{43}$$

The Weber number is the ratio of inertial to surface tension forces, where ρ and σ are the density and surface tension of the liquid, respectively. Moreover, the Weber number represents the relative strength of the bubble surface tension force against the liquid momentum owing to bubble expansion [322].

The Ohnesorge number (Oh) is used to characterize the strength of the viscous dissipation of the liquid relative to the product of liquid inertia and surface tension.

$$Oh = \frac{\mu}{\sqrt{\rho d \sigma}} \tag{44}$$

The liquid becomes superheated by exposure to the environment at a pressure lower than the liquid's saturation pressure [323]. The entire process can be characterized by the Jakob number (Ja), which quantifies the ratio between the available heat stored in the liquid and the latent heat required for vaporization. Ja is an important dimensionless parameter that can characterize flash vaporization [18].

$$Ja = \frac{\rho_l C_l \Delta T_{sub}}{\rho_g h_{fg}} \tag{45}$$

Jakob number (Ja) represents the ratio between the sensible heat and latent heat in the process of phase change.

Accordingly, many analytic predictive models for drop deformation and breakup have been developed using the above non-dimensional parameter models. The most widely used models in computational fluid dynamics coupled with momentum conservation equations are the Taylor breakup model (TAB), and the Kelvin-Helmholtz and Rayleigh-Taylor (KHRT) hybrid and wave models. We used the three models to investigate the breakup and vaporization of YSZ droplets in this work, as discussed in Section 3.1.

However, the wave model is appropriate for high-speed injections, where the Kelvin-Helmholtz instability is considered to dominate droplet breakup [324], which considers the breakup of the droplets to be induced by the relative velocity between the gas and liquid phases. The model assumes that the breakup time and the resulting droplet size are related to the fastest-growing Kelvin-Helmholtz instability due to the plasma jet stability. The wavelength and growth rate of this instability are used to predict details of the newly formed droplets, as described in Section 3.1.

Fig. 22-a shows the zirconia vapor concentration distribution during the PS-PVD (chamber pressure = 100 Pa, I = 2000 A, 30 SLPM Ar + 60 SLPM He) in this study at a total feed rate of 8 g/min with two-way injection. The maximum vapor concentration was approximately 1.6 g/cm^3 under this condition. Fig. 22-b shows the magnification view nearby the torch nozzle in Fig. 22-a, where the highest vapor concentration occurred inside the plasma torch and the zirconia vapor was pushed further to a spraying distance of 1000 mm. Flash vaporization occurred immediately inside the plasma torch where the YSZ particles were initially injected. This was also observed for the steady model in Fig. 15.

Fig. 22-c and 22-d show the calculated in-flight particle velocity and temperature distributions as the particle diameters at the cross-section of the torch nozzle varied, respectively. The particles at the edge of the torch wall had a low in-flight velocity, and the particles were gradually accelerated when they flowed further into the plasma jet. A large area of particle temperatures was above 4500 K (the boiling point of zirconia is 4548 K), and these may be quickly vaporized at temperature equal to or above to the boiling point of zirconia through the heating vaporization model or isothermal vaporization model as mentioned before. The statistical distribution of particle diameters at the cross-section of the torch nozzle is shown in Fig. 22-e by considering the breakup of droplets in the wave model, where it comprised multi-sized in-flight particles. 11.86% of in-flight particles had diameters ranging from 0.81 to 2 μm; 31.85% of in-flight particles had diameters in the range of 2–5 μm, and 35.56% of in-flight particles had diameters range of 5–10 μm. The remaining 20.73% in-flight particles were in the range of 10–30.15 μm.

The in-flight particle velocity and temperature distributions as the particle diameters varied at the cross-section of the spraying distance of 1200 mm are shown in Fig. 22-f and 22-g, respectively. The distribution of in-flight particle locations at the cross-section occurred in a larger range. The in-flight particle velocity was lower than the result of the cross-section of the torch nozzle. The high area of particle temperature occurred in the center area, and part of the particle temperature was still above 4200 K. After flowing a distance of 1200 mm, the statistical distribution of particle diameters ranged from 0.18 μm to 10.1 μm, which primarily comprised particles with diameters of 0.18–2 μm at a percent of 61.7% and in the diameter of 2 μm–5 μm at a percentage of 37.82%.

The in-flight particle velocity and temperature distributions as particle diameters varied at the cross-section of the spraying distance of 1500 mm are shown in Fig. 22-i and 22-j, which is also the top surface of the substrate. According to Section 4.1, the impinging particles will flow bypass the edge of the substrate owing to the shadow effect. Therefore, the center area at the cross-section had a high zirconia vapor concentration (Fig. 22-a); other impinging particles were distributed at the periphery of the substrate, which was also in agreement with observations. In the experiment, the YSZ coating microstructure featured a smooth quasi-columnar structure or a cauliflower-like structure at the center of the substrate [14,20]. However, the coatings had a mass of splashed nanoparticles at the periphery of the substrate that exhibited unclear interspaces within the cauliflower-like structures on the top surface [88,89]. The diameters of in-flight particles ranged from 0.24 to 2 μm at a percentage of 79.58%, 2–5 μm at a percentage of 2.94%, 5–10 μm at a percentage of 11.11%, and 10–15 μm at a percentage of 5.07%.

Therefore, a high zirconia vapor concentration existed inside the plasma torch area owing to flash vaporization when the temperature is equal to or above its boiling point, as the heating vaporization model or isothermal vaporization model. Thereafter, the liquid columns are atomized in the low-pressure chamber near the torch nozzle and further breakup into smaller particles, which significantly increases the total specific surface area of the liquid. The evaporation may occur on the surface of a liquid when the temperature is above the boiling point of zirconia. Meanwhile, several liquids can freeze to a solid or half-solid state during a long spraying distance when the particle temperature is cooled to below

distributions at the cross-section of the plasma torch; the statistical distribution of particle diameters at the cross-section of the plasma torch (e); particles velocity (f) and temperature (g) as the tracked particle diameter distributions at the spraying distance of 1200 mm; the statistical distribution of particle diameters at the spraying distance of 1200 mm (h); particles velocity (i) and temperature (j) as the tracked particle diameter distributions at the spraying distance of 1500 mm; the statistical distribution of particle diameters at the spraying distance of 1500 mm (k).

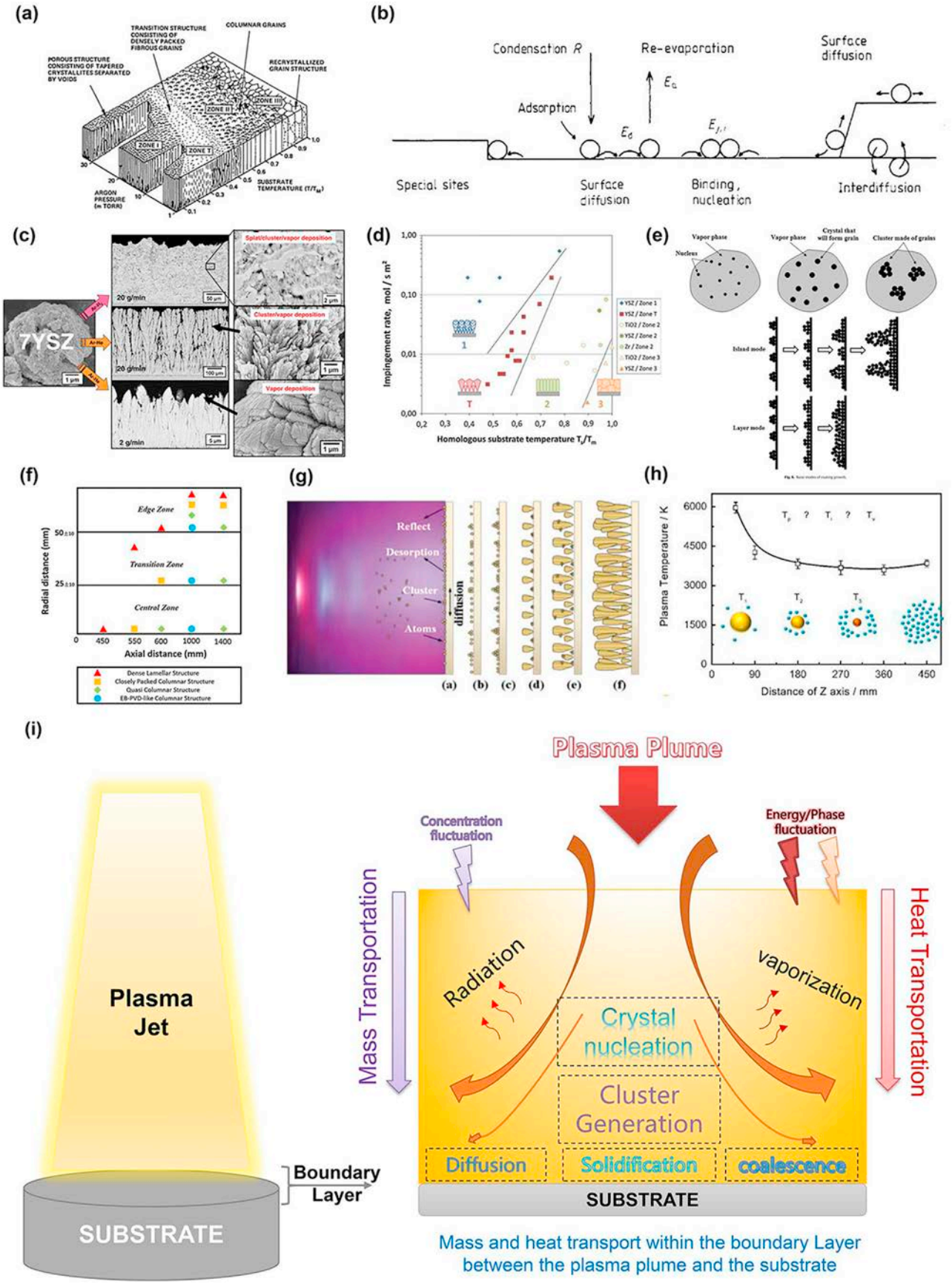

Fig. 23. Formation mechanism of thin films and coatings deposited from vapor: (a) Effect of geometry and deposition conditions on the structure of thick sputtered coatings by Thornton (1974) [344]; (b) rate equation approaches to thin film nucleation kinetics by Venables (1984) [330]; (c) and (d) are the effects of impingement rate on the microstructure

2950 K (melting point of zirconia). That is frequently called the re-solidification of the droplet and is commonly observed in atmospheric plasma spray processes at certain spray distances [234,325–328].

The deposition units at a spraying distance of 1500 mm in the PS-PVD process are as follows:

1) secondary breakup droplets;
2) re-solidification particles;
3) particles from vapor condensation.

However, the vapor phase can be transferred to either the liquid phase or solid phase depending on the local conditions at the boundary layer of the substrate, which will be discussed in the next section.

5. Kinetic surface diffusion, migration, coalescence, and decay of nano-clusters in the additive manufacturing of the coatings

According to the previous discuss, the coating growth was under a high temperature on the substrate surface during the additive manufacturing of the PS-PVD method. A mixture depositing unites was observed and studies in the previous sections. However, the columns develop a tapered shape so that the growth becomes competitive and local areas grow at a higher rate in the vertical direction comparing with the growth in the parallel direction, as well as the inter-spaces between the columns further develop unclear and vague as the increasing of coating thickness, which will discuss in this section.

5.1. Layer growth versus hybrid growth

Coating surface topographies and fracture microstructure evaluations are often described according to the results of Thornton (1974) [329]. With an increase in the argon pressure from 100 to 3000 Pa and substrate temperature (Fig. 23-a), the formation of a microstructure of sputtered metallic coatings was demonstrated from layers of porous, densely packed, quasi-columnar, and columnar structures. Venables (1984) used the rate equation approach to calculate the thin film formation [330], including the condensation, adsorption, surface diffusion and re-evaporation processes (Fig. 23-b). Fig. 26-c shows the microstructure evolution with increasing YSZ powder feed rate in the PS-PVD process. More splats were obtained in the coating at a high powder feed rate of 20 g/min [331]. The effects of the impingement rate on the microstructural formation of the YSZ coating in the PS-PVD process from the investigations of Vaßen et al. (2013) are shown in Fig. 26-d.

Guo et al. (2014) investigated the microstructural evolution of PS-PVD coatings at different spray distances and classified coatings as dense lamellar, closely packed columnar, quasi columnar structures, and EB-PVD-like columnar structures (Fig. 23-f) [14]. Such a classification has become a scientific consensus in the research on PS-PVD. In addition, they highlighted that the growth of quasi-columnar coatings should consider the absorption of atoms, nucleation, stable islands, early columnar growth and complete growth (Fig. 23-g) [332]. With the continuous arrival of gas atoms, nuclei grow and form a three-dimensional island. The island structure may develop into a column crystal with continuous absorption of vapor atoms. The droplets can fill the gaps in the columns and form pores and defects.

Zhou et al. (2016) investigated the deposition mechanism in the PS-PVD process (Fig. 23-e) [333]. They observed that homogeneous nucleation occurred at the end of the plasma plume, which resulted in the formation of agglomerated clusters. An island structure occurred at a lower average coverage. When the substrate temperature decreased from 850 °C to room temperature, the island growth mode tended to the layer growth mode as the absorbed atoms exhibit a low diffusion ability. Growing a stable nucleus on the substrate was difficult because vapor condensed rapidly and few oriented fine grains were formed because of a large amount of undercooling.

Moreover, Liu et al. (2018) indicated that a two-way compensation mechanism exists between the plasma gas and in-flight liquids in the PS-PVD process (Fig. 23-h) [334,335], which means that evaporation (cooling vaporization) can occur when the droplet temperature is below the boiling point of zirconia, as mentioned in Section 4.3. A large temperature and pressure gradient exist near the substrate surface owing to the different temperatures of the substrate and plasma jet. The partial and vapor pressures of the vapor atoms determine the supersaturated boundary layer where clusters can be formed. More clusters will form over a larger area of the supersaturated boundary layer [238,336].

Therefore, a high substrate temperature, or interface temperature (usually above than 800 °C), a low chamber pressure (50–200 Pa), and a high input power plasma torch (>100 kW) were the three essentially conditions to obtain an advanced quasi-columnar ceramic coating in the PS-PVD process (Fig. 23-i). The ceramic powders (i.e., YSZ, GZO, and LCO) were injected into the plasma torch; mass intensification and heat transfer occurred on the substrate at a maximum distance of 1000–1500 mm through a low-pressure plasma jet, which had a maximum velocity of over 6000 m/s and a maximum temperature of over 12000 K at the torch nozzle.

In general, the region at which the flow adjusts from zero velocity at the wall to a maximum in the main stream of the flow is termed the boundary layer [337]. The concept of boundary layers is significantly in all viscous fluid dynamics and the theory of heat transfer [338,340]. As a velocity boundary layer develops when there is a fluid flow over a surface (e.g., a flat substrate) [338], a thermal boundary layer develops if the fluid and surface temperatures differ [339], and a turbulent boundary layer will rapidly increase as a result of increased shear stress at the surface [340].

Similarly, the momentum flow is driven by a velocity gradient, the heat flow by a temperature gradient and mass transport on the substrate by a concentration gradient [341]. A mass-transfer (concentration) boundary layer can be defined for ceramic mass transfer on the substrate in the PS-PVD process, for which a large difference between local concentration and concentration from the free stream occurs. For example, a dense lamellar-layer-structured YSZ coating can be deposited at a spraying distance of 550 mm (Fig. 4), although the microstructure will favor a transfer to island growth or hybrid growth at a longer spraying distance under the same operating conditions. As the stand-off distance increases, the supersaturated boundary layer becomes larger and the formation of clusters is easier [88]. In the boundary layer, sufficiently low temperature and high supersaturation are beneficial to the onset of particle nucleation and growth [383]. Thus, the level of supersaturation is more likely to be sufficient, and nucleation and formation

formation of YSZ coating in PS-PVD by Vaßen et al. (2013) [345]; (e) nucleation and cluster coalescence in PS-PVD manufacture of YSZ coating the by Zhang et al. (2016) [333]; (f) microstructural evaluation of PS-PVD coatings at different spray distances by Guo et al. (2014) [14]; (g) schematic diagram of additive manufacturing of coatings in the PS-PVD process by Guo et al.(2016) [332]; (h) two-way compensation mechanism between the plasma gas and liquid in PS-PVD by Liu (2018) [335]; (i) the intensified mass and heat transport at the boundary layer between the low-pressure plasma plume and the substrate in the study.

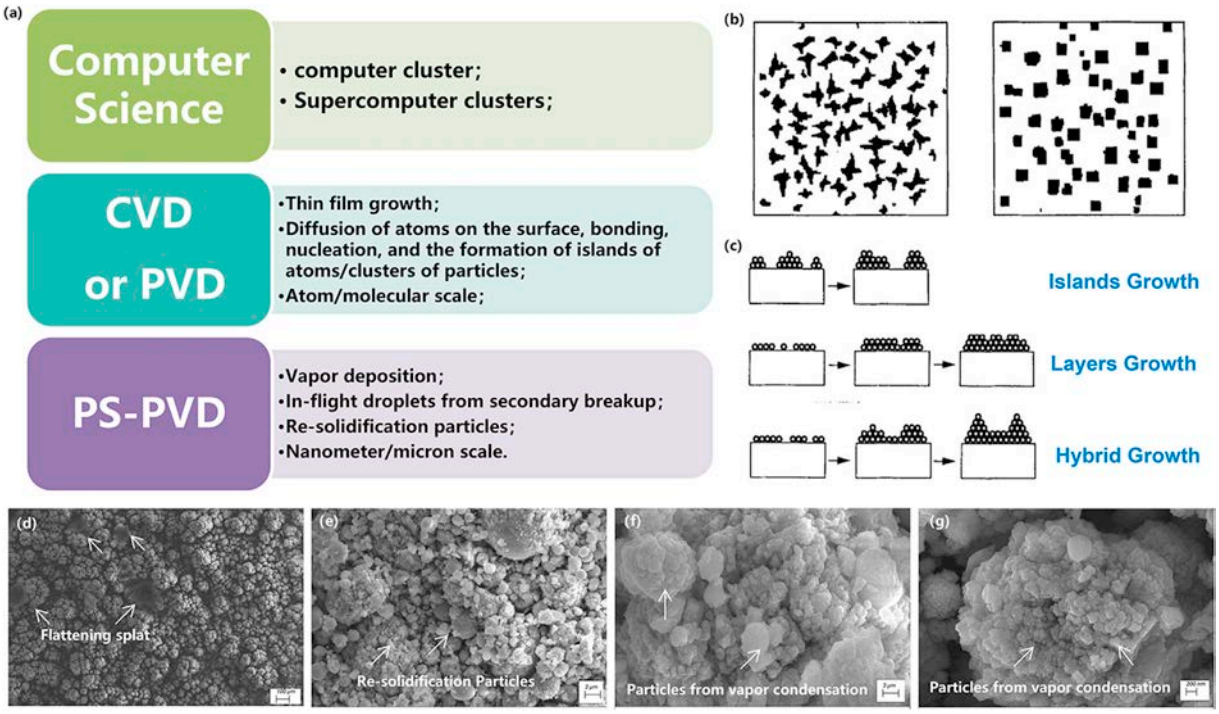

Fig. 24. (a) "cluster" definitions in computer science, CVD and PS-PVD field; (b) modelling of cluster density distributions that caused by diffusion limited aggregation in thin film deposition [348]; (c) schematic illustration of three growth models in the deposition of a thin film by E. Wang (2003) [349]; top surface observation of different nano-sized cluster and cauliflower-like features of YSZ coatings in this study (d), (e), (f), (g).

of small particles are more likely to occur, at longer spray distances in the boundary layer [342]. The large temperature difference in the boundary layer will cause rapid cooling of the deposits to a supercooled state. Hence, homogeneous nucleation from supersaturated vapor is possible at a high supersaturation ratio, and rapid nucleation on the substrate is expected at the beginning [343]. Therefore, the local conditions at the boundary layer of the substrate in the PS-PVD process have a crucial function in dominating the layer growth or hybrid growth model.

In addition, the self-shadowing effect of impinging particles will occur first at the velocity boundary layer before they impact the substrate, as discussed in Section 4. 1.

5.2. Formation of stable clusters during the deposition of ceramic coatings

The formation of a stable cluster of island features is an initial step during the growth of a coating on the substrate. Particle formation in a plasma plume involves the growth of molecular or ionic clusters. This growth can occur by physical condensation of a supersaturated vapor, e.g., metal or ceramic vapors by a sequence of chemical reactions, direct vapor deposition on nano-particle surfaces or coagulation due to collisions between nano-particles [346]. However, "cluster" is also a common word in the computer science field (Fig. 24-a). A cluster in Chemical Vapor Deposition (CVD) or Physical Vapor Deposition (PVD) fields refers to a group of adatoms at the atomic or molecular scale. A group of clusters form an island feature on the top surface of the coating or thin film [347]. Witten and Sander (1981) proposed a diffusion-limited aggregation mechanism in the deposition of thin films, and the formation of a compact island and fractal island from a mass of clusters [348]. Wang (2003) modeled the formation and density of clusters based on the diffusion-limited aggregation mechanism (Fig. 24-b). The growth of a thin film can be achieved through three different models under different local conditions [349]: the layer growth model (Frank-van der Merwe model), island growth model (Volmer-Weber model) and hybrid growth model (Stranski-Krastanov model) (Fig. 24-c).

Similarly, in the PS-PVD process, hybrid deposition units (vapor condensation, nano-droplets from the secondary breakup, and re-solidification particles) exist at spraying distances ranging from 1000 to 1500 mm. The different microstructures of nano-sized clusters and cauliflower-like YSZ coatings on the top surface are shown in Fig. 24-d–24-g. The flattening splat originated from the impinging droplets. Re-solidification particles exhibited a fractal island feature, and the particles from vapor condensation exhibited a compact island feature.

In the experiment (Fig. 25), the spraying time was increased from 1 to 40 s under two different operating conditions. The deposition units were constant in multiple scans of the plasma spray at a given powder feed rate. Many nano-clusters were formed on the substrate at the initial step and distributed randomly. Subsequently, apparent island structures were obtained with a thickness of 2–5 μm, comprising smaller islands and connected with nanoclusters or droplets. Finally, a hybrid deposition coating was obtained with a thickness of over 50 μm.

Accordingly, Gao et al. (2016) proposed that the quasi-columnar YSZ coating was composed of droplets, unmelted particles, and vapor from original feed-stock powders in the PS-PVD process (Fig. 26-a) [332]. Zhang et al. (2017) separated the deposition in the PS-PVD process into the initial, growth and complete stages, for a processing using a solid nucleus surrounded by a liquid layer, droplets, nanoparticles, micron-sized particles, and vapor phases (Fig. 26-b) [87]. Chen et al. (2019) observed the deposition mechanisms between VLPPS coatings and PS-PVD coatings (Fig. 26-c) [350]. A higher particle temperature and velocity were achieved because of the lower chamber pressure and higher input power of the PS-PVD process. In addition, Racek (2010) reported that the

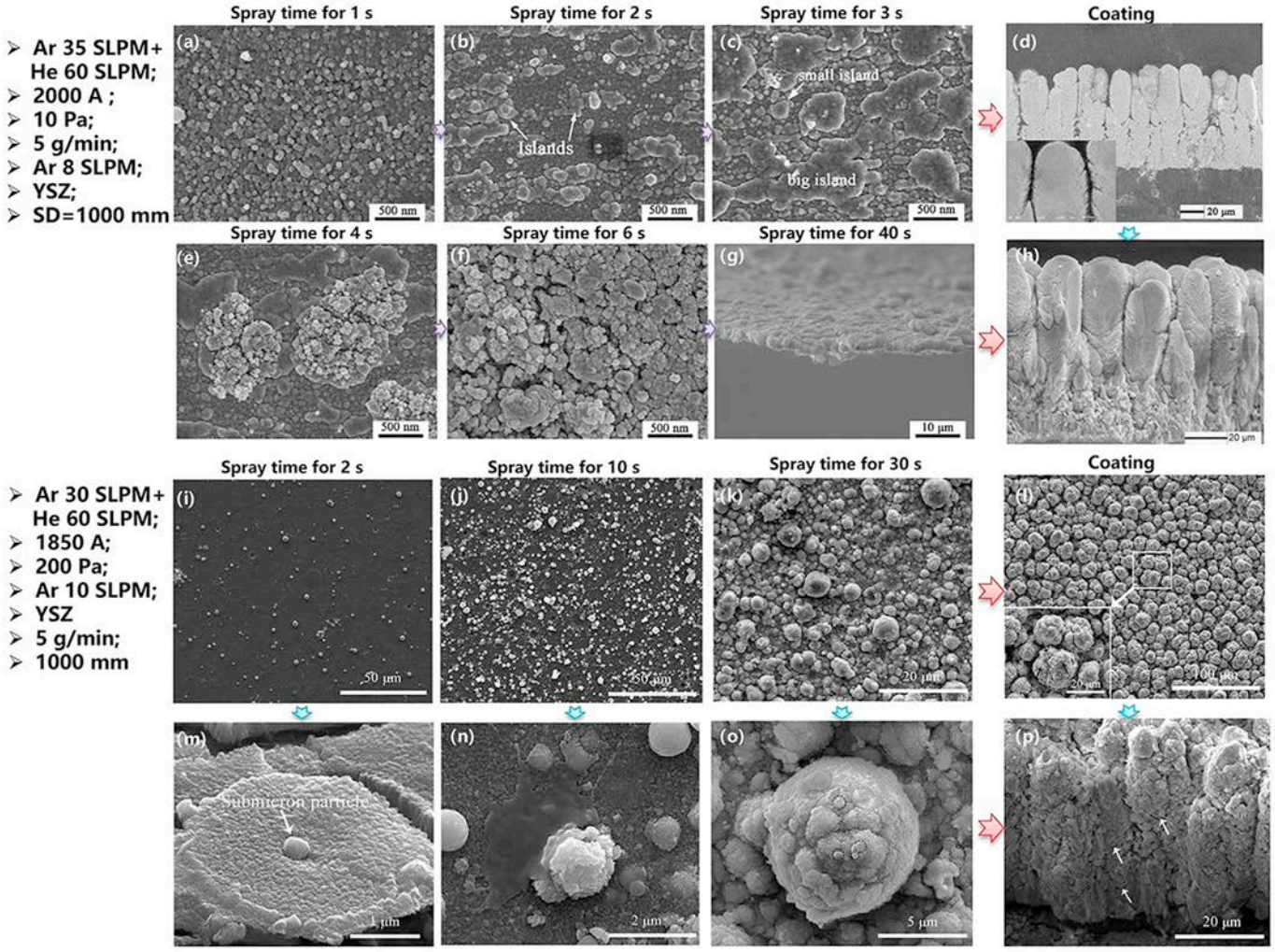

Fig. 25. Additive manufacturing process of quasi-columnar coatings during low-pressure plasma spray-physical vapor deposition: top surface after deposition (P = 10 Pa, I = 2000 A, 35 SLPM Ar + 60 SLPM He, SD = 1000 mm) (a) spray time of 1 s; (b) spray time of 2 s; (c) spray time of 3 s; (d) the YSZ coating with a thickness of 45 μm; (e) spray time of 4 s; (f) spray time of 6 s; (g) spray time of 40 s; (h) coating with a thickness of 45 μm. Top surface observation after deposition (P = 200 Pa, I = 1850 A, 30 SLPM Ar + 60 SLPM He, SD = 1000 mm): spray time of 2 s in (i) and (m); spray time of 10 s in (j) and (n); spray time of 30 s in (k) and (o); top surface observation of the YSZ coating (l); fracture surface observation of the coating (p) (Reproduced with permission [87,332]© Elsevier B.V.).

formation of island protrusions on the surface of the coating may relate to the splashing from high-speed impinging droplets (Fig. 26-d) [351].

For droplet solidification on a flat surface, according to the studies by Masdejski (1975) [352], Vardelle. et al. (1995) [353], and Rangel et al. (1997) [354], the deformation and solidification process of a single droplet in plasma spraying technology is described by the conservation of mechanical energy:

$$\frac{d}{dt_s}\left(E_k + E_p + E_d\right) = 0 \tag{46}$$

for which the kinetic energy is calculated using,

$$E_k(\mathrm{t_s}) = \frac{3}{10}\pi\rho_p\left(\frac{dR}{dt_s}\right)^2\left(\mathrm{R^2 b} + \frac{11}{7}\mathrm{b^3}\right) \tag{47}$$

The potential energy on the free surface of the substrate is calculated using,

$$E_p = \sigma\left(\pi \mathrm{R^2} + 2\pi R\mathrm{b}\right) \tag{48}$$

The viscosity energy dissipation rate of liquid droplets is calculated using,

$$\frac{dE_d}{dt_s} = \frac{\pi\mu R^2}{b}\left(\frac{dR}{dt_s}\right)^2\left(\frac{3}{2} + \frac{72}{5}\frac{b^2}{R^2}\right) \tag{49}$$

where b and R in Eq. (47)–(49) are the geometrical parameters of a molten layer during dynamic flattening and solidification, and σ is the surface tension of the liquid droplet. The kinetic energy and viscosity energy dissipation when the liquid droplets impinge on a solid surface are all time-dependent quantities.

The theoretical studies of nucleation and growth of clusters were computed based on an adatom concentration distribution that was obtained by solving an adatom diffusion equation on the substrate in a sequence of time stages [355–358].

$$\frac{\partial n(r,t)}{\partial t} = \frac{\nu}{4}\nabla^2\ \mathrm{n(r,t)} + \mathrm{F} \tag{50}$$

At the initial stage, the adatom concentration gradually increases when the deposition rate of adatoms is equal to the vapor impingement rate *(F)* [359]. Moreover, the vaporized atoms cannot

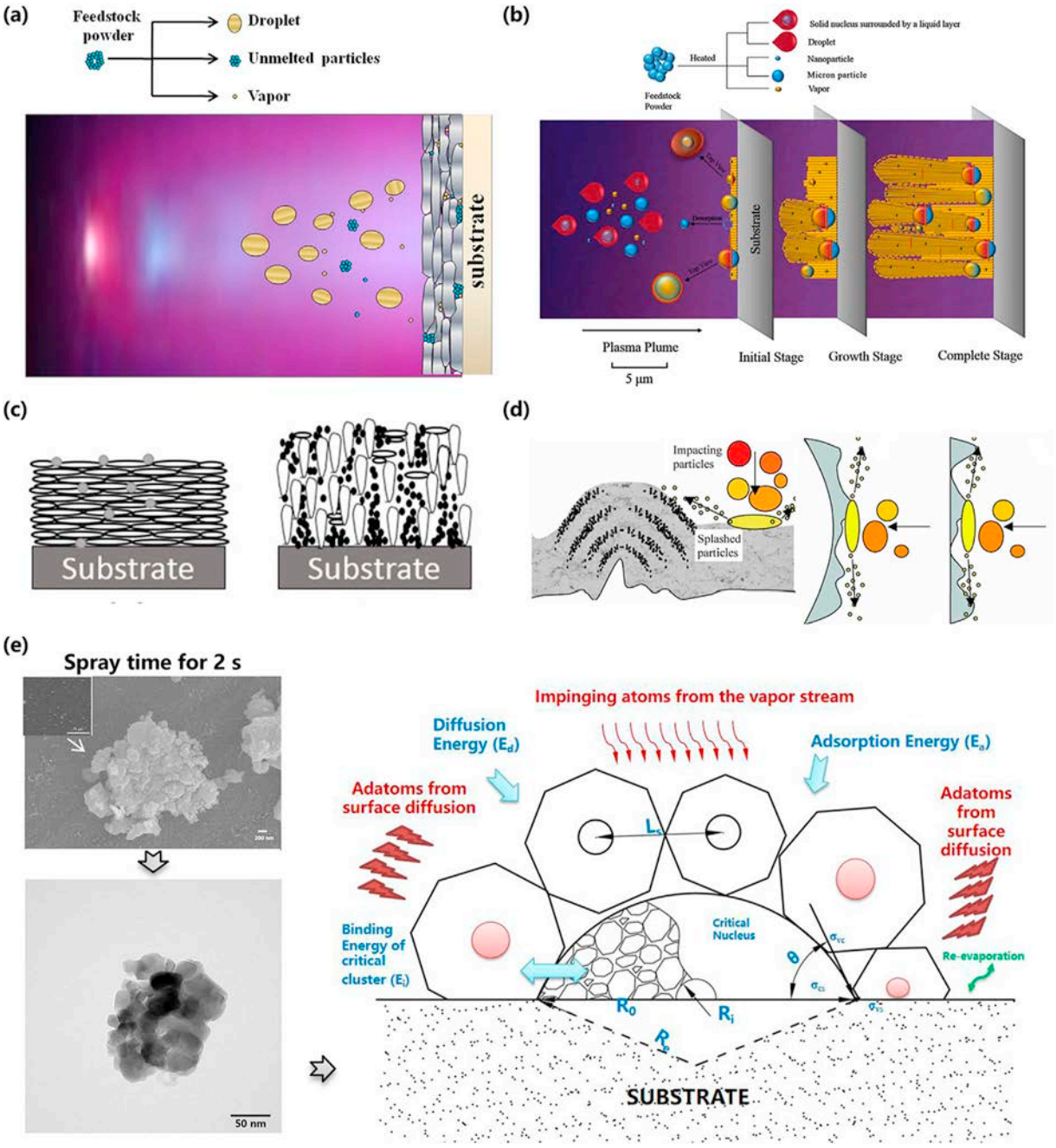

Fig. 26. (a) Gao et al. (2016) proposed the deposition mechanism of the dense coating in PS-PVD [332]; (b) Zhang et al. (2017) gave the deposition model of quasi-columnar coating in PS-PVD [87]; (c) Song Chen et al. (2019) observed the deposition mechanisms of VLPPS and PS-PVD coatings [365]; (d) Racek (2010) proposed the formation of island protrusions of the coating in HVOF [366]; (e) schematic illustration of the cluster formation on the substrate according to the experimental observation and effects of adsorption energy (E_a), diffusion energy (E_d), and binding energy (E_i) on the critical cluster that contained adatoms from surface diffusion and vapor stream.

always condense when they impinge on a surface. The adatoms may diffuse on the surface for a period of time (resident time/relaxation time) and then re-evaporate back to the vapor phase [360]. Meanwhile, they may collide with other adatoms during its migration, causing nucleation on the surface of the substrate. The adatom concentration is determined by the vapor rate, re-evaporation, and capture rates of the existing clusters. A stable cluster on the substrate may grow by the capture of adatoms via surface diffusion and by the direct addition of atoms from the vapor stream during the plasma spray [361]. The effects of adsorption energy (E_a), diffusion energy (E_d), and binding energy (E_i) on the formation of a critical cluster based on the experiment results are shown in Fig. 25-e. The separation of clusters is *Ls* and each cluster of effective radius R_i occupies an effective zone of effective radius R_o.

The adsorption energy (E_a) is determined by the residence time (τ_s) and atom vibration frequency (ν) [362,363],

$$E_a = k \cdot T_{sub} \cdot \ln(\nu \tau_s) \tag{51}$$

The activation energy of surface diffusion (E_d) is calculated through the surface diffusion (D) and adatom jump distance (a) as follows [363]:

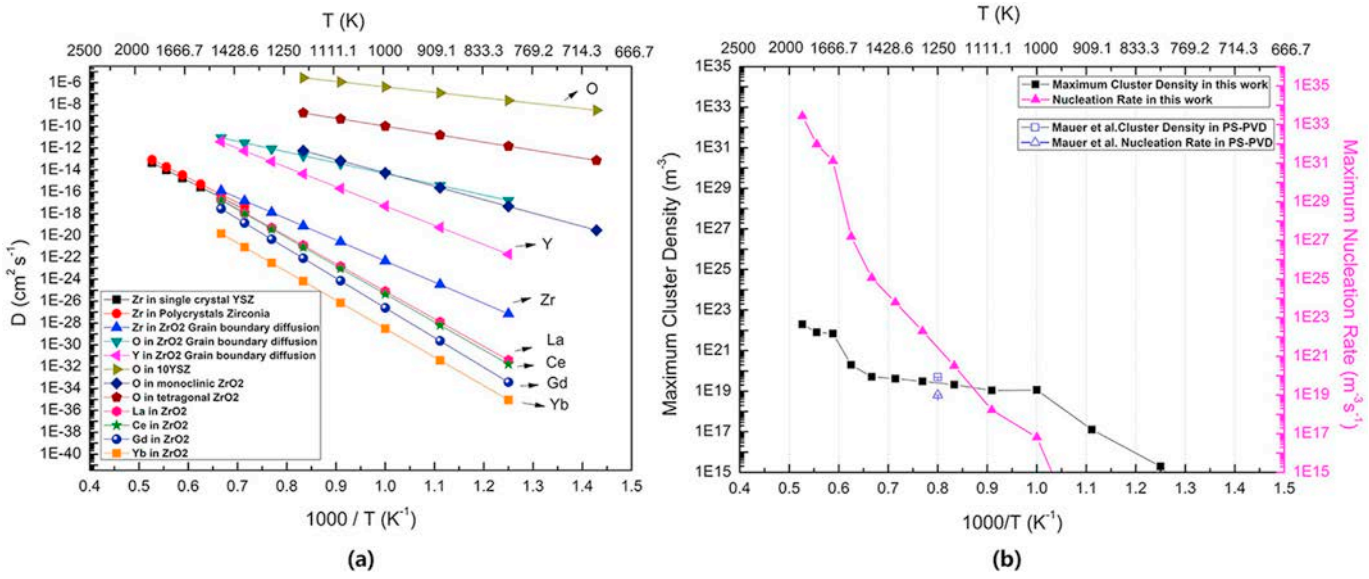

Fig. 27. Surface diffusion coefficient in YSZ (a), maximum/stable clusters density (m^{-3}) and nucleation rate ($m^{-3}s^{-1}$) as the function of 1000/T (b).

$$D = D_0 \exp(-E_a/kT) = \nu a^2 \exp(-E_a/kT_{sub}) \quad (52)$$

The flux of atoms absorbed to a cluster in a radius of R and the vapor impinging rate of J is calculated using,

$$F = 2\pi RD\left(\frac{dN}{dr}\right)_{r=R} + \pi R^2 J \quad (53)$$

The free energy of the formation of an embryo with a radius of R_c (Fig. 26-e) is calculated as

$$\Delta G = \pi R_e^2 \sin^2\theta\,(\sigma_{cs} - \sigma_{sv}) + 4\pi R_e^2 \frac{1-\cos\theta}{2}\sigma_{cv} + \frac{4}{3}\pi R_e^3 \frac{2-3\cos\theta+\cos^3\theta}{4}\Delta G_v \quad (54)$$

$$\Delta G_v = -\frac{kT_{sub}}{\nu_m}\ln\left(\frac{P}{P_e}\right) \quad (55)$$

where ν_m is the volume of an atom (cm^3), the Young's equation is expressed as

$$\sigma_{sv} - \sigma_{sc} = \sigma_{cv}\cos\theta \quad (56)$$

The contact angle (θ) will decrease owing to the higher surface tension of the high-temperature droplet [333].

In the rate equations approach, the binding energy (E_i) is described by the cluster density (N), critical-sized (i) clusters, and adatom concentration (n_x (R, t, i)),

$$(n_x/N) \sim (R/N\nu)^i r^{i+1} \exp(E_i/kT) \quad (57)$$

After the initial stage, the surface will be covered by stable nuclei, and the fraction of the area of the free surface with the contact angle increases. For a critical separation of clusters, Ls is described as:

$$L_s = 2\left(\pi/2\sqrt{3}\right)^{0.5} R_o \quad (58)$$

In addition, the critical separation can also be calculated through lattice approximation and mean-field approximation methods, these had results that agreed with the model [364].

5.3. Maximum cluster density and nucleation rate variations during the additive manufacturing of the coating

The boundary layer of the substrate has a crucial function in controlling the mass flow rate and substrate temperature. The deposition rate (kg/s or mol/s), impinging mass flow rate (kg/s) and heat flux (W/m^2) from the plasma jet to the substrate in multi-scans of the plasma spraying process are all constant. Multiple phases of deposition units existed in every scan of the plasma spray, whether the plasma spray was operated for 20 or 50 min. In the experiment, the coating that was deposited at the centerline of the plasma torch exhibited a noticeably cauliflower-like structure with a uniform interspace at the top surface and a quasi-columnar structure at the cross-section, as discussed in Section. 4.3. However, the volume of the columnar-like structure at the cross-section of the coating increased with the increasing thickness of the coating. The microstructures of the quasi-columnar YSZ coating exhibited a wide space at the top and a narrow space at the bottom of a column at the polished cross-section under constant operating conditions. Frequently, this is called a “big head” of the cauliflower-like structure; this is discussed below. Furthermore, the variations in the deposition interface in the additive manufacturing process by multiple scans of the plasma spraying will be investigated in this section.

In the columnar-like region, the diffusion of the atoms condensed from the vapor to form clusters and the coalescence of clusters are incomplete [346,366]. General rate equations to describe the relationship between cluster density (N_x, m^{-3}), diffusion coefficient (D_x, m^2/s), deposition rate(F, kg/s or mol/s) and nucleation rate (U_m, m^{-3} sec^{-1}) of thin-film deposition are used in Eqs. (59)–(61) by assuming that stable clusters have a similar diffusion coefficient [367–369].

$$D_x = D_o \exp\left(-\frac{Q}{RT}\right) \quad (59)$$

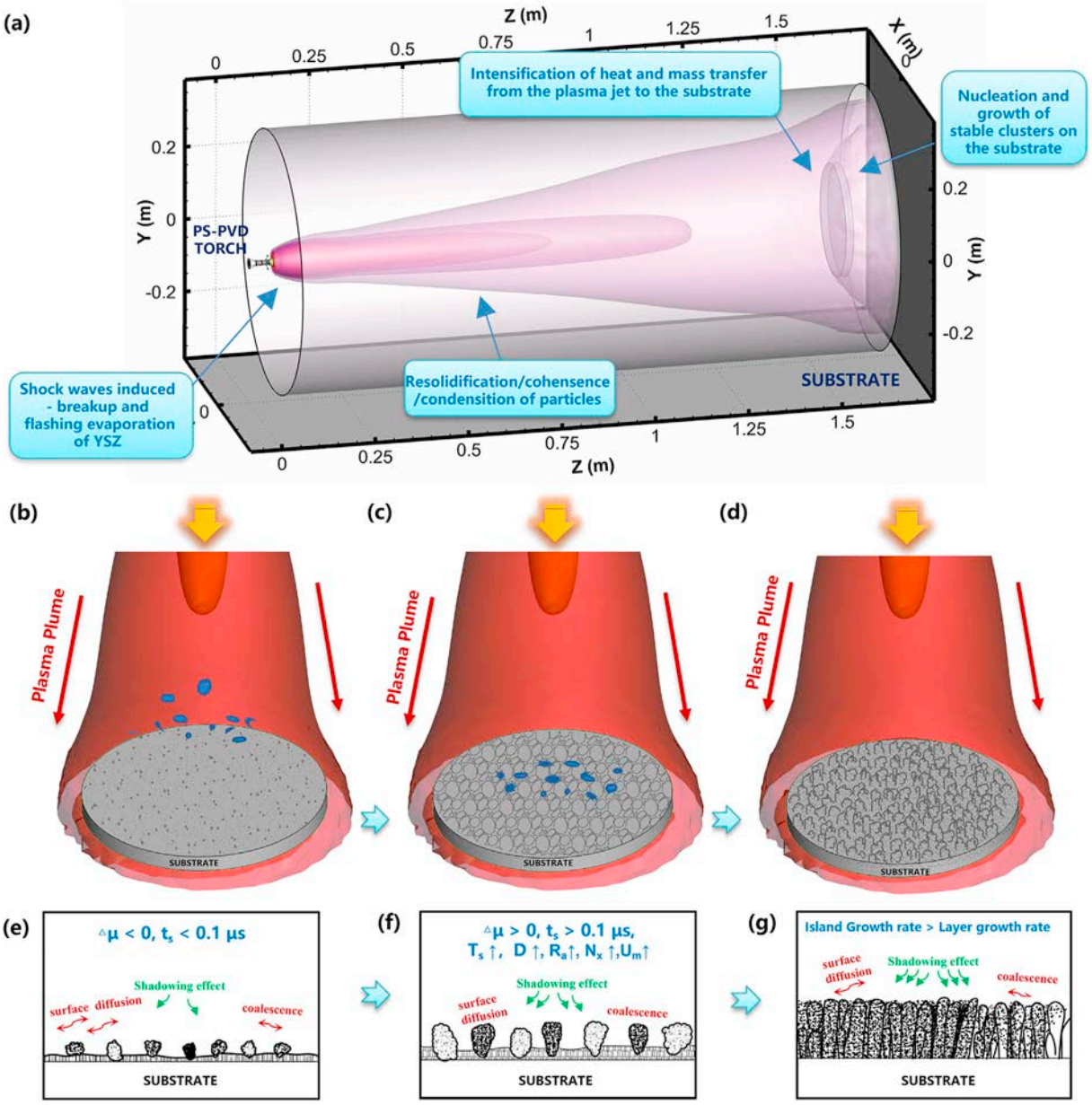

Fig. 28. Schematic representation of PS-PVD coating process (a); continuous formation of the quasi-columnar ceramic coatings on the top surface of the substrate (b), (c), (d); on the cross-sections of the substrate (e), (f), (g).

$$N_x\ (F,\ T,\ \delta_i) \approx \left(\frac{D_x}{F}\right)^{-\frac{\delta_i}{\delta_i+2}} \exp\left[\frac{E_i}{(\delta_i+2)k_B T}\right] \tag{60}$$

$$U_m = \sigma_x D_x N_x^2 \ / \ \delta_i \tag{61}$$

where δ_i is the critical size of cluster and is set to 0.2 μm; E_i is the cluster bonding energy (0.84 eV [370]); k_B is the Boltzmann constant (1.38×10^{-23} J/K), and R is the universal gas constant (8.3145 J mol^{-1} K^{-1}).

To evaluate the saturation at the deposition interface, it is described with the substrate temperature at a constant equilibrium vapor pressure according to Eq. (62). Pe is the equilibrium vapor pressure of the bulk deposition.

$$\Delta\mu = RT_{sub}\ln(p/p_e) \tag{62}$$

Accordingly, the lattice and grain boundary diffusion in the YSZ, LCO, and GZO systems as a function of the temperature are shown in Fig. 27-a, according to Keneshes et al. (1971) [371], Park et al. (1991) [372], Akash et al. (2000) [373], Swaroop et al. (2005) [374], Nakagawa et al. (2005) [375],Ghosh et al. (2011) [376], Pelleg (2013) [377], H. Shin et al. (2018) [378]. Diffusion of O is favored over diffusion of Zr, Y, La, Ce, or Gd through lattice or grain-boundary diffusion with increasing temperature. Therefore, the surface diffusion within the formerly deposited coating or thin film was significantly intensified at a high interface temperature or substrate temperature during overlapped deposition processes, e.g., the PS-PVD process. Model predictions indicated that rapid surface diffusion can accelerate the rate of increase of this contact area and the rate of densification and shrinkage [379], which means that it can induce the migration, coalescence, and decay of the deposited nanoclusters when the substrate temperature is greater than

Table 5
Ceramic powder properties used in the calculation [258,259].

Parameters	Value
Droplet surface tension of zirconia (N/m)	1.5
Viscosity of liquid zirconia (kg/m/s)	0.03692
Density of zirconia (kg/m^3)	5980
Density of gadolinia (kg/m^3)	7070
Melting point of zirconia (K)	2950
Melting point of gadolinia (K)	2693
Melting point of yttria (K)	2693
Standard enthalpy of formation of zirconia (J/kg)	−8 906 677.6
Standard enthalpy of formation of yttria (J/kg)	−8 438 040.8
Enthalpy of crystal phase transformation of zirconia (J/kg)	48 215.4
Enthalpy of crystal phase transformation of yttria (J/kg)	5743.8
Latent heat of melting of zirconia (J/kg)	706 284.8
Boiling point of zirconia (K)	4548
Boiling point of gadolinia (K)	4573
Liquid specific heat of zirconia (J/kg/K)	713
Latent heat of boiling of zirconia (J/kg)	9 000 000

1000 K throughout the process (Fig. 20).

The predicted maximum cluster density and nucleation rate are shown in Fig. 27-b. These values gradually increase as the temperature increases. Thus, maintaining an appropriate substrate temperature for the PS-PVD method is an essential condition, which then determines the movement speed between the plasma plume and substrate. In our experience, if the substrate temperature is lower than 1000 K, obtaining an advanced quasi-columnar thermal barrier coating in the experiment is difficult.

Mauer et al. (2018) indicated that the particle condensation (m^{-3}) and nucleation rates (m^{-3} s^{-1}) for PS-PVD manufactured YSZ coatings at a spraying distance of 400 mm and operating pressure of 100 Pa were in the range of 1 × 1019-^{1} × 1020 m^{-3} and 1 × 1015-^{1} × 1023 m^{-3} s^{-1}, respectively (Table 6) [383]. These results were similar to those in this study under the same operating conditions of the PS-PVD system.

To summarize (Fig. 28), during coating growth from 10 to 150 μm by multiple scan of the plasma spray, the impinging mass flow rate (kg/s), and heat flux (W/m^2) from the plasma jet to the substrate in multiple scans of the plasma spraying process were all constant. Firstly, randomly distributed stable nanoclusters were rapidly formed on the metallic substrate in 2 s (e.g., Fig. 25-a, 25-i, 25-e). Furthermore, a thin film with a thickness of 10 μm was obtained on the substrate where local areas grew at a higher rate in the vertical direction compared with the growth in the parallel direction owing to the shadow effect of impinging particles.

Moreover, the solidification time of droplets was gradually prolonged on the previously deposited ceramic layer [79], where the supersaturation of molten YSZ, stable cluster density, and nucleation rate all increased with the increase in the temperature at the deposition interface (Fig. 27). These areas shifted in favor of island formation in the kinetics, and the interface roughness increased simultaneously.

A mass of stable nano-sized clusters formed an island feature. The island structures continued to grow as a quasi-columnar feature at the cross-section of the coating. Hence, the volume of the columnar structure at the cross-section of the coating increased with increasing thickness of the coating (Fig. 28-e, 28-f, 28-g). During the growth from a thin film to a thicker coating, the self-shadowing effects of impinging particles always occurred where the smaller particles had a higher tangential velocity that caused the incident direction of the particles to deviate from the direction perpendicular to the substrate. The previously deposited particles blocked the later impinging particles at the incident direction, which aided production of more porous branched structures at the cross-section of the coating.

Simultaneously, the migration, coalescence, and decay of nano-clusters in the formerly deposited coating were induced through lattice and grain boundary diffusion on the substrate during the overlapped deposition processes of the plasma spraying, where the substrate temperature was above 1000 K throughout the entire process.

Finally, a vapor and droplet co-deposited YSZ coating was obtained using this method. A quasi-columnar structure at the cross-section of the coating and multi-cauliflower-like protrusions on the top surface of the coating were observed with a thickness of over 100 μm.

5.4. *Effects of the experimental parameters on the formation of the coating microstructure*

Although the PS-PVD torch was operated at a higher input power than compared with current plasma spray torches (Table 1 and Fig. 30), the feed rate of ceramic powder has to be significantly lower to obtain advanced quasi-columnar coatings (Table 5). Generally, the PS-PVD system should operate from 20 to 50 min, depending on the required coating thickness. The PS-PVD coating properties are sensitive to the parameters of the entire system, including the torch power (kW), chamber pressure (Pa), plasma gas species, carrier gas flow rate (SLPM), powder feed rate (g/min), translation speed of the plasma jet relative to the substrate (m/s), and spraying distance (mm). For example, when other operating conditions were constant, as the spraying distance increased from 450 to 1400 mm, the microstructure of YSZ coatings evolved from a dense lamellar structure, to a closely packed columnar structure, a quasi-columnar structure, and finally a EB-PVD-like columnar structure [14]. As the carrier gas flow rate increased from 5 to 13

Table 6
Clusters growth during physical vapor deposition in current plasma spray methods.

Parameters	ALPS	SPS	G. Mauer. et al. for PS-PVD	This Work
Particle feed rate (g min^{-1})	6	0.47 cm^3/s	7	4–8
Cluster Density (m^{-3})	1 × 10^8–1 × 10^{12}	/	1 × 10^{19}–1 × 10^{20}	1 × 10^{19}–1 × 10^{20}
Nucleation rate (m^{-3} s^{-1})	1 × 10^{18}–1 × 10^{21}	/	1 × 10^{15}–1 × 10^{23}	1 × 10^{15}–1 × 10^{23}
Growth Rate of coating (μm/min)	20–30	5–15	10–30	10–30
Spraying Distance (mm)	250	40	400/1500	1000/1200/1500
Substrate Temperature in the axis (K)	600–1000	/	1250	1100
Output Power (kW)	26	45	110–140	125
Working Gases (SLPM)	9.8 N_2 + 4.2 Ar	40 Ar+8H_2	35 Ar + 60 He	30 Ar + 60 He
Viscosity of plasma gases (kg m^{-1} s^{-1})	2.85 × 10^{-5}–2.34 × 10^{-4}	3.42 × 10^{-5}–2.75 × 10^{-4}	3.25 × 10^{-5}–2.73 × 10^{-4}	3.25 × 10^{-5}–2.73 × 10^{-4}
Particle diameter (μm)	1–30	0.060	1–30	1–30
Thickness of velocity boundary layer (mm)	0.1	0.1–2	6.8	2–4
Thickness of thermal boundary layer (mm)	0.5	/	/	1
Reference	[79]	[35,380,381]	[382,383]	

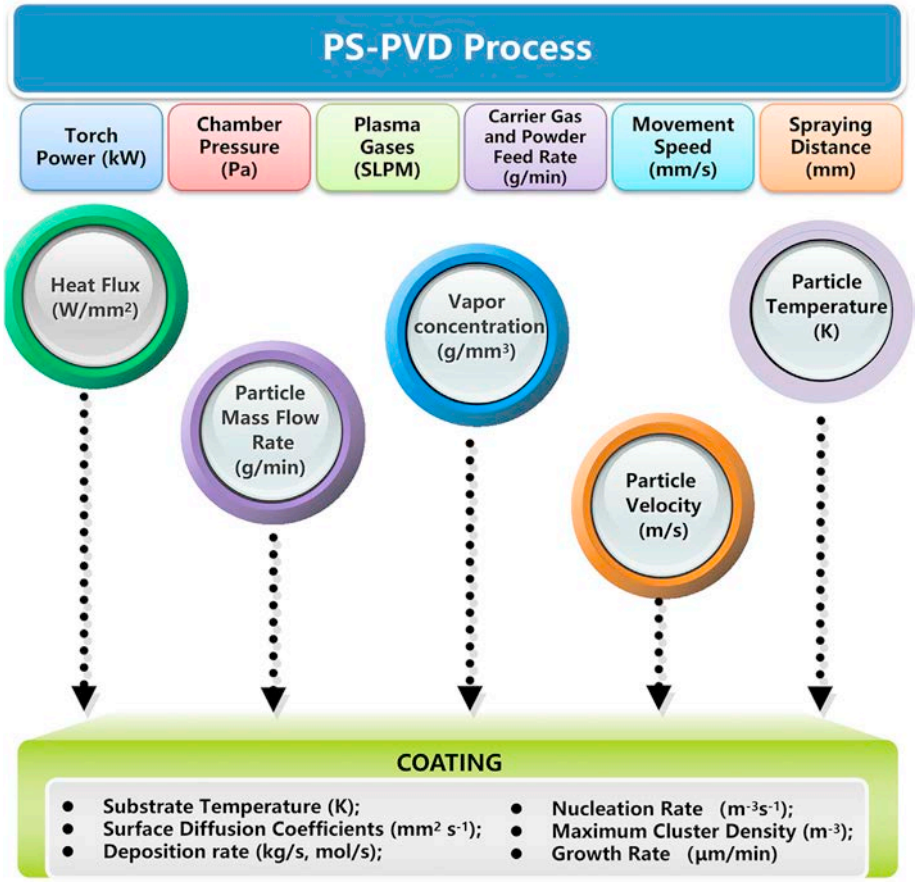

Fig. 29. Schematic representation of the effects and interactions from PS-PVD system to the coating microstructures.

SLPM, the interspace of the quasi-columnar structure of the YSZ coating at the top surface was enlarged [86]; as the powder feed rate increased from 2 to 20 g/min, the advanced quasi-columnar structure will transform into a dense layer structure where a mass of droplets were deposited, just as the result by using a conventional APS method.

As mentioned above, in such complex systems and super-long distances of multi-phase flow (Fig. 29), we should focus on the heat flux (W/mm^2), mass flow rate (kg/s), vapor concentration (g/mm^3), apparent particle velocity (m/s) and particle temperature (K) for droplets, freezing droplets, or re-solidification solid particles, which dominate the mass transfer and heat transfer process in a PS-PVD system. Furthermore, these will increase the substrate temperature (K) and surface diffusion coefficient (cm^2/s). The nucleation rate (m^{-3}s^{-1}) and maximum cluster density (mm^{-3}) were simultaneously increased with an increase in the deposition interface temperature (substrate temperature) during the additive manufacturing process of the plasma spray. Hence, the deposition rate (kg/s, mol/s), deposition flux (kg m^{-2} s^{-1}), and growth rate (μm/min) were used to characterize the growth of the coating.

In addition, authors used the vaporization rate (kg m^{-2} s^{-1}) [241,384], vapor capacity (g/min) [334], vapor mass source (kg/s) [253], vaporization efficiency (%) [385], or evaporated mass rate (g/min) [386] to characterize the physical vapor process in the deposition, which are physically similar quantities.

Fig. 30-a lists the importance of five experimental parameters in the formation of coatings in the PS-PVD system. A comparison of the input power and total gas flow rate of the ALPS torch, Sulzer F4-VB torch, Praxair SG-100 Gun, Triplex Pro 210 Torch and the PS-PVD torch is shown in Fig. 30-b. A high-input-power plasma torch and applicable spraying distance are important factors in obtaining an advanced quasi-columnar ceramic coating. The mean free path is the average distance that a particle can travel between two successive collisions with other particles. The gas mean free path for current low-pressure deposition methods at 300 K is given in Fig. 30-c. In the CVD methods, vapor molecules can collide with the substrate surface many times before adsorbing to the surface and deposit on non-line of sight regions of complex components by multiple reflections [387–389]. In these PVD methods, low deposition pressures can prevent particle formation and ensure atom-by-atom coating growth [390]. Vapor atoms flight in free path without undergoing interparticle collisions during transport from their source to the substrate at a low pressure [391–393]. Hence, mean free path between gas molecule collisions must be smaller than the length of the substrate surfaces to ensure the vapor molecules to access these complex surfaces (e.g., double guide vanes).

6. Critical challenges and new directions

Although extensive research has been conducted, further investigations are still required to clarify the existing problems that have not been fully understood. Potential topics that require further study are listed as follows.

6.1. Advanced in-situ experimental measurement and numerical theories

In plasma spray torches, it is evident that the plasma properties

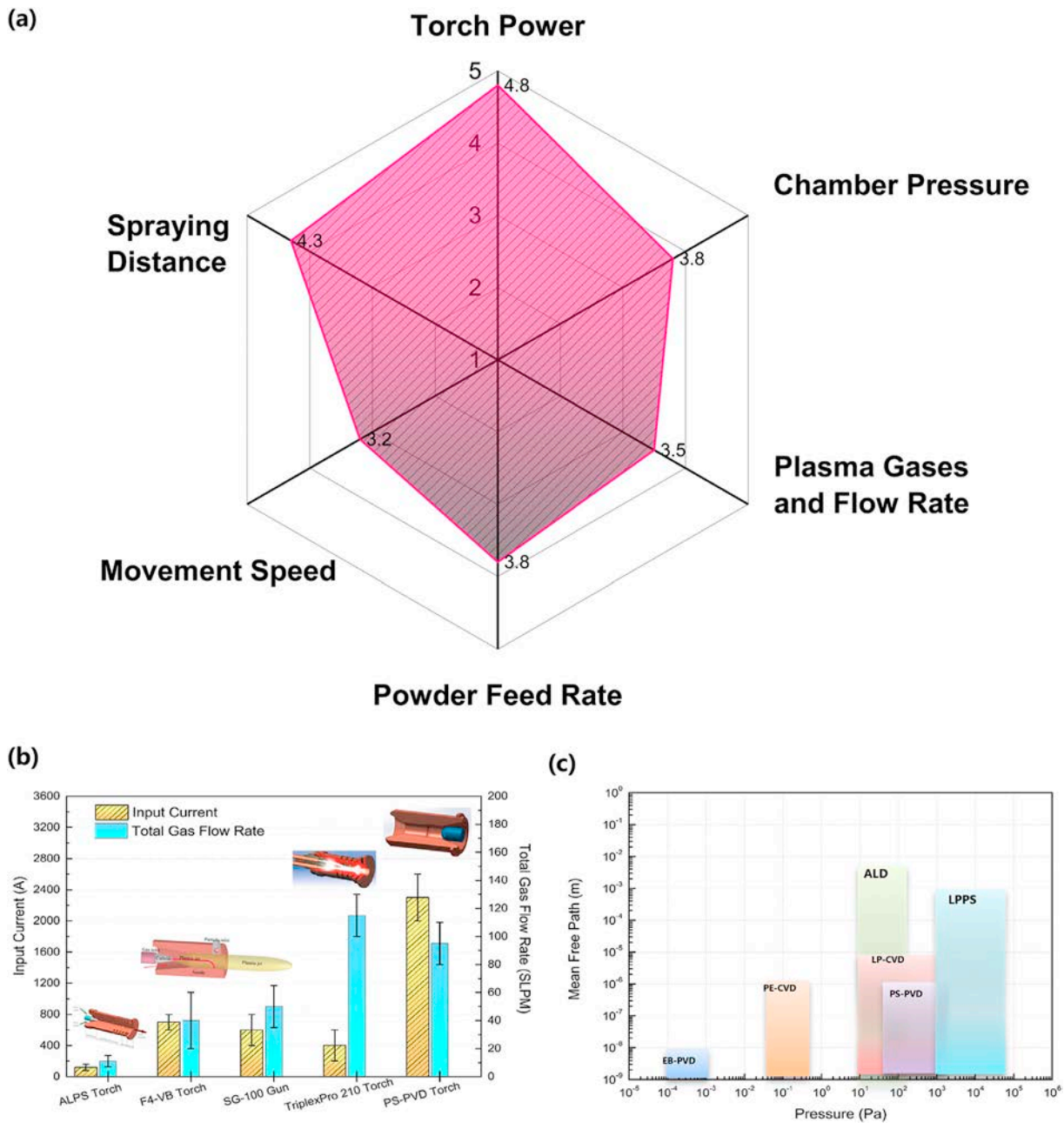

Fig. 30. Effects of experimental parameters in PS-PVD process on the formation of quasi-columnar ceramic coatings (a); input power and total gas flow rate of current plasma spray torches (b); mean free path of current low-pressure deposition methods (c).

(particle densities, temperatures of electrons and heavy particles) can differ in the plasma depending on the description of the electron transport [394,395]. Large regions are exist where kinetic equilibrium between heavy-particles and electrons is not achieved, not only near the electrodes [396], but also in the plasma jet region with cold carrier gases (e.g., internal powder injection of the plasma spraying). Thermal non-equilibrium in those regions is due to the imbalance between transport and kinetic equilibration processes [397]. The state-of-the-art in arc modelling would have to include deviations from local thermal equilibrium and local chemical (ionization) equilibrium in both the near-electrode regions and the fringes of the arc [192,398]. To model the plasma spraying more accurately, the local thermal equilibrium (LTE) assumption needs to be abandoned in favor of a thermal non-equilibrium (NLTE) and a chemical non-equilibrium (NCE) description in which the heavy-particles and electrons are assumed to have separate Maxwellian distributions.

The interest in non-equilibrium effects in arc plasma has grown during the last decade, experimental studies are still scarce. Experimental measurements can provide visualized and directly results, although the measurements should provide multiple quantities during the plasma spraying. The connections among the directly measured quantities are most readily understood by comparing values that can be calculated from them. A significant challenge of experimental measurement still exists inside the low-pressure chamber, including the difference between electrons and heavy particles of the plasma gas. The commercial systems that based on the optical or probe method should develop a specific

device that can operate inside the chamber, many works are still necessary before a real online control can be developed.

Moreover, the effects of the electromagnetic field of the plasma jet on the substrate are still unknown. The in-flight particles may be charged under non-equilibrium conditions, and charging can significantly affect the agglomeration of clusters, which also deserves more studies.

6.2. Preparation of powder feedstocks and new materials

In experiment, the characteristics of powder feedstocks are very critical in the PS-PVD process to produce quasi-columnar structured ceramic coatings. The specifically designed nano-agglomerated ceramic powders (e.g., Metco 6700-8YSZ, d = 1–30 μm, d_{50} = 10 μm, Oerlikon Metco, Westbury, USA) is a majority chose in PS-PVD processes to make sure that the powders can reach to the hottest zone of the plasma plume as possible. The nano-agglomerated ceramic powders usually produced using solid-phase reaction through spray drying and heat treatment (sintering) at high temperature to enhance the binding strength between the primary particles. Typically, the production processes include mixture slurry (deionized water, dispersant, or organic binder), ball milling, spray dry, sintering, etc. The consistently spheroidal particle shape of the agglomerated and sintered materials provides reliable flow and structural stability.

In fact, a quite low particle feed rate was employed in the PS-PVD method, while the input power of plasma torch is higher than conventional APS methods. The PS-PVD process meet challenges owing to the complex structure of blades and increased working temperature. Attempts to use different types of ceramic powder would be interesting and challenging. It is an urgent need to develop new ceramic materials with better performance to address the challenges facing industry production requirements. Hence, effects in this project may be worth pursuing.

6.3. Paradox between the column density and corrosion/wear resistance

Depending on the column density, the strain compliance of coatings can be significantly improved. However, the pores in the inter-space of columns are usually interconnected through the whole coating, which allows easy penetration of a corrosive gaseous or liquid material to the coating/substrate interface. The adhesion and irregular growth of the corrosion products on the coating is generated additional stresses and accelerate the coating failure.

Solid particle erosion is another failure mode of TBCs when the gas turbines operate in the sandy and ashy environments [399]. The individual column will be cracked due to impact particles [400], cracks can nucleate and propagate due to stress concentration induced by subsequent impacts and easily propagate along neighbouring columns [401]. Then, crack bands propagate conically toward the coating and will promote delaminations of the coating [402,403]. Typically, a dense microstructure of the coating guarantees a better resistance to impacts from solid particle.

It is still a great challenge how to deposit a ceramic coating of a high column density which can provide a metal substrate with excellent corrosion resistance and excellent wear resistance. On the other hand, the interface bonding dominates the coating physical and mechanical properties because a variety of coating properties are proportional to interface bonding strength. The dominant bonding mechanism is related to process parameters and can change with them. Failure of the PS-PVD manufactured TBCs after corrosion and wear test should analyse to gain further insights, which has not been well identified in detail.

6.4. Potential applications in industry

The conventional PVD processes are mainly applied for thin coating productions and can only cover surfaces which are in direct line of sight to the coating source. Substrates with complex geometries are very difficult to coat homogeneously. Hence, the drawbacks of conventional PVD processes compared to thermal spray are high investment costs and low deposition rates.

The depositing position of PS-PVD processing is broadened and more homogeneous so that the coating area is enlarged. This process is capable to coat areas which are not in the line of sight of the substrate and makes the coverage of substrates with complex geometries possible (e.g., multiple turbine air foils). It offers novel opportunities for the application of thermal spray technology. This process gives the possibility to deposit thin or thick coatings for special applications through a plasma spray approach in low pressure environment, and reduce of oxidation from the substrate. It fills the gap between conventional plasma spray and EB-PVD, and also opens new application fields in which neither plasma spraying nor PVD processes.

Moreover, PS-PVD method significantly improved the working environment of workers since the chamber effectively prevented the potential risks due to gases, toxicity of powders, vapors and dusts production, noise, radiation, high temperatures of the different processes, and electrical equipment.

Therefore, it has a great potential in the domain of new energy concepts in applications like Solid Oxide Fuel Cells, membranes, photovoltaic cell, replacement of hard chromium, as well as ornamental applications with the adoption of new ways of producing coatings by thermal spray. The applications of PS-PVD not only limited to high-added value components in the aeronautic and nuclear industry, but also a wide range of industrial requirement became available.

7. Summary

The multi-phase flow characteristics in the PS-PVD process were analyzed using a three-dimensional numerical simulations and experiments. The formation of a quasi-columnar YSZ coating was reviewed. The following conclusions can be drawn:

(1) PS-PVD coatings with unique microstructure can be deposited. The cross-section exhibits a quasi-columnar structure, and multiple cauliflower-like protrusions are present on the top surface. The coatings have an excellent thermal cycling lifetime compared to other methods, indicating their potential for TBCs.

(2) The maximum velocity of the low-pressure plasma gas was in the shock region and outside the torch nozzle, while the maximum temperature of the low-pressure plasma gas was inside the plasma torch and gradually decreased after ejection from the torch nozzle. At an input current of 2000 A using 30 SLPM argon and 60 SLPM helium, the maximum plasma gas temperatures at the torch nozzle under chamber pressures of 50, 100, 200 and 1000 Pa are predicted to be 12850.7, 12849.3, 12823.7 and 12826.5 K, respectively. The corresponding maximum plasma gas velocities in the chamber pressure of 50, 100, 200 and 1000 Pa are 6519.4, 6508.6, 6474.8, 6294.2 m/s, respectively.

(3) The flight trajectories of particles in the chamber depended on the particle diameters. Particles with diameters of 1–5 μm flowed along the streamlines of the plasma jet to a maximum distance of 2200 mm and remained close to the centerline. Particles with diameters of 5–12 μm exited the torch at a large angle and departed from the centerline of the plasma

jet. Particles with diameters of 25–30 μm deviated from the centerline of the plasma jet and impinged on the chamber wall.

(4) The mechanism underlying of the self-shadowing of impinging particles in repeated deposition passes was examined. It was shown that smaller YSZ particles follow the gs flow as it is diverted parallel to the substrate. Previously deposited particles block the substrate impinging particles, which helps to produce more porous branched structure in the coating cross-section.

(5) The plasma jet shockwaves induced flash vaporization, and the associated breakup of YSZ materials was classified. Before, vaporization occurs, the YSZ powders are primarily melted into liquid columns, the liquid is abruptly accelerated by the perpendicular plasma gas flow, and the larger drops breakup into smaller drops. The deposition units in the PS-PVD process were concluded to be secondary breakup droplets, re-solidified particles and particles from vapor condensation.

(6) Kinetic surface diffusion, migration, coalescence and decay of nano-clusters in the additive manufacturing of the coating always occur when the substrate temperature is above 1000 K during the entire process. The surface diffusion coefficient, maximum cluster density, and nucleation rate all increase with increasing temperature.

(7) In a PS-PVD system, torch power (kW), chamber pressure (Pa), plasma gas species and carrier gas flow rate (SLPM), powder feed rate (g/min), movement speed from the plasma jet to the substrate (m/s), and spraying distance (mm) co-control the quality of ceramic coatings. Among these conditions, a high input power plasma torch and applicable spraying distance have the dominant functions in obtaining an advanced quasi-columnar ceramic coating.

Declaration of competing interest

The authors declare that they have no known competing financial interests or personal relationships that could have appeared to influence the work reported in this paper.

Acknowledgments

The authors are grateful to the Massachusetts Green High-Performance Computing Center (MGH - PCC). This work was supported by the Natural Key R&D Program of China (Basic Research Project, Grant No.2017YFB0306104), National Natural Science Foundation of China (Grant No.91860114,51590894,51901011) and the China Postdoctoral Foundation (Grant No. 230210558). National Science and Technology Major Project (No. 2017-VI-0010-0081).

The data presented in this paper are available on request from the authors.

References

[1] K. von Niessen, M. Gindrat, Plasma spray-PVD: a new thermal spray process to deposit out of the vapor phase, J. Therm. Spray Technol. 20 (4) (2011) 736–743.
[2] B. Lv, R. Mücke, X. Fan, T.J. Wang, O. Guillon, R. Vaßen, Sintering resistance of advanced plasma-sprayed thermal barrier coatings with strain-tolerant microstructures, J. Eur. Ceram. Soc. 38 (15) (2018) 5092–5100.
[3] K. Wada, Y. Ishiwata, N. Yamaguchi, H. Matsubara, Strain tolerance and microstructure of thermal barrier coatings produced by electron beam physical vapor deposition process, Mater. Sci. Forum (2006) 267–276.
[4] Z. Salhi, D. Klein, P. Gougeon, C. Coddet, Development of coating by thermal plasma spraying under very low-pressure condition, Vacuum 77 (2) (2005) 145–150.
[5] K. Von Niessen, M. Gindrat, A. Refke, Vapor phase deposition using plasma spray-PVD, J. Therm. Spray Technol. 19 (1–2) (2010) 502–509.
[6] K. Iizuka, M. Kambara, T. Yoshida, Growth of tin oxide thick films by plasma spray physical vapor deposition, Sensor. Actuator. B Chem. 155 (2) (2011) 551–556.
[7] A. Shinozawa, K. Eguchi, M. Kambara, T. Yoshida, Feather-like structured YSZ coatings at fast rates by plasma spray physical vapor deposition, J. Therm. Spray Technol. 19 (1–2) (2010) 190–197.
[8] Yang Gao, Development tendencies of the very low-pressure plasma spraying and deposition technology, Therm. Spray Technol. 3 (2) (2010) (In Chinese).
[9] M.D. Yang, Yang Gao, Effect of plasma spraying methods and the morphology of powder on the microstructure of ZrO_2-8%Y_2O_3 coating, Therm. Spray Technol. 2 (4) (2012) (In Chinese).
[10] A. Hospach, G. Mauer, R. VaEn, D. StVer, Characteristics of ceramic coatings made by thin film low-pressure plasma spraying (lpps-tf), J. Therm. Spray Technol. 21 (3–4) (2012) 435–440.
[11] M.F. Smith, A.C. Hall, J.D. Fleetwood, P. Meyer, Very low-pressure plasma spray-a review of an emerging technology in the thermal spray community, Coatings 1 (2) (2011) 117–132.
[12] B. Harder, PS-PVD processing varies coating architecture with processing parameters, Adv. Mater. Process. 169 (8) (2011) 49–51.
[13] M. Goral, S. Kotowski, A. Nowotnik, M. Pytel, M. Drajewicz, J. Sieniawski, PS-PVD deposition of thermal barrier coatings, Surf. Coating. Technol. 237 (Complete) (2013) 51–55.
[14] C. Li, H.B. Guo, L.H. Gao, L. Wei, S. Gong, H.B. Xu, Microstructures of yttria-stabilized zirconia coatings by plasma spray-physical vapor deposition, J. Therm. Spray Technol. 24 (3) (2014) 534–541.
[15] Q.Y. Chen, X.Z. Peng, G.J. Yang, C.X. Li, C.J. Li, Characterization of plasma jet in plasmaspray-ph ysical vapor deposition of YSZ using a < 80 kW shrouded torch based on optical emission spectroscopy, J. Therm. Spray Technol. 24 (6) (2015) 1038–1045.
[16] Chen QY, Li CX, Li CJ, Luo XT, Yang GJ. Columnar structure YSZ coating formation by PS-PVD using conventional plasma spray system assisted through droplet filtering. Proceedings of 2015International Thermal Spray Conference.
[17] C. Song, Y. Wang, X. Fan, S. Xie, M. Liu, K. Zhou, H. Liao, Microstructure and mechanical property of dense yttria-stabilized zirconia coating fabricated by an axial bi-cathode plasma torch under very low-pressure, Ceram. Int. 46 (7) (2020) 9507–9511.
[18] F. Shao, H. Zhao, C. Liu, X. Zhong, Y. Zhuang, J. Ni, et al., Dense yttria-stabilized zirconia coatings fabricated by plasma spray-physical vapor deposition, Ceram. Int. 43 (2) (2017) 2305–2313.
[19] J. Yang, H. Zhao, X. Zhong, F. Shao, C. Liu, Y. Zhuang, et al., Thermal cycling behavior of quasi-columnar ysz coatings deposited by ps-pvd, J. Therm. Spray Technol. 26 (1–2) (2017) 132–139.
[20] Li-hua Gao, Yue-guang Yu, Fang Jia, Ji Xiao-juan, De-ming Zhang, Progress in plasma spray-physical vapor deposition thermal barrier coatings, Therm. Spray Technol. 2 (9) (2017) (In Chinese).
[21] Li-hua Gao, Xiaojuan Ji, Wei Hou, Xiaoliang Lu, Deming Zhang, Thermal shock resistance property of quasi -columnar YSZ thermal barrier coatings prepared by plasma spray-physical vapor deposition, Mater. Rep. 33 (6) (2019) (In Chinese).
[22] P. Xu, T.W. Coyle, L. Pershin, J. Mostaghimi, Fabrication of superhydrophobic ceramic coatings via solution precursor plasma spray under atmospheric and low-pressure conditions, J. Therm. Spray Technol. 28 (1–2) (2019) 242–254.
[23] S.H. Liu, S. Lin, Sen-Hui Liu, Shan-Lin Zhang, Cheng-Xin Li, Li Lu, Jia-Hua Huang, Trelles Juan Pablo, B. Anthony, C.L. Murphy, Generation of long laminar plasma jets: experimental and numerical analyses, Plasma Chem. Plasma Process. 1–11 (2019), 0123456789.
[24] H.-J. Rätzer-Scheibe, U. Schulz, The effects of heat treatment and gas atmosphere on the thermal conductivity of APS and EB-PVD PYSZ thermal barrier coatings, Surf. Coating. Technol. 201 (18) (2007) 7880–7888.
[25] C. Lamuta, G.D. Girolamo, L. Pagnotta, Microstructural, mechanical and tribological properties of nanostructured YSZ coatings produced with different APS process parameters, Ceram. Int. 41 (7) (2015) 8904–8914.
[26] B. Bernard, L. Bianchi, A. Malié, A. Joulia, B. Rémy, Columnar suspension plasma sprayed coating microstructural control for thermal barrier coating application, J. Eur. Ceram. Soc. 36 (4) (2016) 1081–1089.
[27] R. Darolia, Thermal barrier coatings technology: critical review, progress update, remaining challenges and prospects, Int. Mater. Rev. 58 (6) (2013) 315–348.
[28] U. Schulz, C. Leyens, K. Fritscher, M. Peters, B. Saruhan-Brings, O. Lavigne, M. Caliez, Some recent trends in research and technology of advanced thermal barrier coatings, Aero. Sci. Technol. 7 (1) (2003) 73–80.
[29] I.G. Wright, T. Gibbons, Recent developments in gas turbine materials and technology and their implications for syngas firing, Int. J. Hydrogen Energy 32 (16) (2007) 3610–3621.
[30] G. Mauer, M.O. Jarligo, S. Rezanka, A. Hospach, R. Vaßen, Novel opportunities for thermal spray by PS-PVD, Surf. Coating. Technol. 268 (2015) 52–57.
[31] S. Rezanka, G. Mauer, R. Vaßen, Improved thermal cycling durability of thermal barrier coatings manufactured by PS-PVD, J. Therm. Spray Technol. 23 (1) (2014) 182–189.
[32] S. Rezanka, D.E. Mack, G. Mauer, D. Sebold, O. Guillon, R. Vaßen, Investigation of the resistance of open-column-structured PS-PVD TBCs to erosive and high-temperature corrosive attack, Surf. Coating. Technol. 324 (2017) 222–235.

[33] B.J. Harder, D. Zhu, Plasma spray-physical vapor deposition (PS-PVD) of ceramics for protective coatings, Adv. Ceram. Coating. Mater. Extrem. Environ.: Ceram. Eng. Sci. Proc. 32 (2011) 71–84.

[34] Y. Zhang, C. Deng, J. Mao, Z. Luo, Z. Deng, X. Zhang, C. Deng, Impact of cathode loss on plasma characteristics, microstructures and properties of 7YSZ coatings in PS-PVD, Ceram. Int. 46 (9) (2020) 13307–13316.

[35] P.L. Fauchais, J.V.R. Heberlein, M.I. Boulos, Thermal Spray Fundamentals, Springer Science+Business Media, NewYork, 2014.

[36] L. Pawlowski, The Science and Engineering of Thermal Spray Coatings, John Wiley & Sons, Ltd, 1995, ISBN 9780470754085, https://doi.org/10.1002/9780470754085.

[37] N.P. Padture, M. Gell, P.G. Klemens, Ceramic materials for thermal barrier coatings, J. Eur. Ceram. Soc. (2004).

[38] N.P. Padture, Thermal barrier coatings for gas-turbine engine applications, Science 296 (5566) (2002) 280–284.

[39] R. Vaßen, M.O. Jarligo, T. Steinke, D.E. Mack, D. Stöver, Overview on advanced thermal barrier coatings, Surf. Coating. Technol. 205 (4) (2010) 938–942.

[40] W. Uczak de Goes, N. Markocsan, M. Gupta, R. Vaßen, T. Matsushita, K. Illkova, Thermal barrier coatings with novel architectures for diesel engine applications, Surf. Coating. Technol. 396 (May) (2020).

[41] K.W. Schlichting, N.P. Padture, P.G. Klemens, Thermal conductivity of dense and porous yttria-stabilized zirconia, J. Mater. Sci. 6 (2001) 3003–3010.

[42] R. Vassen, X. Cao, F. Tietz, D. Basu, D. Stöver, Zirconates as new materials for thermal barrier coatings, J. Am. Ceram. Soc. 83 (8) (2004) 2023–2028.

[43] J. Wu, X. Wei, N.P. Padture, P.G. Klemens, M. Gell, P. Miranzo, M.I. Osendi, Low-thermal-conductivity rare-earth zirconates for potential thermal-barrier-coating applications, J. Am. Ceram. Soc. 35 (2002) 3031–3035.

[44] S. Krämer, J. Yang, C.G. Levi, Infiltration-inhibiting reaction of gadolinium zirconate thermal barrier coatings with CMAS melts, J. Am. Ceram. Soc. 91 (2) (2008) 576–583.

[45] E. Bakan, D.E. Mack, G. Mauer, R. Vaßen, Gadolinium zirconate/YSZ thermal barrier coatings: plasma spraying, microstructure, and thermal cycling behavior, J. Am. Ceram. Soc. 97 (12) (2014) 4045–4051.

[46] D.R. Clarke, S.R. Phillpot, Thermal barrier coating materials, Mater. Today 8 (6) (2005) 22–29.

[47] W. Ma, S. Gong, H. Xu, X. Cao, The thermal cycling behavior of Lanthanum–Cerium Oxide thermal barrier coating prepared by EB–PVD, Surf. Coating. Technol. 200 (16) (2006) 5113–5118.

[48] A. Joulia, M. Vardelle, S. Rossignol, Synthesis and thermal stability of $Re_2Zr_2O_7$, (Re = La, Gd) and $La_2(Zr_{1-x}Ce_x)_2O_{7-\delta}$ compounds under reducing and oxidant atmospheres for thermal barrier coatings, J. Eur. Ceram. Soc. 33 (13) (2013) 2633–2644.

[49] A. Vardelle, C. Moreau, J. Akedo, et al., The 2016 thermal spray roadmap, J. Therm. Spray Technol. 25 (8) (2016) 1376–1440.

[50] O. Racek, C.C. Berndt, D.N. Guru, J.V.R. Heberlein, Nanostructured and conventional YSZ coatings deposited using APS and TTPR techniques, Surf. Coating. Technol. 201 (1) (2006) 338–346.

[51] P. Arunkumar, U. Aarthi, M. Sribalaji, B. Mukherjee, A.K. Keshri, W.H. Tanveer, K.S. Babu, Deposition rate dependent phase/mechanical property evolution in zirconia and ceria-zirconia thin film by EB-PVD technique, J. Alloys Compd. 765 (2018) 418–427.

[52] J. Singh, D.E. Wolfe, J. Singh, Architecture of thermal barrier coatings produced by electron beam-physical vapor deposition (EB-PVD), J. Mater. Sci. 37 (15) (2002) 3261–3267.

[53] J. Singh, D.E. Wolfe, Review Nano and macro-structured component fabrication by electron beam-physical vapor deposition (EB-PVD), J. Mater. Sci. 40 (1) (2005) 1–26.

[54] J.R. Nicholls, K.J. Lawson, A. Johnstone, D.S. Rickerby, Methods to reduce the thermal conductivity of EB-PVD TBCs, Surf. Coating. Technol. 151 (2002) 383–391.

[55] U. Schulz, B. Saruhan, K. Fritscher, C. Leyens, Review on advanced EB-PVD ceramic topcoats for TBC applications, Int. J. Appl. Ceram. Technol. 1 (4) (2005) 302–315.

[56] M. Peters, C. Leyens, U. Schulz, W.A. Kaysser, EB-PVD thermal barrier coatings for aeroengines and gas turbines, Adv. Eng. Mater. 3 (4) (2001) 193–204.

[57] P. Song, D. Naumenko, R. Vassen, L. Singheiser, W.J. Quadakkers, Effect of oxygen content in NiCoCrAlY bondcoat on the lifetimes of EB-PVD and APS thermal barrier coatings, Surf. Coating. Technol. 221 (2013) 207–213.

[58] P. Fauchais, G. Montavon, M. Vardelle, J. Cedelle, Developments in direct current plasma spraying, Surf. Coating. Technol. 201 (2006) 1908–1921.

[59] H.B. Guo, R. Vaßen, D. Stöver, Atmospheric plasma sprayed thick thermal barrier coatings with high segmentation crack density, Surf. Coating. Technol. 186 (3) (2004) 353–363.

[60] M. Gell, E.H. Jordan, M. Teicholz, B.M. Cetegen, N.P. Padture, L. Xie, D. Chen, Thermal barrier coatings made by the solution precursor plasma spray process, J. Therm. Spray Technol. 17 (March) (2008) 124–135.

[61] M. Mutter, G. Mauer, R. Mücke, O. Guillon, R. Vaßen, Correlation of splat morphologies with porosity and residual stress in plasma-sprayed YSZ coatings, Surf. Coating. Technol. 318 (2017) 157–169.

[62] Q. Li, P. Song, K. Lü, Q. Dong, Q. Li, J. Tan, J. Lu, Fracture behaviour of ceramic–metallic glass gradient transition coating, Ceram. Int. 45 (5) (2019) 5566–5576.

[63] A. Meghwal, A. Anupam, B.S. Murty, C.C. Berndt, R.S. Kottada, A.S.M. Ang, Thermal spray high-entropy alloy coatings: a review, J. Therm. Spray Technol. (2020).

[64] F. Zhou, Y. Wang, M. Liu, C. Deng, Y. Li, Y. Wang, X. Zhang, Bonding strength and thermal conductivity of novel nanostructured La 2 (Zr 0.75 Ce 0.25) 2 O 7/8YSZ coatings, Appl. Surf. Sci. 481 (January) (2019) 460–465.

[65] L. Pawlowski, Suspension and solution thermal spray coatings, Surf. Coating. Technol. 203 (19) (2009) 2807–2829.

[66] H. Kassner, R. Siegert, D. Hathiramani, R. Vassen, D. Stoever, Application of suspension plasma spraying (SPS) for manufacture of ceramic coatings, J. Therm. Spray Technol. 17 (1) (2008) 115–123.

[67] R. Kumar, D. Cietek, C. Jiang, J. Roth, M. Gell, E.H. Jordan, Influence of microstructure on the durability of gadolinium zirconate thermal barrier coatings using APS & SPPS processes, Surf. Coating. Technol. 337 (2018) 117–125.

[68] P. Fauchais, G. Montavon, R.S. Lima, B.R. Marple, Engineering a new class of thermal spray nano-based microstructures from agglomerated nanostructured particles, suspensions and solutions: an invited review, J. Phys. D 44 (9) (2011) 93001.

[69] A. Guignard, G. Mauer, R. Vaßen, D. Stöver, Deposition and characteristics of submicrometer-structured thermal barrier coatings by suspension plasma spraying, J. Therm. Spray Technol. 21 (3) (2012) 416–424.

[70] J.W. Adams, R. Ruh, K.S. Mazdiyasni, Young's modulus, flexural strength, and fracture of yttria-stabilized zirconia versus temperature, J. Am. Ceram. Soc. 80 (4) (2005) 903–908.

[71] L. Guo, H. Guo, H. Peng, S. Gong, Thermophysical properties of Yb_2O_3 doped $Gd_2Zr_2O_7$ and thermal cycling durability of $(Gd_{0.9}Yb_{0.1})_2Zr_2O_7$/YSZ thermal barrier coatings, J. Eur. Ceram. Soc. 34 (5) (2014) 1255–1263.

[72] X. Wang, L. Guo, H. Peng, L. Zheng, H. Guo, S. Gong, Hot-corrosion behavior of a $La_2Ce_2O_7$/YSZ thermal barrier coating exposed to Na_2SO_4+V_2O_5 or V_2O_5 salt at 900 °C, Ceram. Int. 41 (5) (2015) 6604–6609.

[73] T. Liu, S. Yao, L. Wang, G. Yang, C. Li, C. Li, Plasma-sprayed thermal barrier coatings with enhanced splat bonding for CMAS and corrosion protection, J. Therm. Spray Technol. 25 (January) (2016) 213–221.

[74] T. Liu, S. Zhang, X. Luo, G. Yang, C. Li, C. Li, High heat insulating thermal barrier coating designed with large two-dimensional inter- lamellar pores, J. Therm. Spray Technol. 25 (1) (2016) 222–230.

[75] S. Pal, A. Deore, N.M. Alford, A. Templeton, S.J. Penn, High temperature thermal properties of columnar yttria stabilized zirconia thermal barrier coating performed, J. Phys. Conf. (745) (2016): 032012.

[76] D. Zhou, J. Malzbender, Y.J. Sohn, O. Guillon, R. Vaßen, Sintering behavior of columnar thermal barrier coatings deposited by axial suspension plasma spraying (SPS), J. Eur. Ceram. Soc. 39 (2–3) (2019) 482–490.

[77] D. Zhou, D.E. Mack, E. Bakan, G. Mauer, D. Sebold, O. Guillon, R. Vaßen, Thermal cycling performances of multilayered yttria-stabilized zirconia/gadolinium zirconate thermal barrier coatings, J. Am. Ceram. Soc. 103 (3) (2020) 2048–2061.

[78] S.H. Liu, C.X.C.J. Li, H.Y. Zhang, S.L. Zhang, L. Li, P. Xu, G.J. Yang, C.X.C.J. Li, A novel structure of YSZ coatings by atmospheric laminar plasma spraying technology, Scripta Mater. 153 (2018) 73–76.

[79] S.-H. Liu, J.P. Trelles, C.-J. Li, H.B. Guo, C.-X. Li, Numerical analysis of the plasma-induced self-shadowing effect of impinging particles and phases transformation in a novel long laminar plasma jet, J. Phys. Appl. Phys. 53 (2020) 375202.

[80] X.Q. Cao, R. Vassen, D. Stoever, Ceramic materials for thermal barrier coatings, J. Eur. Ceram. Soc. 24 (1) (2004) 1–10.

[81] X.Q. Cao, R. Vassen, W. Jungen, S. Schwartz, F. Tietz, D. Stöver, Thermal stability of lanthanum zirconate plasma-sprayed coating, J. Am. Ceram. Soc. 84 (9) (2004) 2086–2090.

[82] X. Cao, R. Vassen, W. Fischer, F. Tietz, W. Jungen, D. Stover, Lanthanum–cerium oxide as a thermal barrier-coating material for high-temperature applications, Adv. Mater. 15 (17) (2003) 1438–1442.

[83] R. Vassen, X. Cao, F. Tietz, D. Basu, D. Stöver, Zirconates as new materials for thermal barrier coatings, J. Am. Ceram. Soc. 83 (8) (2004) 2023–2028.

[84] J. He, H. Guo, H. Peng, S. Gong, Microstructural, mechanical and oxidation features of NiCoCrAlY coating produced by plasma activated EB-PVD, Appl. Surf. Sci. 274 (2013) 144–150.

[85] H. Peng, H. Guo, J. He, S. Gong, Oxidation and diffusion barrier behaviors of double-layer NiCoCrAlY coatings produced by plasma activated EB-PVD, Surf. Coating. Technol. 205 (19) (2011) 4658–4664.

[86] B.P. Zhang, L. Wei, L. Gao, H.B. Guo, H.B. Xu, Microstructural characterization of PS-PVD ceramic thermal barrier coatings with quasi-columnar structures, Surf. Coating. Technol. 311 (2017) 199–205.

[87] B.P. Zhang, L. Wei, H.B. Guo, H.B. Xu, Microstructures and deposition mechanisms of quasi-columnar structured yttria-stabilized zirconia coatings by plasma spray physical vapor deposition, Ceram. Int. 43 (15) (2017) 12920–12929.

[88] S. Li, W. He, J. Shi, L. Wei, J. He, H. Guo, PS-PVD gadolinium zirconate thermal barrier coatings with columnar microstructure sprayed from sintered powder feedstocks, Surf. Coating. Technol. 383 (August 2019) (2020) 125243.

[89] C. Zhao, W. He, L. Wei, H. Guo, Microstructures of $La_2Ce_2O_7$ coatings produced by plasma spray-physical vapor deposition, J. Eur. Ceram. Soc. 40 (4) (2020) 1462–1470.

[90] C.J. Li, Q.L. Zhang, S.W. Yao, G.J. Yang, C.X. Li, Plasma spraying of dense ceramic coating with fully bonded lamellae through materials design based on the critical bonding temperature concept, J. Therm. Spray Technol. 28 (1–2) (2019) 53–56.

[91] C.-J. Li, G.-J. Yang, C.-X. Li, Development of particle interface bonding in thermal spray coatings: a review, J. Therm. Spray Technol. 22 (2) (2013) 192–206.

[92] C.-J. Li, G.-J. Yang, A. Ohmori, Relationship between particle erosion and lamellar microstructure for plasma-sprayed alumina coatings, Wear 260 (11) (2006) 1166–1172.

[93] L. Chen, G.J. Yang, C.-X. Li, C.-J. Li, Edge effect on crack patterns in thermally sprayed ceramic splats, J. Therm. Spray Technol. 26 (3) (2017) 302–314.

[94] X. Yuan, D. Xiao, T. Luo, S. Lin, A novel strategy for depositing dense self - fluxing alloy coatings with sufficiently bonded splats by one - step atmospheric plasma spraying, J. Therm. Spray Technol. (2019) 123456789.

[95] Y. Tan, V. Srinivasan, T. Nakamura, S. Sampath, P. Bertrand, G. Bertrand, Optimizing compliance and thermal conductivity of plasma sprayed thermal barrier coatings via controlled powders and processing strategies, J. Therm. Spray Technol. 21 (5) (2012) 950–962.

[96] B. Bernard, A. Quet, L. Bianchi, A. Joulia, A. Malié, V. Schick, B. Rémy, Thermal insulation properties of YSZ coatings: suspension plasma spraying (SPS) versus electron beam physical vapor deposition (EB-PVD) and atmospheric plasma spraying (APS), Surf. Coating. Technol. 318 (2017) 122–128.

[97] P. Sokołowski, S. Kozerski, L. Pawłowski, A. Ambroziak, The key process parameters influencing formation of columnar microstructure in suspension plasma sprayed zirconia coatings, Surf. Coating. Technol. 260 (2014) 97–106.

[98] R. Naraparaju, M. Hüttermann, U. Schulz, P. Mechnich, Tailoring the EB-PVD columnar microstructure to mitigate the infiltration of CMAS in 7YSZ thermal barrier coatings, J. Eur. Ceram. Soc. 37 (1) (2017) 261–270.

[99] L. Gao, H. Guo, L. Wei, C. Li, S. Gong, H. Xu, Microstructure and mechanical properties of yttria stabilized zirconia coatings prepared by plasma spray physical vapor deposition, Ceram. Int. 41 (7) (2015) 8305–8311.

[100] Z.Y. Yu, L.L. Wei, X.Y. Guo, B.P. Zhang, Q. He, H.B. Guo, Microstructural evolution, mechanical properties and degradation mechanism of PS-PVD quasi-columnar thermal barrier coatings exposed to glassy CMAS deposits, Rare Met. (2018) 1–12.

[101] T. Yuan, C.G. Deng, J. Mao, C.M. Deng, Z.Q. Deng, Preparation and thermal conductivity of 7ysz thermal barrier coatings prepared by plasma spray-physical vapor deposition, J. Mater. Eng. 45 (7) (2017) 1–6.

[102] Wen Long Cheng, Fabrication and Properties of Feather-like Columnar Structure 7YSZ Thermal Barrier Coatings by PS-PVD, PhD Thesis, Guangdong University of Technology, 2017 (In Chinese).

[103] A. Refke, D. Hawley, J. Doesburg, R. Schmid, LPPS thin film technology for the application of TBC systems, in: Proceedings of the International Thermal Spraying Conference, Basel, 2005.

[104] F. Shao, H. Zhao, X. Zhong, Y. Zhuang, Z. Cheng, L. Wang, et al., Characteristics of thick columnar ysz coatings fabricated by plasma spray-physical vapor deposition, J. Eur. Ceram. Soc. (2017). S0955221917307392.

[105] Q.Y. Chen, Microstructure Control of YSZ Ceramic Coating by Plasma Spray-Physical Vapor Deposition, PhD Thesis, Xi'an Jiaotong University, 2016 (In Chinese).

[106] K. Wang, H. Peng, H. Guo, S. Gong, Effect of sintering on thermal conductivity and thermal barrier effects of thermal barrier coatings, Chin. J. Aeronaut. 25 (5) (2012) 811–816.

[107] H. Guo, S. Gong, K. Aik Khor, H. Xu, Effect of thermal exposure on the microstructure and properties of EB-PVD gradient thermal barrier coatings, Surf. Coating. Technol. 168 (1) (2003) 23–29.

[108] B. Bernard, A. Quet, L. Bianchi, V. Schick, A. Joulia, A. Malié, B. Rémy, Effect of suspension plasma-sprayed YSZ columnar microstructure and bond coat surface preparation on thermal barrier coating properties, J. Therm. Spray Technol. 26 (6) (2017) 1025–1037.

[109] H. Zhang, J. Yuan, W. Song, X. Zhou, S. Dong, S. Duo, J. Wang, X. Yang, J. Jiang, L. Deng, J. Huang, X. Cao, Composition, mechanical properties and thermal cycling performance of YSZ toughened $La_2Ce_2O_7$ composite thermal barrier coatings, Ceram. Int. 46 (5) (2020) 6641–6651.

[110] T. Liu, X. Chen, G.J. Yang, C.J. Li, Properties evolution of plasma-sprayed $La_2Zr_2O_7$ coating induced by pore structure evolution during thermal exposure, Ceram. Int. 42 (14) (2016) 15485–15492.

[111] Sen-Hui Liu, Cheng-Xin Li, Lu Li, Jia-Hu Huang, Pan Xu, G.-J.Y. Ying-Zhen Hu, C.-J. Li, Development of long laminar plasma jet on thermal spraying process: microstructures of zirconia coatings, Surf. Coating. Technol. 337 (2018) 241–249.

[112] A.S.M. Ang, C.C. Berndt, A review of testing methods for thermal spray coatings, Int. Mater. Rev. 59 (4) (2014) 179–223.

[113] L. Wang, Y. Wang, X.G. Sun, J.Q. He, Z.Y. Pan, C.H. Wang, Microstructure and indentation mechanical properties of plasma sprayed nano-bimodal and conventional ZrO_2-8wt%Y_2O_3 thermal barrier coatings, Vacuum 86 (8) (2012) 1174–1185.

[114] R. Vaßen, E. Bakan, D. Mack, S. Schwartz-Lückge, D. Sebold, Y. Jung Sohn, D. Zhou, O. Guillon, Performance of YSZ and $Gd_2Zr_2O_7$/YSZ double layer thermal barrier coatings in burner rig tests, J. Eur. Ceram. Soc. 40 (2) (2020) 480–490.

[115] K.A. Khor, Y.W. Gu, Z.L. Dong, Mechanical behavior of plasma sprayed functionally graded YSZ/NiCoCrAlY composite coatings, Surf. Coating. Technol. 139 (2–3) (2001) 200–206.

[116] F. Azarmi, T. Coyle, J. Mostaghimi, Young's modulus measurement and study of the relationship between mechanical properties and microstructure of air plasma sprayed alloy 625, Surf. Coating. Technol. 203 (8) (2009) 1045–1054.

[117] L. Guo, H.B. Guo, S.K. Gong, H.B. Xu, Improvement on the phase stability, mechanical properties and thermal insulation of Y2O3-stabilized ZrO2 by Gd2O3 and Yb2O3co-doping, Ceram. Int. 39 (8) (2013) 9009–9015.

[118] A. Jadhav, N.P. Padture, F. Wu, E.H. Jordan, M. Gell, Thick ceramic thermal barrier coatings with high durability deposited using solution-precursor plasma spray, Mater. Sci. Eng., A 405 (2005) 313–320.

[119] K. Vanevery, M.J.M. Krane, R.W. Trice, H. Wang, W. Porter, M. Besser, D. Sordelet, J. Ilavsky, J. Almer, Column Formation in Suspension Plasma-Sprayed Coatings and Resultant Thermal Properties, vol. 20, 2011, pp. 817–828. June.

[120] J. Singh, D.E. Wolfe, Nano and macro-structured component fabrication by electron beam-physical vapor deposition (EB-PVD), J. Mater. Sci. 40 (2005) 1–26.

[121] D. Zhou, D.E. Mack, P. Gerald, O. Guillon, R. Vaßen, Architecture designs for extending thermal cycling lifetime of suspension plasma sprayed thermal barrier coatings, Ceram. Int. June (2019), 0–1.

[122] C.O. Laux, T.G. Spence, C.H. Kruger, R.N. Zare, Optical diagnostics of atmospheric pressure air plasmas, Plasma Sources Sci. Technol. 12 (2) (2003) 125–138.

[123] I.H. Hutchinson, Principles of Plasma Diagnostics, Cambridge University Press, 1987, ISBN 9780511613630, https://doi.org/10.1017/CBO9780511613630.

[124] J.W. Coburn, M. Chen, Optical emission spectroscopy of reactive plasmas: a method for correlating emission intensities to reactive particle density, J. Appl. Phys. 51 (6) (1980) 3134–3136.

[125] I.O. Golosnoy, A. Cipitria, T.W. Clyne, Heat transfer through plasma-sprayed thermal barrier coatings in gas turbines: a review of recent work, J. Therm. Spray Technol. 18 (5) (2009) 809–821.

[126] V.A. Nemchinsky, W.S. Severance, What we know and what we do not know about plasma arc cutting, J. Phys. D 39 (22) (2006).

[127] Y.C. Lee, Y.P. Chyou, E. Pfender, Particle dynamics and particle heat and mass transfer in thermal plasmas. Part II. Particle heat and mass transfer in thermal plasmas, Plasma Chem. Plasma Process. 5 (4) (1985) 391–414.

[128] R.C. Allen, W.J. Black, J.A. Mcfarland, Development and diagnosis of an atmospheric pressure plasma torch for investigating magnetohydrodynamic instabilities, J. Phys. Appl. Phys. 15 (17) (2019).

[129] H. Huang, W. Pan, Z. Guo, C. Wu, Instabilities in a Non-transferred Direct Current Plasma Torch Operated at Reduced, 2010, p. 85202.

[130] V. Rat, J.F. Coudert, Analytical interpretation of arc instabilities in a DC plasma spray torch: the role of pressure, J. Phys. Appl. Phys. 49 (23) (2016).

[131] V. Rat, J.F. Coudert, Improvement of plasma spray torch stability by controlling pressure and voltage dynamic coupling, J. Therm. Spray Technol. 20 (1–2) (2011) 28–38.

[132] L. Zhao, M. Maurer, F. Fischer, R. Dicks, E. Lugscheider, Influence of spray parameters on the particle in-flight properties and the properties of HVOF coating of WC-CoCr, Wear 257 (257) (2004) 41–46.

[133] J.R. Fincke, W.D. Swank, R.L. Bewley, D.C. Haggard, M. Gevelber, D. Wroblewski, Diagnostics and control in the thermal spray process, Surf. Coating. Technol. (2001) 537–543.

[134] J. Stanisic, D. Kosikowski, P.S. Mohanty, High-speed visualization and plume characterization of the hybrid spray process, J. Therm. Spray Technol. 15 (4) (2006) 750–758.

[135] L. Zhao, K. Seemann, A. Fischer, E. Lugscheider, Study on atmospheric plasma spraying of Al2O3 using on-line particle monitoring, Surf. Coating. Technol. 168 (2) (2003) 186–190.

[136] M. Vardelle, A. Vardelle, A.C. Leger, P. Fauchais, D. Gobin, Influence of particle parameters at impact on splat formation and solidification in plasma spraying processes, J. Therm. Spray Technol. 4 (1) (1995) 50–58.

[137] S. Sampath, X. Jiang, J. Matejicek, A. Leger, A. Vardelle, Substrate temperature effects on splat formation, microstructure development and properties of plasma sprayed coatings Part I: case study for partially stabilized zirconia, Mater. Sci. Eng. A-Struct. Mater. Prop. Microstruct. Process. 272 (1) (1999) 181–188.

[138] A. Vardelle, P. Fauchais, B. Dussoubs, N.J. Themelis, Heat generation and particle injection IN a thermal plasma torch, Plasma Chem. Plasma Process. 18 (4) (1998) 551–574.

[139] P. Fauchais, A. Vardelle, Heat, mass and momentum transfer in coating formation by plasma spraying, Int. J. Therm. Sci. 39 (2000) 852–870.

[140] A. Vardelle, C. Moreau, N.J. Themelis, C. Chazelas, A perspective on plasma spray technology, Plasma Chem. Plasma Process. 35 (3) (2015) 491–509.

[141] P. Fauchais, M. Vardelle, A. Vardelle, Reliability of plasma-sprayed coatings: monitoring the plasma spray process and improving the quality of coatings, J. Phys. D 46 (22) (2013) 224016.

[142] M. Vardelle, P. Fauchais, A. Vardelle, K.I. Li, B. Dussoubs, N.J. Themelis, Controlling particle injection in plasma spraying, J. Therm. Spray Technol. 10 (2) (2001) 267–284.

[143] E. Pfender, Y.C. Lee, Particle dynamics and particle heat and mass transfer in thermal plasmas. Part I. The motion of a single particle without thermal effects, Plasma Chem. Plasma Process. 5 (3) (1985) 211–237.

[144] M. Brossa, E. Pfender, Probe measurements in thermal plasma jets, Plasma Chem. Plasma Process. 8 (1) (1988) 75–90.

[145] J. Fazilleau, C. Delbos, V. Rat, J.F. Coudert, P. Fauchais, B. Pateyron, Phenomena involved in suspension plasma apraying part 1: suspension injection and behavior, Plasma Chem. Plasma Process. 26 (4) (2006) 371–391.

[146] A.A. Ovsyannikov, M.F. Zhukov, Plasma Diagnostics, Cambridge International Science Publishing, Cambridge CB16AZ, UK, 2005, ISBN 1898326231.

[147] L. Vincenzi, S. Suzuki, D. Outcalt, J. Heberlein, Controlling spray torch fluid dynamics — effect on spray particle and coating characteristics, J. Therm. Spray Technol. 19 (June) (2010) 713–722.
[148] C. Zhang, W. Li, M. Planche, C. Li, H. Liao, Study on gas permeation behavior through atmospheric plasma-sprayed yttria stabilized zirconia coating, Surf. Coating. Technol. 202 (2008) 5055–5061.
[149] V. Debout, et al., Investigation of in-light particle characteristics and Microstructural effects on optical properties of YSZ plasma-sprayed coatings, High Temp. Mater. Process. 11 (2007) 309–320.
[150] G. Mauer, R. Vaßen, D. Stöver, Preliminary study on the TriplexPro TM -200 gun for atmospheric plasma spraying of yttria-stabilized zirconia, Surf. Coating. Technol. 202 (2008) 4374–4381.
[151] G. Mauer, R. Vaßen, D. Stöver, Atmospheric plasma spraying of yttria-stabilized zirconia coatings with specific porosity, Surf. Coating. Technol. 204 (1–2) (2009), 172–1.
[152] W.H. Zhao, K. Tian, H.Z. Tang, D. Liu, G.Z. Zhang, J. Phys. D Appl. Phys. 35 (2002) 2815.
[153] W.X. Pan, X. Meng, C.K. Wu, Plasma Sci. Technol. 8 (2006) 416.
[154] L.T. An, Y. Gao, C. Sun, Effects of anode arc root fluctuation on coating quality during plasma spraying, J. Therm. Spray Technol. 20 (4) (2011) 775–781, https://doi.org/10.1007/s11666-011-9644-y.
[155] S. Janisson, A. Vardelle, J.F. Coudert, P. Fauchais, E. Meillot, Analysis of the stability of dc plasma gun operating with Ar–He–H2, gas mixtures, Ann. N. Y. Acad. Sci. 891 (1) (1999) 407–416.
[156] R. Chidambaram Seshadri, S. Sampath, Characteristics of conventional and cascaded arc plasma spray-deposited ceramic under standard and high-throughput conditions, J. Therm. Spray Technol. 28 (4) (2019) 690–705.
[157] S.-H. Liu, J.P. Trelles, A.B. Murphy, L. Li, S. Zhang, G.-J. Yang, C.-J.C.-X.C. Li, C.-J.C.-X.C. Li, Numerical simulation of the flow characteristics inside a novel plasma spray torch, J. Phys. Appl. Phys. 52 (33) (2019) 335203.
[158] A. Refke, G. Barbezat, Characterization of LPPS processes under various spray conditions for potential applications, in: International Thermal Spray Conference, 2003. May, 5–8.
[159] L. Vincenzi, S. Suzuki, D. Outcalt, J. Heberlein, Controlling spray torch fluid dynamics effect on spray particle and coating characteristics J, Therm. Spray Technol. 19 (2010), 713–22.
[160] C. Zhang, W. Li, M. Planche, C. Li, H. Liao, Study on gas permeation behavior through atmospheric plasma-sprayed yttria stabilized zirconia coating Surf. Coat, Technol. 202 (2008), 5055–61.
[161] V. Debout, A. Vardelle, P. Abelard, P. Fauchais, E. Meillot, E. Bruneton, F. Enguehard, S. Schelz, Investigation of in-light particle characteristics and Microstructural effects on optical properties of YSZ plasma-sprayed coatings High, Temp. Mater. Processes 11 (2007) 309–320.
[162] G. Mauer, R. Vaßen, D. Stöver, Preliminary study on the TriplexPro™–200 gun for atmospheric plasma spraying of yttria-stabilized zirconia Surf. Coat, Technol. 202 (2008), 4374–81.
[163] G. Mauer, R. Vaßen, D. Stöver, Atmospheric plasma spraying of yttria-stabilized zirconia coatings with specific porosity, Surf. Coating. Technol. 204 (2009), 172–9.
[164] E. Turunen, T. Varis, S.P. Hannula, A. Vaidya, A. Kulkarni, J. Gutleber, H. Herman, On the role of particle state and deposition procedure on mechanical, tribological and dielectric response of high velocity oxy-fuel sprayed alumina coatings, Mater. Sci. Eng., A 415 (1–2) (2006) 1–11.
[165] M. Boulos, P. Fauchais, E. Pfender, Thermal Plasmas: Fundamentals and Applications, Springer, Berlin, 1994.
[166] Xi Chen, Heat and Mass Transfer of Thermal Plasma, Science Press, Beijing, 2009.
[167] H. Li, X. Chen, Three-dimensional simulation of a plasma jet with transverse particle and carrier gas injection, Thin Solid Films 390 (2001) 175–180.
[168] K. Cheng, X. Chen, Effects of natural convection on the characteristics of long laminar argon plasma jets issuing upwards or downwards into ambient air—a numerical study, J. Phys. Appl. Phys. 37 (17) (2004) 2385–2391.
[169] D.-Y. Xu, X. Chen, K. Cheng, Three-dimensional modelling of the characteristics of long laminar plasma jets with lateral injection of carrier gas and particulate matter, J. Phys. Appl. Phys. 36 (13) (2003) 1583–1594.
[170] W.T. He, G. Mauer, R. Vaßen, Excitation temperature and constituent concentration profiles of the plasma jet under plasma spray-PVD, Plasma Chem. Plasma Process. 37 (5) (2017) 1293–1311.
[171] W.X. Pan, Z.Y. Guo, X. Meng, H.J. Huang, C.K. Wu, Fluctuation characteristics of arc voltage and jet flow in a non-transferred dc plasma generated at reduced pressure, Plasma Sources Sci. Technol. 18 (4) (2009): 045032.
[172] K. Bobzin, M. Öte, Modeling multi-arc spraying systems, J. Therm. Spray Technol. 25 (5) (2016) 920–932.
[173] R. Bandyopadhyay, P. Nylén, A computational fluid dynamic analysis of gas and particle flow in flame spraying, J. Therm. Spray Technol. 12 (4) (2003) 492–503.
[174] E. Pfender, J. Fincke, R. Spores, Entrainment of cold gas into thermal plasma jets, Plasma Chem. Plasma Process. 11 (4) (1991) 529–543.
[175] E. Pfender, Plasma jet behavior and modeling associated with the plasma spray process, The Solid Films 238 (1994) 228–241.
[176] Li He-Ping, E. Pfender, Three dimensional modeling of the plasma spray process, J. Therm. Spray Technol. 16 (2) (2007) 245–260.
[177] J.P. Trelles, E. Pfender, J.V.R. Heberlein, Thermal nonequilibrium simulation of an arc plasma jet, IEEE Trans. Plasma Sci. 36 (4 PART 1) (2008) 1026–1027.
[178] S. Paik, P.C. Huang, J. Heberleinand, E. Pfender, Determination of the arc-root position in a DC plasma torch, Plasma Chem. Plasma Process. 13 (3) (1993) 379–397.
[179] J. Heberlein, J. Mentel, E. Pfender, The anode region of electric arcs: a survey, J. Phys. D 43 (2) (2010) 23001.
[180] H.-P. Li, E. Pfender, X. Chen, Application of Steenbeck's minimum principle for three-dimensional modelling of DC arc plasma torches, J. Phys. D 36 (9) (2003) 1084–1096.
[181] J.P. Trelles, E. Pfender, J. Heberlein, Multiscale finite element modeling of arc dynamics in a DC plasma torch, Plasma Chem. Plasma Process. 26 (6) (2006) 557–575.
[182] J.P. Trelles, E. Pfender, J.V.R. Heberlein, Modelling of the arc reattachment process in plasma torches, J. Phys. D 40 (18) (2007) 5635–5648.
[183] J.P. Trelles, Computational study of flow dynamics from a dc arc plasma jet, J. Phys. D 46 (25) (2013) 255201.
[184] G. Yang, P. Cronin, J.V. Heberlein, E. Pfender, Experimental investigations of the anode boundary layer in high intensity arcs with cross flow, J. Phys. D 39 (13) (2006) 2764–2774.
[185] J.P. Trelles, C. Chazelas, A. Vardelle, J.V.R. Heberlein, Arc plasma torch modeling, J. Therm. Spray Technol. 18 (5–6) (2009) 728–752.
[186] Z. Duan, J. Heberlein, arc instabilities in a plasma spray torch, J. Therm. Spray Technol. 11 (March) (2002) 44–51.
[187] M.I. Boulos, The role of transport phenomena and modeling in the development of thermal plasma technology, Plasma Chem. Plasma Process. 36 (1) (2016) 3–28.
[188] E. Pfender, Thermal plasma technology: where do we stand and where are we going? Plasma Chem. Plasma Process. 19 (No. 1) (1999) 1–31.
[189] A.B. Murphy, D. Uhrlandt, Foundations of high-pressure thermal plasmas, Plasma Sources Sci. Technol. 27 (6) (2018).
[190] C.H.C. Ramshaw, J. D, Modelling of nonequilibrium effects in a high-velocity nitrogen-hydrogen plasma jet, Plasma Chem. Plasma Process. 16 (I) (1996).
[191] H. Sun, Y. Wu, Y. Tanaka, K. Tomita, Investigation on chemically non-equilibrium arc behaviors of different gas media during arc decay phase in a model circuit breaker, J. Phys. Appl. Phys. 52 (725202) (2019).
[192] M. Baeva, M.S. Benilov, N.A. Almeida, D. Uhrlandt, Novel non-equilibrium modelling of a DC electric arc in argon, J. Phys. Appl. Phys. m (245205) (2016).
[193] M.S. Benilov, Understanding and modelling plasma-electrode interaction in high-pressure arc discharges: a review, J. Phys. Appl. Phys. 41 (14) (2008).
[194] J.P. Trelles, Nonequilibrium phenomena in (quasi -) thermal plasma flows, Plasma Chem. Plasma Process. (2019) 123456789.
[195] M. Baeva, Non-equilibrium modeling of tungsten-inert gas arcs, Plasma Chem. Plasma Process. 37 (2) (2017) 341–370.
[196] V.G. Bhigamudre, J.P. Trelles, Characterization of the arc in crossflow using a two-temperature nonequilibrium plasma flow model, J. Phys. Appl. Phys. 52 (15205) (2019).
[197] B. Pateyron, M.-F. Elchinger, G. Delluc, P. Fauchais, Thermodynamic and Transport Properties of Ar-H ~ and A r - H e Plasma Gases Used for Spraying at Atmospheric Pressure . I: properties of the Mixtures, Plasma Chem. Plasma Process. 12 (4) (1992) 421–448.
[198] J. Xiang, K. Tanaka, F.F. Chen, M. Shigeta, M. Tanaka, A.B. Murphy, Modelling and Measurements of Gas Tungsten Arc Welding in Argon–Helium Mixtures with Metal Vapour, Welding in the World, 2021.
[199] S. Chapman, T.G. Cowling, The Mathematical Theory of Non-uniform Gases, third ed., Cambridge University Press, Cambridge, 1970.
[200] R.S. Devoto, Transport coefficients of partially ionized argon, Phys. Fluid. 10 (1967), 354–64.
[201] K. Onda, Y. Tanaka, K. Akashi, Y. Nakano, T. Ishijima, Y. Uesugi, S. Sueyasu, S. Watanabe, K. Nakamura, Numerical thermofluid simulation on tandem type of induction thermal plasmas with and without current modulation in a lower coil, J. Phys. Appl. Phys. 53 (16) (2020).
[202] A.B. Murphy, Transport coefficients of helium and argon – helium plasmas, IEEE Trans. Plasma Sci. 25 (5) (1997) 809–814.
[203] S.A. Yershin, Paradoxes in Aerohydrodynamics, Springer, Switzerland, 2016.
[204] R. Huang, H. Fukanuma, Y. Uesugi, Y. Tanaka, An improved local thermal equilibrium model of DC arc plasma torch, IEEE Trans. Plasma Sci. 39 (10) (2011) 1974–1982.
[205] ANSYS FLUENT 16.0 User's Guide, https://studentcommunity. ansys.com/thread/fluent-theory-guide-user-guide/.
[206] M.M. Gibson, B.E. Launder, Ground effects on pressure fluctuations in the atmospheric boundary layer, J. Fluid Mech. 86 (1978) 491–511.
[207] B.E. Launder, G.J. Reece, W. Rodi, Progress in the development of a Reynolds-stress turbulence closure, J. Fluid Mech. 68 (3) (April 1975) 537–566.
[208] V. Bianco, A. Khait, A. Noskov, V. Alekhin, A comparison of the application of RSM and LES turbulence models in the numerical simulation of thermal and flow patterns in a double-circuit Ranque-Hilsch vortex tube, Appl. Therm. Eng. 106 (2016) 1244–1256.
[209] Q. Zhou, H. Li, X. Xu, F. Liu, S. Guo, X. Chang, P. Xu, Comparative study of turbulence models on highly constricted plasma cutting arc, J. Phys. D 42 (1) (2009) 15210.
[210] A. Gleizes, J.J. Gonzalez, P. Freton, Thermal plasma modelling J, Phys. D: Appl. Phys. 38 (2005). R153–83.
[211] Q. Zhou, H. Yin, H. Li, X. Xu, F. Liu, S. Guo, P. Xu, Comparative study of turbulence models on highly constricted plasma cutting arc, J. Phys. D Appl. Phys. 42 (2009) 95208.
[212] Z. Guo, S. Yin, H. Liao, S. Gu, Three-dimensional simulation of an

argon—hydrogen DC non-transferred arc plasma torch Int, J. Heat Mass Transfer 80 (2015), 644–52.
[213] T. Zhang, Y. Bao, D.T. Gawne, B. Liu, J. Karwattzki, Computer model to simulate the random behaviour of particles in a thermal-spray jet, Surf. Coating. Technol. 201 (2006) 3552–3563.
[214] K. Bobzin, M. Öte, M.A. Knoch, I. Alkhasli, Macroscopic particle modeling in air plasma spraying, Surf. Coating. Technol. (December 2017) (2018) 1–8.
[215] E. Pfender, Y.C. Lee, Particle dynamics and particle heat and mass transfer in thermal plasmas. Part I. The motion of a single particle without thermal effects, Plasma Chem. Plasma Process. 5 (3) (1985) 211–237.
[216] Xi Chen, Heat Transfer and Fluid Flow under Thermal Plasma Conditions, chapters vols. 4 and 5, Science Press, Beijing, 1993 (in Chinese).
[217] R. Westhoff, G. Trapaga, J. Szekely, Plasma-particle interactions in plasma spraying systems, Metallur. Trans. B 23 (6) (1992) 683–693.
[218] J.J. Tian, S.W. Yao, S.L. Zhang, C.J. Li, Effect of the shell-core-structured particle design on the heating characteristic of nickel-based alloy particle during plasma spraying, Surf. Coating. Technol. 335 (December 2017) (2018) 52–61.
[219] P. Fauchais, Understanding plasma spraying, J. Phys. Appl. Phys. 37 (9) (2004).
[220] H. Zhang, A. Vardelle, N.J. Themelis, J. High Temp. Mater. Process 3 (2003), 277–98.
[221] L. Pawlowski, Suspension and solution thermal spray coatings, Surf. Coating. Technol. 203 (19) (2009) 2807–2829.
[222] H.P. Li, X. Chen, Three-dimensional modeling of the turbulent plasma jet impinging upon a flat plate and with transverse particle and carrier-gas injection, Plasma Chem. Plasma Process. 22 (1) (2002).
[223] Y.P. Wan, V. Prasad, G.-X. Wang, S. Sampath, J.R. Fincke, Model and powder particle heating, melting, resolidification and vaporization in plasma spraying processes, J. Heat Tran. 121 (1999) 691–699.
[224] X. Chen, E. Pfender, Behavior of small particles in a thermal plasma flow, Plasma Chem. Plasma Process. 3 (1983) 351.
[225] E.P. Xi Chen, Effect of the Knudsen number on heat transfer to a particle immersed into a thermal plasma, Plasma Chem. Plasma Process. 3 (I) (1983).
[226] A.B. Liu, D. Mather, R.D. Reitz, Modeling the Effects of Drop Drag and Breakup on Fuel Sprays. SAE Technical Paper 930072, SAE, 1993.
[227] R.D. Reitz, Mechanisms of atomization processes in high-pressure vaporizing sprays, Atomization Spray Technol. 3 (1987) 309–337.
[228] J.H. Ferziger, M. Peric, Computational Methods for Fluid Dynamics, Springer, Berlin, 2002, p. 423, https://doi.org/10.1007/978-3-642-56026-2.
[229] F.M. White, Viscous Fluid Flow, third ed., McGrawHill, New York, 2005.
[230] F.P. Incropera, D.P. Dewitt, T.L. Bergman, A.S. Lavine, Fundamentals of Heat and Mass Transfer, sixth ed., John Wiley, New York, 2007.
[231] G.A. Hughmark, Mass and heat transfer from rigid spheres, AIChE J. 13 (6) (1967) 1219–1221.
[232] K. Bobzin, M. Öte, M.A. Knoch, I. Alkhasli, Macroscopic particle modeling in air plasma spraying, Surf. Coating. Technol. July (2018) 1–8.
[233] A. Vardelle, P. Fauchais, B. Dussoubs, N.J. Themelis, Heat generation and particle injection in a thermal plasma torch, Plasma Chem. Plasma Process. 18 (4) (1998) 551–574.
[234] H. Xiong, L. Zheng, S. Sampath, R.L. Williamson, J.R. Fincke, Three-dimensional simulation of plasma spray : effects of carrier gas flow and particle injection on plasma jet and entrained particle behavior, Int. J. Heat Mass Tran. 47 (2004) 5189–5200.
[235] G.M. Faeth, Vaporization and combustion of sprays, Progress Energy Combust. Sci. Set. 9 (1983) 1–76.
[236] Xi Chen, X. Chen, Drag on a metallic or nonmetallic particle exposed to a rarefied plasma flow, Plasma Chem. Plasma Process. 9 (1989) 387–408.
[237] M. Vardelle, C. Trassy, A. Vardelle, P. Fauchais, Experimental investigation of powder vaporization in thermal plasma jets, Plasma Chem. Plasma Process. 11 (2) (1991) 185–201.
[238] M.J. Liu, M. Zhang, Q. Zhang, G.J. Yang, C.X. Li, C.J. Li, Evaporation of droplets in plasma spray–physical vapor deposition based on energy compensation between self-cooling and plasma heat transfer, J. Therm. Spray Technol. 26 (7) (2017) 1641–1650.
[239] R. Westhoff, G. Trapaga, J. Szekely, Plasma-particle interactions in plasma spraying systems, Metallur. Trans. B 23 (6) (1992) 683–693.
[240] A. Vardelle, N.J. Themelis, B. Dussoubs, M. Vardelle, P. Fauchais, Transport and chemical rate phenomena in plasma sprays, High Temp. Mater. Process. 1 (3) (1997) 295–313.
[241] Y.P. Wan, J.R. Fincke, S. Sampath, V. Prasad, H. Herman, Modeling and experimental observation of vaporization from oxidizing molybdenum particles entrained in a thermal plasma jet, Int. J. Heat Mass Tran. 45 (2002) 1007–1015.
[242] ANSYS FLUENT 12.0 UDF Manual, Copyrighted by ANSYS. Inc.
[243] J.P. Trelles, J.V.R. Heberlein, E. Pfender, Non- equilibrium modelling of arc plasma torches J. Phys, D (Dallas, 1978): Appl. Phys. 40 (2007), 5937–52.
[244] P. Han, Numerical and Experimental Studies on the Characteristics of D.C. Arc Plasma Torches and Jets, Ph.D. Thesis, Tsinghua University, Beijing, China, 1999 (in Chinese).
[245] Help Online - Origin Help - GaussAmp https://www.originlab.com/doc/Origin-Help/GaussAmp-FitFunc.
[246] P. Han, X. Chen, Modeling of the subsonic-supersonic flow and heat transfer in a DC arc plasma torch, Plasma Chem. Plasma Process. 21 (2) (2001) 249–264.
[247] P. Han, X. Chen, Modeling of the supersonic argon plasma jet at low gas pressure environment, Thin Solid Films 390 (1–2) (2001) 181–185.
[248] G. Mauer, Plasma characteristics and plasma-feedstock interaction under PS-PVD process conditions, Plasma Chem. Plasma Process. 34 (5) (2014) 1171–1186.
[249] B. Vautherin, M.P. Planche, R. Bolot, A. Quet, L. Bianchi, G. Montavon, Vapors and droplets mixture deposition of metallic coatings by very low-pressure plasma spraying, J. Therm. Spray Technol. 23 (4) (2014) 596–608.
[250] X. C, M. Liu, G.F. Xu, et al., Numerical simulation for heat transfer and flow of plasma in LPPS, China Surf. Eng. 28 (5) (2015) 57–63 (In Chinese).
[251] A. Anwaar, L. Wei, H. Guo, B. Zhang, Plasma–powder feedstock interaction during plasma spray–physical vapor deposition, J. Therm. Spray Technol. 26 (3) (2017) 292–301.
[252] D. Ivchenko, G.M. Tao Zhang, A. Vardelle, S. Goutier, T.E. Itina, On the validity of continuum computational fluid dynamics approach under very low-pressure plasma spray conditions, J. Therm. Spray Technol. 27 (2018) 3–13.
[253] D. Ivchenko, G. Mariaux, A. Vardelle, S. Goutier, T.E. Itina, P. André, Feasibility study of an adaptive-pressure plasma coating process—Part 1: model description, J. Therm. Spray Technol. 29 (1–2) (2020) 25–37.
[254] M.J. Liu, K. Zhang, Q. Zhang, M. Zhang, G. Yang, C. Li, Thermodynamic conditions for cluster formation in supersaturated boundary layer during plasma spray-physical vapor deposition, Appl. Surf. Sci. 471 (March 2018) (2019) 950–959.
[255] M.J. Liu, M. Zhang, X. Zhang, G. Li, Q. Zhang, Transport and deposition behaviors of vapor coating materials in plasma spray-physical vapor deposition, Appl. Surf. Sci. 486 (December 2018) (2019) 80–92.
[256] Mei Jun Liu, Jun Yang Guan, Condensation behavior of gaseous phase during transported in the near-substrate boundary layer of plasma spray-physical vapor deposition, J. Mater. Sci. Technol. July 24 (2020).
[257] T. Zhang, X. Luo, C. Li, Numerical simulation of DC argon-hydrogen plasma jet characteristics under very low-pressure plasma spray conditions, Coatings 11 (726) (2021).
[258] I. Barin, O. Knacke, Thermochemical Properties of Inorganic Substances, Springer, Supplement, Berlin, 1997.
[259] D. Ye, J. Hu, The Manual of Practical Inorganic Thermodynamics, Metallurgical Industry Press, Beijing, 2002 (in Chinese).
[260] E. Nogues, M. Vardelle, P. Fauchais, P. Granger, Surf. Coating. Technol. 202 (18) (2008) 4387–4393.
[261] H.B. Guo, R. Vaßen, D. Stöver, Atmospheric plasma sprayed thick thermal barrier coatings with high segmentation crack density, Surf. Coating. Technol. 186 (3) (2004) 353–363.
[262] Sen-Hui Liu, Gang Ji, Chang-Jiu Li, H.-B.G. Cheng-Xin Li, Novel long laminar plasma sprayed hybrid structure thermal barrier coatings for high-temperature anti-sintering and volcanic ash corrosion resistance, J. Mater. Sci. Technol. 79 (5) (2021) 141–146.
[263] D. Zhou, H. Peng, L. Zhu, H. Guo, S. Gong, Microstructure, hardness and corrosion behaviour of Ti/TiN multilayer coatings produced by plasma activated EB-PVD, Surf. Coating. Technol. 258 (2014) 102–107.
[264] J. He, H. Guo, H. Peng, S. Gong, Microstructural, mechanical and oxidation features of NiCoCrAlY coating produced by plasma activated EB-PVD, Appl. Surf. Sci. 274 (2013) 144–150.
[265] V.E. de M.L. da S. Pereira, J.R. Nicholls, R. Newton, Modelling the EB-PVD thermal barrier coating process: component clusters and shadow masks, Surf. Coating. Technol. 311 (2017) 307–313.
[266] U. Schulz, Phase transformation in EB-PVD yttria partially stabilized zirconia thermal barrier coatings during annealing, J. Am. Ceram. Soc. 83 (4) (2004) 904–910.
[267] H. Guo, L. Sun, H. Li, S. Gong, High temperature oxidation behavior of hafnium modified NiAl bond coat in EB-PVD thermal barrier coating system, Thin Solid Films 516 (16) (2008) 5732–5735.
[268] T.M. Rodgers, H. Zhao, H.N.G. Wadley, Vapor deposition on doublet airfoil substrates: control of coating thickness and microstructure, J. Vac. Sci. Technol.: Vacuum, Surfaces Films 33 (6) (2015) 61518.
[269] X.W. Zhou, H.N.G. Wadley, The low energy ion assisted control of interfacial structure: ion incident angle effects, Surf. Sci. 487 (1–3) (2001) 159–170.
[270] J. Cho, S.G. Terry, R. LeSar, C.G. Levi, A kinetic Monte Carlo simulation of film growth by physical vapor deposition on rotating substrates, Mater. Sci. Eng. 391 (1–2) (2005) 390–401.
[271] P. Wang, W. He, G. Mauer, R. Mücke, R. Vaßen, Monte Carlo simulation of column growth in plasma spray physical vapor deposition process, Surf. Coating. Technol. 335 (December 2017) (2018) 188–197.
[272] M. Yoshiya, K. Wada, B.K. Jang, H. Matsubara, Computer simulation of nanopore formation in EB-PVD thermal barrier coatings, Surf. Coating. Technol. 187 (2–3) (2004) 399–407.
[273] B.A. Movchan, Inorganic materials and coatings produced by EBPVD, Surf. Eng. 22 (1) (2006) 35–46.
[274] P.L. Fauchais, J.V.R. Heberlein, M.I. Boulos, Thermal Spray Fundamentals: from Powder to part.. Springer Science+Business Media, Springer, New York, 2014, https://doi.org/10.1007/978-0-387-68991-3.
[275] E.H. Jordan, C. Jiang, M. Gell, The solution precursor plasma spray (SPPS) Process : a review with energy considerations, J. Therm. Spray Technol. 24 (7) (2015) 1153–1165.
[276] P. Sokołowski, et al., The microstructural studies of suspension plasma sprayed zirconia coatings with the use of high-energy plasma torches, Surf. Coating. Technol. 318 (2017) 250–261.

[277] P.L. Fauchais, J.V.R. Heberlein, M.I. Boulos, Thermal Spray Fundamentals: from Powder to part.. Springer Science+Business Media, Springer, New York, 2014, https://doi.org/10.1007/978-0-387-68991-3.
[278] E.H. Jordan, C. Jiang, M. Gell, The solution precursor plasma spray (SPPS) process: a review with energy considerations, J. Therm. Spray Technol. 24 (7) (2015) 1153–1165.
[279] P. Sokołowski, et al., The microstructural studies of suspension plasma sprayed zirconia coatings with the use of high-energy plasma torches, Surf. Coating. Technol. 318 (2017) 250–261.
[280] N. Nikolopoulos, A. Theodorakakos, G. Bergeles, A numerical investigation of the evaporation process of a liquid droplet impinging onto a hot substrate, Int. J. Heat Mass Tran. 50 (1–2) (2007) 303–319.
[281] B. Cai, X. Tuo, Z. Song, Y. Zheng, H. Gu, H. Wang, Modeling of spray flash evaporation based on droplet analysis, Appl. Therm. Eng. 130 (2018) 1044–1051.
[282] C. Price, A. Hamzehloo, P. Aleiferis, D. Richardson, Numerical modelling of droplet breakup for flash-boiling fuel spray predictions, Int. J. Multiphas. Flow 125 (2020).
[283] W. Gao, Q. Qi, J. Zhang, G. Chen, D. Wu, An experimental study on explosive boiling of superheated droplets in vacuum spray flash evaporation, Int. J. Heat Mass Tran. 144 (2019).
[284] P. Yin, S. Yang, X. Li, M. Xu, Numerical simulation of in-nozzle flow characteristics under flash boiling conditions, Int. J. Multiphas. Flow 127 (2020).
[285] F. Fathinia, M. Khiadani, Y.M. Al-Abdeli, A. Shafieian, Performance improvement of spray flash evaporation desalination systems using multiple nozzle arrangement, Appl. Therm. Eng. 163 (September) (2019).
[286] G.V. Kuznetsov, M.V. Piskunov, P.A. Strizhak, Evaporation, boiling and explosive breakup of heterogeneous droplet in a high-temperature gas, Int. J. Heat Mass Tran. 92 (2016) 360–369.
[287] E. Hahne, G. Barthau, Evaporation waves in flashing processes, Int. J. Multiphas. Flow 26 (4) (2000) 531–547.
[288] V. Kulkarni, D. Sivakumar, C. Oommen, T.J. Tharakan, Liquid sheet breakup in gas-centered swirl coaxial atomizers, J. Fluids Eng. Trans. ASME 132 (1) (2010) 113031–113037.
[289] E. Sher, T. Bar-Kohany, A. Rashkovan, Flash-boiling atomization, Prog. Energy Combust. Sci. 34 (4) (2008) 417–439.
[290] C. Wang, R. Xu, Y. Song, P. Jiang, Study on water droplet flash vaporization in vacuum spray cooling, Int. J. Heat Mass Tran. 112 (2017) 279–288.
[291]] Evaporation| Definition & Facts | Britannica https://www.britannica.com/science/evaporation.
[292] Vaporization|meaning in the Cambridge English Dictionary https://dictionary.cambridge.org/dictionary/english/vaporization.
[293] E. Sher, T. Bar-Kohany, A. Rashkovan, Flash-boiling atomization, Prog. Energy Combust. Sci. 34 (4) (2008) 417–439.
[294] Y. Wang, L. Bourouiba, Unsteady sheet fragmentation: droplet sizes and speeds, J. Fluid Mech. 848 (2018) 946–967.
[295] L. Qian, H. Cong, C. Zhu, A numerical investigation on the collision behavior of polymer droplets, Polymers 12 (2) (2020).
[296] V. Guichet, S. Almahmoud, H. Jouhara, Nucleate pool boiling heat transfer in wickless heat pipes (two-phase closed thermosyphons): a critical review of correlations, Therm. Sci. Eng. Progress 13 (July) (2019).
[297] C.L. Ng, R. Sankarakrishnan, K.A. Sallam, Bag breakup of nonturbulent liquid jets in crossflow, Int. J. Multiphas. Flow 34 (3) (2008) 241–259.
[298] A. Hosseini Araghi, M. Khiadani, M.H. Sadafi, K. Hooman, A numerical model and experimental verification for analysing a new vacuum spray flash desalinator utilising low grade energy, Desalination 413 (2017) 109–118.
[299] K.G. Lyras, S. Dembele, J.X. Wen, Numerical simulation of flashing jets atomisation using a unified approach, Int. J. Multiphas. Flow 113 (2019) 45–58.
[300] J. Wen, Y. Hu, A. Nakanishi, R. Kurose, Atomization and evaporation process of liquid fuel jets in crossflows: a numerical study using Eulerian/Lagrangian method, Int. J. Multiphas. Flow 129 (2020) 103331.
[301] A. Günther, K.E. Wirth, Evaporation phenomena in superheated atomization and its impact on the generated spray, Int. J. Heat Mass Tran. 64 (2013) 952–965.
[302] A. Mansour, N. Müller, A review of flash evaporation phenomena and resulting shock waves, Exp. Therm. Fluid Sci. 107 (May) (2019) 146–168.
[303] S. Mutair, Y. Ikegami, Experimental study on flash evaporation from superheated water jets: influencing factors and formulation of correlation, Int. J. Heat Mass Tran. 52 (23–24) (2009) 5643–5651.
[304] H. Kim, J. Song, Jet breakup behavior of liquid carbon dioxide for coal transport applications, Exp. Therm. Fluid Sci. 105 (May 2018) (2019) 349–355.
[305] A.E. Saufi, R. Calabria, F. Chiariello, A. Frassoldati, A. Cuoci, T. Faravelli, P. Massoli, An experimental and CFD modeling study of suspended droplets evaporation in buoyancy driven convection, Chem. Eng. J. 375 (June) (2019).
[306] S.Y. Misyura, G.V. Kuznetsov, R.S. Volkov, V.S. Morozov, Droplet evaporation on a structured surface: the role of near wall vortexes in heat and mass transfer, Int. J. Heat Mass Tran. 148 (2020).
[307] C.K. Wemp, V.P. Carey, Heat transport for evaporating droplets on superhydrophilic, thin, nanoporous layers, Int. J. Heat Mass Tran. 132 (2019) 34–51.
[308] D. Yildiz, Dynamics of Two-phase Flashing Jets. VKI Lectures Series, von-Karman Institute for Fluid Dynamic, Belgium, 2003.
[309] T. Li, X. Dong, D.L.S. Hung, X. Li, M. Xu, Analysis of evaporation characteristics and heat transfer for flash-boiling sprays, Int. J. Heat Mass Tran. 127 (2018) 244–254.
[310] J.J. Yan, D. Zhang, W. Deng, Y.L. Guo, Experiment investigation of the instantaneous mass transfer coefficient at steam-liquid interface during water film flash evaporation in closed chamber, J. Xi'an Jiaot. Univ. 42 (5) (2008) 515–519 (in Chinese).
[311] W.L. Cheng, H. Chen, L. Hu, W.W. Zhang, Effect of droplet flash evaporation on vacuum flash evaporation cooling: Modeling, Int. J. Heat Mass Tran. 84 (2015) 149–157.
[312] P. O'Rourke, Collective Drop Effects on Vaporizing Liquid Sprays, PhD Thesis, Princeton NJ University, 1982.
[313] G.M. Faeth, L.P. Hs, K.W. P, Structure and breakup properties of sprays, Int. J. Multiphas. Flow 21 (1995) 99–127.
[314] L. Opfer, I.V. Roisman, J. Venzmer, M. Klostermann, C. Tropea, Droplet-air collision dynamics: evolution of the film thickness, Phys. Rev. 89 (1) (2014) 1–6.
[315] G. Polanco, A.E. Holdø, G. Munday, General review of flashing jet studies, J. Hazard Mater. 173 (1–3) (2010) 2–18.
[316] X. Chen, D. Ma, V. Yang, S. Popinet, High-fidelity simulations of impinging jet atomization, Atomization Sprays 23 (12) (2013) 1079–1101.
[317] R. Reitz, Computer Modeling of Sprays. Spray Technology Short Course, Pittsburgh, PA, vols. 1–11, 1996. Retrieved from, http://www.erc.wisc.edu/documents/Short_course_1.pdf.
[318] M. Wang, M. Broumand, M. Birouk, Liquid jet trajectory in a subsonic gaseous cross-flow: an analysis of published correlations, Atomization Sprays (2016).
[319] C. Wang, R. Xu, Y. Song, P. Jiang, Study on water droplet flash evaporation in vacuum spray cooling, Int. J. Heat Mass Tran. 112 (2017) 279–288.
[320] M. Eslamian, A. Amighi, N. Ashgriz, Atomization of liquid jet in high-pressure and high-temperature subsonic crossflow, AIAA J. 52 (2014) 1374–1385.
[321] C. Wang, S. Chang, H. Wu, J. Xu, Modeling of drop breakup in the bag breakup regime, Appl. Phys. Lett. 104 (15) (2014) 1–6.
[322] D.D. Loureiro, J. Reutzsch, A. Kronenburg, B. Weigand, K. Vogiatzaki, Primary breakup regimes for cryogenic flash atomization, Int. J. Multiphas. Flow 132 (2020) 103405.
[323] F. Fathinia, M. Khiadani, Y.M. Al-Abdeli, A. Shafieian, Performance improvement of spray flash vaporization desalination systems using multiple nozzle arrangement, Appl. Therm. Eng. 163 (September) (2019).
[324] ANSYS Inc, ANSYS FLUENT Theory Guide, 2009. USA.
[325] H. Zhang, X.Y. Wang, L.L. Zheng, X.Y. Jiang, Studies of splat morphology and rapid solidification during thermal spraying, Int. J. Heat Mass Tran. 44 (24) (2001) 4579–4592.
[326] D. Zhang, L. Zheng, X. Hu, H. Zhang, Numerical studies of arc plasma generation in single cathode and three-cathode plasma torch and its impact on plasma spraying, Int. J. Heat Mass Tran. 98 (2016) 508–522.
[327] S. Basu, E.H. Jordan, B.M. Cetegen, Fluid mechanics and heat transfer of liquid precursor droplets injected into high-temperature plasmas, J. Therm. Spray Technol. 17 (1) (2008) 60–72.
[328] P. Fauchais, A. Vardelle, Solution and suspension plasma spraying of nanostructure coatings, Adv. Plasma Spray Appl. (2012) 149–188.
[329] J.A. Thornton, Influence of apparatus geometry and deposition conditions on structure and topography of thick sputtered coatings, J. Vac. Sci. Technol. 11 (4) (1974) 666–670.
[330] J.A. Venables, R. Article, J.A. Venables, G.D.T. Spiller, M. H, G.D.T. Spiller, M. Hanbucken, Nucleation and growth of thin films, Rep. Progress Phys. Rev. 47 (4) (1984) 399–459.
[331] G. Mauer, A. Hospach, R. Vaßen, Process development and coating characteristics of plasma spray-PVD, Surf. Coating. Technol. 220 (2013) 219–224.
[332] L.H. Gao, L. Wei, H.B. Guo, S. Gong, H. Xu, Deposition mechanisms of yttria-stabilized zirconia coatings during plasma spray physical vapor deposition, Ceram. Int. 42 (4) (2016) 5530–5536.
[333] X.F. Zhang, K.S. Zhou, C.M. Deng, M. Liu, Z.Q. Deng, C.G. Deng, J.B. Song, Gas-deposition mechanisms of 7YSZ coating based on plasma spray-physical vapor deposition, J. Eur. Ceram. Soc. 36 (3) (2016) 697–703.
[334] M.J. Liu, M. Zhang, Q. Zhang, G.J. Yang, C.X. Li, C.J. Li, Gaseous material capacity of open plasma jet in plasma spray-physical vapor deposition process, Appl. Surf. Sci. 428 (2018) 877–884.
[335] M. Liu, Cross-Domain Transport Mechanism of Materials and Integrated Control of Parameter-Group during Plasma Spray–Physical Vapor Deposition, PhD Thesis, Xi'an Jiaotong University, 2018.
[336] M. Liu, G. Zhang, Y. Lu, J. Han, G. Li, Plasma Spray – Physical Vapor Deposition toward Advanced Thermal Barrier Coatings: a Review, Rare Metals, 2020.
[337] Theodore L. Bergman, Adrienne S. Lavine, Frank P. Incropera, Fundamentals of Heat and Mass Transfer, seventh ed., John Wiley & Sons, Incorporated, 2011, ISBN 9781118137253.
[338] M. White Frank, Fluid Mechanics, seventh ed., McGraw-Hill Education, February, 2010, ISBN 978-0077422417.
[339] E. Todreas Neil, S. Kazimi Mujid, Nuclear Systems Volume I: Thermal Hydraulic Fundamentals, second ed., CRC Press, 2012, ISBN 978-0415802871.
[340] Schlichting Herrmann, Gersten Klaus, Boundary-Layer Theory, Springer-Verlag Berlin Heidelberg, 2000, ISBN 978-3-540-66270-9.
[341] L.F. Fan, Z.J. Wu, Z. Wan, J.W. Gao, Experimental investigation of thermal effects on dynamic behavior of granite, Appl. Therm. Eng. 125 (2017) 94–103.

[342] C. Zhao, W. He, J. Shi, Q. Guo, J. Li, H. Guo, Deposition mechanisms of columnar structured $La_2Ce_2O_7$ coatings via plasma spray-PVD, Ceram. Int. 46 (9) (2020) 13424–13432.
[343] W. He, G. Mauer, Y.J. Sohn, A. Schwedt, O. Guillon, R. Vaßen, Investigation on growth mechanisms of columnar structured YSZ coatings in Plasma Spray-Physical Vapor Deposition (PS-PVD), J. Eur. Ceram. Soc. 39 (10) (2019) 3129–3138.
[344] J.A. Thornton, Influence of apparatus geometry and deposition conditions on structure and topography of thick sputtered coatings, J. Vac. Sci. Technol. 11 (4) (1974) 666–670.
[345] G. Mauer, A. Hospach, R. Vaßen, Process development and coating characteristics of plasma spray-PVD, Surf. Coating. Technol. 220 (2013) 219–224.
[346] S.L. Girshick, Particle nucleation and growth in dusty plasmas: on the importance of charged-neutral interactions, J. Vac. Sci. Technol. (38) (2020): 011001.
[347] G. Do Lee, C.Z. Wang, E. Yoon, N.M. Hwang, D.Y. Kim, K.M. Ho, Diffusion, coalescence, and reconstruction of vacancy defects in graphene layers, Phys. Rev. Lett. 95 (20) (2005) 1–4.
[348] T.A. Witten, L.M. Sander, Phys. Rev. Lett. 47 (1981) 1400–1403.
[349] Enge Wang, Atomic-scale study of kinetics in film growth I, Prog. Phys. 23 (2) (2003) (In Chinese).
[350] J. Wen, C. Song, T. Liu, Z. Deng, S. Niu, Y. Zhang, Fabrication of dense gadolinia-doped ceria coatings via very-low-pressure plasma spray and plasma spray–physical vapor deposition process, Coatings 9 (717) (2019).
[351] O. Racek, The effect of HVOF particle-substrate interactions on local variations in the coating microstructure and the corrosion resistance, J. Therm. Spray Technol. 19 (5) (2010) 841–851.
[352] J. Madejski, Solidification of droplets on a cold surface, Int. J. Heat Mass Tran. (1975) 191009–191013.
[353] M. Vardelle, A. Vardelle, A.C. Leger, P. Fauchais, D. Gobin, Influence of particle parameters at impact on splat formation and solidification in plasma spraying processes, J. Therm. Spray Technol. 4 (1) (1995) 50–58.
[354] J.P. Delplanque, R.H. Rangel, An improved model for droplet solidification on a flat surface, J. Mater. Sci. 32 (1997) 1519–1530.
[355] J.B. Robins, Thin film nucleation and growth Kinetics, Appl. Surf. Sci. 34 (1988) 379–394.
[356] L. Wang, P. Clancy, Kinetic Monte Carlo simulation of the growth of polycrystalline Cu films, in: Surface Science, vol. 473, 2001, pp. 25–38. Issues 1–2.
[357] G. Sitja, R. Omar Uñac, C.R. Henry, Kinetic Monte Carlo simulation of the growth of metal clusters on regular array of defects on insulator, Surf. Sci. 604 (3–4) (2010) 404–408.
[358] J.J. Quan, X.W. Zhou, H.N.G.G. Wadley, Atomic assembly of metal surfaces and interfaces, Surf. Sci. 600 (19) (2006) 4537–4547.
[359] Y.L. Lee, J.R. Maa, Nucleation and growth of condensate clusters on solid surfaces, Int. J. Heat Mass Tran. 27 (5) (2000) 705–717.
[360] D.M. Mattox, Handbook of Physical Vapor Deposition (PVD) Processing, Elsevier Inc. MA 01803, USA, 2010, ISBN 978-0-81-552037-5.
[361] L.H. Chen, C.Y. Chen, Y.L. Lee, Nucleation and growth of clusters in the process of vapor deposition, Surf. Sci. 429 (1) (1999) 150–160.
[362] J.A. Venables, Rate equation approaches to thin film nucleation kinetics, Phil. Mag. 27 (Issue 3) (1973).
[363] J.A. Venables, Rate equation approaches to thin film nucleation kinetics, Phil. Mag. 27 (Issue 3) (1973).
[364] G. Hu, J. Huang, G. Orkoulas, P.D. Christofides, Investigation of film surface roughness and porosity dependence on lattice size in a porous thin film deposition process, Phys. Rev. 80 (4) (2009) 1–12.
[365] J. Wen, C. Song, T. Liu, Z. Deng, S. Niu, Y. Zhang, Fabrication of dense gadolinia-doped ceria coatings via very-low-pressure plasma spray and plasma spray–physical vapor deposition process, Coatings 9 (717) (2019).
[366] O. Racek, The effect of HVOF particle-substrate interactions on local variations in the coating microstructure and the corrosion resistance, J. Therm. Spray Technol. 19 (5) (2010) 841–851.
[367] J.B. Robins, Thin film nucleation and growth Kinetics, Appl. Surf. Sci. 34 (1988) 379–394.
[368] T. Fujimoto, K. Okuyama, S. Yamada, M. Adachi, Effect of cluster/particle deposition on atmospheric pressure chemical vapor deposition of SiO2 from four gaseous organic Si-containing precursors and ozone, J. Appl. Phys. 85 (8 I) (1999) 4196–4206.
[369] J.A. Venables, Nucleation and growth processes in thin film formation, J. Vac. Sci. Technol. B: Microelectron. Nanometer Struct. 4 (4) (1986) 870.
[370] N.I. Medvedeva, V.P. Zhukov, M.Y. Khodos, V.A. Gubanov, The electronic structure and cohesive energy of HfO_2, ZrO_2, TiO_2, and SnO_2 crystals, Physica Status Solidi B-Basic Solid Stat. Phys. 160 (2) (1990) 517–527.
[371] F.J. Keneshea, D.L. Douglass, The diffusion of oxygen in Zirconia as a function of oxygen pressure, Oxid. Metals 3 (1) (1971) 1–14.
[372] K. Park, D.R. Olander, Oxygen diffusion in single-crystal tetragonal zirconia, J. Electrochem. Soc. 138 (4) (1991) 1154–1159.
[373] A.M.J. VMayo, Zr surface diffusion in tetragonal yttria stabilized zirconia, J. Mater. Sci. 35 (2) (2000) 437–442, https://doi.org/10.1023/A:1004771418188.
[374] S. Swaroop, M. Kilo, C. Argirusis, G. Borchardt, A.H. Chokshi, Lattice and grain boundary diffusion of cations in 3YTZ analyzed using SIMS, Acta Mater. 53 (19) (2005) 4975–4985.
[375] T. Nakagawa, I. Sakaguchi, N. Shibata, K. Matsunaga, T. Yamamoto, H. Haneda, Y. Ikuhara, Oxygen diffusion blocking of single grain boundary in yttria-doped zirconia bicrystals, J. Mater. Sci. 40 (12) (2005) 3185–3190.
[376] S. Ghosh, S. Swaroop, P. Fielitz, G. Borchardt, A.H. Chokshi, Influence of grain boundary sliding on diffusion in yttria doped zirconia, J. Eur. Ceram. Soc. 31 (6) (2011) 1027–1032.
[377] J. Pelleg, Diffusion in ceramics, in: Ceramics Science and Technology, vols. 1–4, 2013, pp. p301–p421.
[378] H. Shin, A. Benali, Y. Luo, E. Crabb, A. Lopez-Bezanilla, L.E. Ratcliff, A.M. Jokisaari, O. Heinonen, Zirconia and hafnia polymorphs: ground-state structural properties from diffusion Monte Carlo, Phys. Rev. Mater. 2 (7) (2018).
[379] A. Cipitria, I.O. Golosnoy, T.W. Clyne, A sintering model for plasma-sprayed zirconia TBCs. Part I: free-standing coatings, Acta Mater. 57 (4) (2009) 980–992.
[380] V. Rat, J.F. Coudert, P. Fauchais, N. Caron, K. Wittman, S. Alexandre, Influence of plasma instabilities in ceramic suspension, Plasma Spraying 16 (December) (2007) 857–865.
[381] P. Fauchais, Suspension and solution plasma spraying, J. Phys. Appl. Phys. 46 (224015) (2013).
[382] G. Mauer, Numerical study on particle – gas interaction close to the substrates in thermal spray processes with high-kinetic and low-pressure conditions, J. Therm. Spray Technol. 28 (1) (2019) 27–39.
[383] G. Mauer, R. Vaßen, Conditions for nucleation and growth in the substrate boundary layer at plasma spray-physical vapor deposition (PS-PVD), Surf. Coating. Technol. 371 (2018), 417–27.
[384] K. Saha, S. Chaudhuri, B.M. Cetegen, Modeling of ceramic particle heating and melting in a microwave plasma, J. Heat Tran. 133 (3) (2011) 31002.
[385] P. Fauchais, G. Montavon, R.S. Lima, B.R. Marple, Engineering a new class of thermal spray nano-based microstructures from agglomerated nanostructured particles, suspensions and solutions: an invited review, J. Phys. Appl. Phys. 44 (9) (2011).
[386] B. Cai, Y. Yin, Y. Zheng, W. Wang, H. Gu, J. Yao, H. Wang, Mathematical study of spray flash evaporation in a spray-assisted seawater desalination chamber, Desalination 465 (March 2018) (2019) 25–37.
[387] D.J. Broer, W. Luijks, J. Appl. Polym. Sci. 26 (31R) (1981) 2415.
[388] H.O. Pierson, Handbook of Chemical Vapor Deposition: Principles, Technology and Applications, first ed., William Andrew Publishing, New York, 1999.
[389] B. Mitrovic, A. Gurary, W. Quinn, J. Cryst. Growth 303 (2007) 323.
[390] T.M. Rodgers, H. Zhao, H.N.G. Wadley, Vapor deposition on doublet airfoil substrates: coating thickness control, J. Vac. Sci. Technol.: Vacuum, Surfaces Films 33 (6) (2015) 61509.
[391] R.F. Bunshah, J. Vac. Sci. Technol. 11 (1974) 814.
[392] J. Webb, B. Casaday, B. Barker, J.P. Bons, A.D. Gledhill, N.P. Padture, J. Turbomach. 135 (2013): 021033.
[393] E.T. Swartz, Thermal boundary resistance, Rev. Mod. Phys. 61 (3) (1989).
[394] M. Baeva, D. Loffhagen, M.M. Becker, D. Uhrlandt, Fluid modelling of DC argon microplasmas: effects of the electron transport description, Plasma Chem. Plasma Process. 39 (4) (2019) 949–968.
[395] M.S. Benilov, Understanding and modelling plasma-electrode interaction in high-pressure arc discharges: a review, J. Phys. Appl. Phys. 41 (14) (2008).
[396] J.P. Trelles, J.P. Trelles, J.P. Trelles, J.P. Trelles, Non-equilibrium modelling of arc plasma, J. Phys. Appl. Phys. 40 (5937–5952) (2007).
[397] V. Rat, A.B. Murphy, J. Aubreton, P.F. Mf Elchinger, Treatment of non-equilibrium phenomena, J. Phys. Appl. Phys. 41 (2008) 183001.
[398] Ervin B. Podgoršak, Introduction to Modern Physics, 2014, p. 115.
[399] J. Menuey, C. Giolli, Solid particle erosion of thermal spray and physical vapour deposition thermal barrier coatings, Wear 271 (11–12) (2011) 2909–2918.
[400] R.G. Wellman, J.R. Nicholls, A review of the erosion of thermal barrier coatings, J. Phys. D Appl. Phys. 40 (2007) R293–R305.
[401] R.G. Wellman, J.R. Nicholls, Some observations on erosion mechanisms of EB-PVD TBCs, Wear 242 (2000) 89–96.
[402] R.G. Wellman, M.J. Deakin, J.R. Nicholls, The effect of TBC morphology on the erosion rate of EB-PVD TBCs, Wear 258 (2005) 349–356.
[403] X. Chen, M.Y. He, I. Spitsberg, N.A. Fleck, J.W. Hutchinson, A.G. Evans, Mechanisms governing the high temperature erosion of thermal barrier coatings, Wear 256 (2004) 735–746.